

Sustainable Civil Infrastructures

Meng-Chia Weng  
Shima Kawamura  
Jianwen Ding *Editors*

# Advancements in Geotechnical Engineering

Proceedings of the 6th GeoChina  
International Conference on Civil &  
Transportation Infrastructures: From  
Engineering to Smart & Green Life Cycle  
Solutions – Nanchang, China, 2021



 Springer

# **Sustainable Civil Infrastructures**

## **Editor-in-Chief**

Hany Farouk Shehata, SSIGE, Soil-Interaction Group in Egypt SSIGE, Cairo, Egypt

## **Advisory Editors**

Khalid M. ElZahaby, Housing and Building National Research Center, Giza, Egypt

Dar Hao Chen, Austin, TX, USA

**Sustainable Civil Infrastructures (SUCI)** is a series of peer-reviewed books and proceedings based on the best studies on emerging research from all fields related to sustainable infrastructures and aiming at improving our well-being and day-to-day lives. The infrastructures we are building today will shape our lives tomorrow. The complex and diverse nature of the impacts due to weather extremes on transportation and civil infrastructures can be seen in our roadways, bridges, and buildings. Extreme summer temperatures, droughts, flash floods, and rising numbers of freeze-thaw cycles pose challenges for civil infrastructure and can endanger public safety. We constantly hear how civil infrastructures need constant attention, preservation, and upgrading. Such improvements and developments would obviously benefit from our desired book series that provide sustainable engineering materials and designs. The economic impact is huge and much research has been conducted worldwide. The future holds many opportunities, not only for researchers in a given country, but also for the worldwide field engineers who apply and implement these technologies. We believe that no approach can succeed if it does not unite the efforts of various engineering disciplines from all over the world under one umbrella to offer a beacon of modern solutions to the global infrastructure. Experts from the various engineering disciplines around the globe will participate in this series, including: Geotechnical, Geological, Geoscience, Petroleum, Structural, Transportation, Bridge, Infrastructure, Energy, Architectural, Chemical and Materials, and other related Engineering disciplines.

**SUCI series is now indexed in SCOPUS  
and EI Compendex.**

More information about this series at <http://www.springer.com/series/15140>

Meng-Chia Weng · Shima Kawamura ·  
Jianwen Ding  
Editors

# Advancements in Geotechnical Engineering

Proceedings of the 6th GeoChina International  
Conference on Civil & Transportation  
Infrastructures: From Engineering  
to Smart & Green Life Cycle  
Solutions – Nanchang, China, 2021

 Springer

*Editors*

Meng-Chia Weng  
Department of Civil Engineering  
National Yang Ming Chiao Tung University  
Hsinchu, Taiwan

Shima Kawamura  
Muroran Institute of Technology  
Muroran, Japan

Jianwen Ding  
School of Transportation  
Southeast University  
Nanjing, China

ISSN 2366-3405

Sustainable Civil Infrastructures

ISBN 978-3-030-79797-3

<https://doi.org/10.1007/978-3-030-79798-0>

ISSN 2366-3413 (electronic)

ISBN 978-3-030-79798-0 (eBook)

© The Editor(s) (if applicable) and The Author(s), under exclusive license  
to Springer Nature Switzerland AG 2021

This work is subject to copyright. All rights are solely and exclusively licensed by the Publisher, whether the whole or part of the material is concerned, specifically the rights of translation, reprinting, reuse of illustrations, recitation, broadcasting, reproduction on microfilms or in any other physical way, and transmission or information storage and retrieval, electronic adaptation, computer software, or by similar or dissimilar methodology now known or hereafter developed.

The use of general descriptive names, registered names, trademarks, service marks, etc. in this publication does not imply, even in the absence of a specific statement, that such names are exempt from the relevant protective laws and regulations and therefore free for general use.

The publisher, the authors and the editors are safe to assume that the advice and information in this book are believed to be true and accurate at the date of publication. Neither the publisher nor the authors or the editors give a warranty, expressed or implied, with respect to the material contained herein or for any errors or omissions that may have been made. The publisher remains neutral with regard to jurisdictional claims in published maps and institutional affiliations.

This Springer imprint is published by the registered company Springer Nature Switzerland AG  
The registered company address is: Gewerbestrasse 11, 6330 Cham, Switzerland

# Introduction

This volume contains nine papers that were presented at the 6th GeoChina International Conference on Civil & Transportation Infrastructures: From Engineering to Smart and Green Life Cycle Solutions in Nanchang, China, during September 18–19, 2021. With increasing urbanization rates and the development of society, advancement in geotechnical technologies is essential to the construction of infrastructures. Geotechnical investigation is the first step of applying scientific methods and engineering principles to obtain solutions for civil engineering problems. This volume brings together scientific experts in different areas that contribute to the state of the art in geotechnical engineering such as testing of geomaterials, seismic response, grouting, slope and embankment stability, foundation, sustainability in geohazards, and some other geotechnical issues that are quite relevant in today's world.

# Contents

<b>Large-Scale 3D Random Finite Element Analysis of Embankment Seepage Stability</b> .....	1
Yong Liu, Man-Yu Wang, Yu-Tao Pan, and Kai Yao	
<b>River Levees Monitoring Using Three Dimensional Laser Point Clouds with SLAM Technology</b> .....	14
Nanoka Akiyama, Satoshi Nishiyama, Koki Sakita, Junsheng Song, and Fumiaki Yamazaki	
<b>Modeling of Pervious Pile-Supported Embankment Under the Consolidation Process</b> .....	23
Yanrou Guo, Jessica U. N. Jeong, Zan Zhou, and Thomas M. H. Lok	
<b>Seismic Response and Fragility Estimates of Highway Bridges Considering Various Modeling Uncertainty Parameters</b> .....	31
Huihui Li, Lifeng Li, and Liang Xu	
<b>Considerations of Vertical Acceleration Induced by Horizontal Earthquake Record for a Building with Underground Stories Based on a SSI 3D Model</b> .....	54
Mohammad Amin Mohammadyar and Ali Akhtarpour	
<b>Tip Post-grouting Using Smart Cells at Urubó Bridge - Premobilization and Improvement of End Resistance</b> .....	62
Antonio Marinucci, Mario Terceros Arce, and Mario A. Terceros Herrera	
<b>Analysis on the Influence of Rainfall Characteristics on the Stability of Granite Residual Soil Slope</b> .....	75
Cheng Chen, Jian-fei Liu, and Jun Gong	

**Development and Field Testing of Geocomposite Cellular Mats (GCM) to Minimize the Ground Movements of Highway Embankments Founded on Peat Ground** ..... 84  
Tuan Noor Hasanah Tuan Ismail, Devapriya Chitral Wijeyesekera, and Ismail Bakar

**Study on Response of Dual Layered Reinforced Stone Column Under Shear Loading** ..... 107  
Akash Jaiswal and Rakesh Kumar

**Author Index** ..... 119



## About the Editors

**Prof. Meng-Chia Weng** is a full professor in the Department of Civil Engineering at National Yang Ming Chiao Tung University, Taiwan. His main research interests are rock mechanics, landslides, constitutive modeling of geomaterials, discrete element method, and finite element method. He has authored 56 journal papers, 24 technical reports, and 90 conference papers. He is the associate editor of Journal of Materials of Civil Engineering, ASCE, the managing guest editor of Engineering Geology, and the editor of Journal of Geoengineering.

**Prof. Shima Kawamura** is a professor of Graduate School of Engineering, Muroran Institute of Technology, Japan. He received his Ph.D. in the Department of Civil Engineering from Hokkaido University, Japan, in 2000. His research interests include bearing capacity improvement of ground, stability evaluation of slopes in cold regions, dynamic behavior of ground during earthquake, and mechanical behavior of volcanic soils. He is currently a member of American Society of Civil Engineers (ASCE), Japan Society of Civil Engineers (JSCE), The Japanese Geotechnical Society (JGS), International Society of Soil Mechanics and Geotechnical Engineering (ISSMGE), and The International Geosynthetics Society (IGS). He is also active as editorial board for Soils and Foundations (JGS), and an associate editors for Japanese Geotechnical Journal (JGS).

**Prof. Jianwen Ding** is a professor of the Institute of Geotechnical Engineering, School of Transportation, Southeast University. He was a visiting scholar in school of civil engineering, Purdue University, from 04/2013 to 04/2014. His specialty is geotechnical engineering, and his research interests are as follows: mechanical behavior and settlement analysis of the big-diameter and super-long piles, comprehensive treatment of dredged clays (consolidation; solidification; recycling), subgrade engineering in highway (road embankment and road subbase), and underground engineering (tunnel; excavation engineering; subway). He is an active member of various academic societies. He has authored and co-authored 42 journal papers. He is in charge of three National Natural Science Foundation of China and many major engineering consulting projects.



# Large-Scale 3D Random Finite Element Analysis of Embankment Seepage Stability

Yong Liu<sup>1</sup>(✉), Man-Yu Wang<sup>1</sup>, Yu-Tao Pan<sup>2</sup>, and Kai Yao<sup>3</sup>

<sup>1</sup> State Key Laboratory of Water Resources and Hydropower Engineering Science, Institute of Engineering Risk and Disaster Prevention, Wuhan University, 299 Bayi Road, Wuhan 430072, People's Republic of China

liuy203@whu.edu.cn

<sup>2</sup> Department of Civil and Environmental Engineering, Norwegian University of Science and Technology, Høgskoleringen 7a, 7491 Trondheim, Norway

<sup>3</sup> School of Qilu Transportation, Shandong University,

12550 East Second Ring Road, Jinan 250002, People's Republic of China

**Abstract.** The stability assessment of a soil embankment in the flooding season has attracted increasing attention in recent years. The current study performs a coupled hydraulic-mechanical analysis of an embankment subjected to water level fluctuation. The coefficient of permeability of embankment soils is represented by a uniform random field with upper and lower bounds. The random finite element method is incorporated for the solution of such coupled analysis. The results indicate that the horizontal correlation length of the permeability field has significant effects on the seepage patterns, leading to a greater variability in the total flow rate, since water flows more easily along the regions of higher permeability. In addition, the failure mechanism resulted from the coupled analysis shows that a rise of water level plays a predominant role in the instability of the embankment, compared with the generated irregular seepage force. The factor of safety of the embankment decreases with the increase of upstream water level, and the corresponding failure mode also changes significantly. The findings from this study can serve as a guidance for the design or reinforcement of a soil embankment and provide a new insight into the solution of green life cycle and sustainable development of embankment engineering.

**Keywords:** Soil embankment · Heterogeneous permeability · Flow rate · Coupled hydraulic-mechanical analysis · Random finite element method

## 1 Introduction

A long soil embankment plays a vital role in preventing the water flow for flood protection purposes. However, the rise of water level caused by the continuing rainstorm may pose a great threat to the overall stability of an embankment composed of untreated natural soils (Jia et al. 2009; Gholami Korzani et al. 2018; Li et al. 2018). Once a failure of embankment occurs, the environment will be affected to a greater extent and the caused loss is unpredictable, such as the occurred events as shown in Fig. 1. In recent

years, increasing relevant events of collapse of a long embankment resulting from the seepage failure were widely reported (Rivera-Hernandez et al. 2019). For instance, such typical events of embankment breaching have taken place in the Poyang Lake regions of China in July 2020 (see Fig. 2), which caused irreparable losses to the agriculture and increased hidden dangers in terms of the stability of buildings. The process of such a failure is essentially a typical coupled hydraulic-mechanical problem defined in numerical investigation (Qi and Vanapalli 2015; Zhang et al. 2018). Many studies associated with this issue were carried out to tentatively seek an acceptable solution so that making it possible to clearly describe the coupled mechanism involved (Cho 2012; Rivera-Hernandez et al. 2019).

In general, the spatial distribution of porosity in natural soil mass is extremely uneven due mainly to the complexity of geo-structures, which may lead to a larger uncertainty in the hydraulic properties of soils compared with other mechanical parameters (Srivastava et al. 2010). In literature, it is found that the coefficient of permeability of most types of soils often covers two or more orders of magnitude (Swiss Standard SN 670 010b 1999), which means that it encounters a difficult in accounting for the spatial variability of soil permeability in a reliable way. Cho (2012) has examined the effects of uncertainty due to the spatial heterogeneity of soil permeability on the seepage flow through the dam and soil foundation, where the saturated hydraulic conductivity of soils was represented by a two-dimensional (2D) lognormal random field. However, the variation range of the random values generated from a marginal lognormal distribution is grossly limited; thus, it expects that a clear range of its values should be reflected (Fenton and Griffiths 2008). Moreover, the analysis of an embankment is essentially a three-dimensional (3D) numerical problem that cannot be neglected in the examination of failure mechanism; however, investigation related to this 3D issue is rarely covered in the previous studies (e.g. Griffiths and Fenton 1997). For such a large-scale analysis, the required efficiency also depends greatly on the representation method for the spatially variable soils. As such, these challenges form the motivation of the current study.

The intention of this work is to evaluate the performance of a large-scale 3D soil embankment subjected to water level fluctuation where the spatial heterogeneity of soil permeability is considered. The random finite element method is employed herein to obtain a relatively accurate solution of the output responses. Uncertainty of flow rate resulted from the spatially variable soil permeability is estimated by the probabilistic approach. The corresponding seepage pattern and failure mechanism under various combined conditions are also evaluated in detail.



**Fig. 1.** Failures of soil embankments from the field observation (a) Event 1 occurred in Xinjiang, China, February 2013 (Chen 2013) and (b) Event 2 occurred in Guangdong, China, May 2014 (Yu 2014).



**Fig. 2.** Typical events of embankment breaching due to continuous heavy rainfall taken place in the Poyang Lake regions of China in July 2020 (Chen 2020).

## 2 Governing Equations of Coupled Hydraulic-Mechanical Analysis

The coupled solutions related to the soil structure and water flow are required to simulate the process of seepage and deformation in a soil embankment (Zhang et al. 2018). The force equilibrium equations for a saturated soil in 3D condition can be expressed as:

$$\begin{cases} \frac{\partial \sigma_x}{\partial x} + \frac{\partial \tau_{xy}}{\partial y} + \frac{\partial \tau_{xz}}{\partial z} + b_x = 0 \\ \frac{\partial \tau_{yx}}{\partial x} + \frac{\partial \sigma_y}{\partial y} + \frac{\partial \tau_{yz}}{\partial z} + b_y = 0 \\ \frac{\partial \tau_{zx}}{\partial x} + \frac{\partial \tau_{zy}}{\partial y} + \frac{\partial \sigma_z}{\partial z} + b_z = 0 \end{cases} \quad (1)$$

where  $\sigma_x$ ,  $\sigma_y$ , and  $\sigma_z$  are the total normal stresses in the  $x$ -,  $y$ -, and  $z$ -directions, respectively;  $\tau_{xy}$  is the shear stress on the  $x$ -plane in the  $y$ -direction ( $\tau_{xy} = \tau_{yx}$ ), and  $\tau_{yz}$  and  $\tau_{zx}$  are similar to the former;  $b_x$ ,  $b_y$ , and  $b_z$  are the body forces in the  $x$ -,  $y$ -, and  $z$ -directions, respectively. For the saturated soils, the effective stress state variable is used in the coupled analysis:

$$\sigma' = \sigma - u_a + \chi(u_a - u_w) \quad (2)$$

where  $\sigma'$  is the effective stress;  $u_a$  is the pore air pressure, which is equal to zero in this study;  $u_w$  is the pore water pressure, and  $(u_a - u_w)$  is the matric suction;  $\chi$  is assumed to be equal to degree of saturation (i.e. equal to 1.0). Based on the effective stress, the modified Mohr-Coulomb failure criterion for the shear strength of saturated soils can be written as:

$$\tau_f = c' + (\sigma - u_w) \tan \phi' \quad (3)$$

where  $\tau_f$  is the shear strength;  $c'$  is the effective cohesion and  $\phi'$  is the effective friction angle. Based on the balance of pore water and the Darcy's law, the governing equation

for steady water flow through saturated soils based on mass conservation can be written as:

$$\frac{\partial^2 H}{\partial x^2} + \frac{\partial^2 H}{\partial y^2} + \frac{\partial^2 H}{\partial z^2} = 0 \tag{4}$$

where  $H$  is the hydraulic head. Combined with the given boundary conditions, the above equations reflecting the coupled mechanism are solved numerically by using finite element method within a prescribed number of iterations.

### 3 Methodology

#### 3.1 Modelling of Soil Embankment

This work extends the 2D embankment studied by Cho (2012) to a long idealized 3D model whose geometric profile and finite element mesh are shown in Fig. 3. The embankment with a height of 5 m and a length of 50 m is constructed on a 5 m thick soil foundation. Two stable upstream water levels of 7 m and 9 m are considered to reflect the fluctuation of water level during the rainstorm period. A fine mesh schedule with 250,460 eight-node brick pore pressure elements is discretized to meet the accuracy requirement of coupled analysis. The four sides of the model are on vertical rollers preventing movement in their vertical directions. the bottom of the mesh is fixed in all directions. Some distances away from the slope toe are placed to minimize the influence of displacement boundary on the failure mechanism. For the seepage boundary conditions, the upstream surfaces below the water level and the downstream flat surface are considered as permeable boundaries.

The soil property of the embankment is treated as the same as that of foundation layer due to the consideration of high similarity of soil materials in an adjacent site. The finite element model idealizes the soils as an elastic-perfectly plastic porous material with the Mohr-Coulomb failure criterion. The present research mainly focuses on the seepage behavior of a soil embankment where the permeability is modelled as spatially random; thus, for simplicity the effective shear strength parameters are assumed to be deterministic. The soil parameters used for the coupled analysis are listed in Table 1.

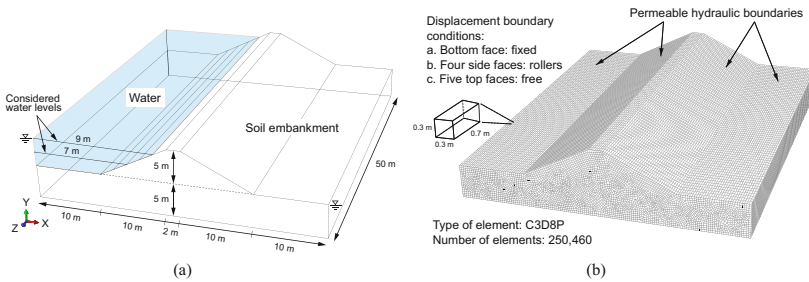


**Fig. 3.** (a) Profile of the embankment geometry; (b) displacement and seepage boundary conditions of the finite element model.

**Table 1.** Parameters of soil properties

Parameter	Unit	Symbol	Value
<b>(a) Deterministic parameters</b>			
Effective cohesion	kPa	$c'$	10
Effective friction angle	degree	$\varphi'$	15
Young's modulus	kPa	$E$	$10^4$
Poisson's ratio	—	$\nu$	0.3
Unit weight of water	kN/m <sup>3</sup>	$\gamma$	10.0
<b>(b) Statistical property of coefficient of permeability of soils</b>			
Coefficient of permeability	m/s	$k$	$5.0 \times 10^{-6} - 5.0 \times 10^{-4}$
Arithmetic average of $k$	m/s	—	$2.5 \times 10^{-4}$
Vertical correlation length of $k$	m	$\theta_v$	2
Horizontal correlation length of $k$	m	$\theta_h$	5, 10, 20

### 3.2 Spatial Variability of Soil Permeability

In this study, the spatial variability of the saturated coefficient of permeability of soils is represented by a 3D uniformly distributed random field, defined by its predefined upper and lower bounds and a correlation structure. The considered bounds for its value range from  $5.0 \times 10^{-6}$  to  $5.0 \times 10^{-4}$  m/s, and the corresponding correlation lengths are also listed in Table 1b. The random field with a marginal uniform distribution is generated through the translation approach (Grigoriu 1995), where the underlying Gaussian random field with a squared exponential auto-correlation structure is first generated by the modified linear estimation method (Liu et al. 2014). The reason for adopting a uniformly distributed random field in this study is that, for most types of soils its value of coefficient of permeability often covers several orders of magnitude (Swiss Standard SN 670 010b 1999), and the likelihood of each value involved in this range is considered to be equal in order to reduce the influence caused by its excessive variability. This is a major advantage relative to the use of a lognormal distribution in modelling the spatial heterogeneity of soil permeability, although the lognormal one has been widely used in previous similar studies (e.g. Cho 2012).

In geotechnical engineering, the vertical correlation length of soil properties often varies in a small domain relative to model geometry and may easily be estimated from in situ measured data, whereas the horizontal correlation length is generally much larger than the vertical one and more challenging to be quantified in a reliable way (Phoon and Kulhawey 1999). For this reason, the vertical correlation length of the permeability field remains constant, while the horizontal one varies in the parametric studies.

### 3.3 Description of Coupled Process

The numerical coupled process involved in this study consists of two main analysis steps. With the given seepage boundaries, a steady-state seepage analysis incorporated with the generated random field is first performed to gain the contours of pore water pressure and to calculate the total flow rate through the embankment. After determining the pore pressure at each integration point, the stress distribution can then be computed according to the principle of effective stress. At this stage, a static analysis step is set to evaluate the stability of the embankment within the predefined iteration numbers. The strength reduction technique widely used for the problems of slope stability is employed to obtain the minimum factor of safety of the embankment. Details of this technique can refer to the work by Wang et al. (2020). The non-convergence of the finite element program is herein taken as a basis for determining the occurrence of instability of an embankment.

### 3.4 Monte Carlo Simulation

A reliable estimation of the flow rate is necessary for the seepage behavior of a soil embankment when taking the spatial variability of permeability into account. The Monte Carlo simulation is performed due to its better robustness compared with other probabilistic methods (Fenton and Griffiths 2008). In a Monte Carlo simulation, the random permeability field varies from one realization to the next, and this process should be repeated to obtain the statistical properties of the flow rate. The convergence result of the statistics of normalized flow rate shown in Fig. 4, based on the embankment models with a 7 m water level but under various correlation lengths, indicates that 100 times of simulation is sufficient to obtain an acceptable consequence. On the other hand, for the large-scale 3D finite element model analyzed in this study, the Monte Carlo technique requires a large amount of computational efforts, but it can be completed through the parallel computing on a high-performance workstation.

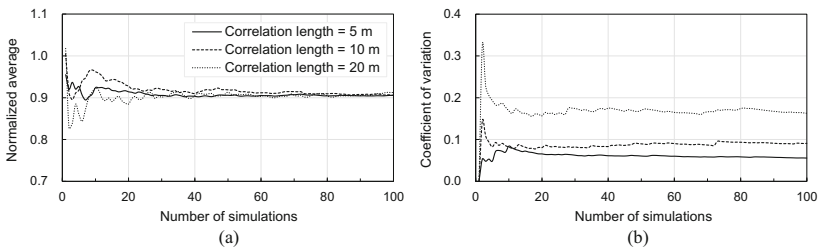


**Fig. 4.** Convergence check of Monte Carlo simulations by plotting the statistics of normalized flow rate (a) average and (b) coefficient of variation as a function of the number of simulations based on the cases with a 7 m upstream water level but under various correlation lengths.

## 4 Results and Discussion

### 4.1 Deterministic Analysis

Prior to probabilistic investigations, a deterministic coupled analysis is performed with a fixed coefficient of permeability of  $2.5 \times 10^{-4}$  m/s at the arithmetic average of the uniform distribution. Although the results of a 3D deterministic analysis may be basically identical to that from a 2D case, it can assess the ability of the numerical analysis to predict the coupled behaviors associated with the failure mechanism of a soil embankment.

Figure 5 shows the vectors of seepage velocity in the deterministic embankment soils under two sets of upstream water levels. For simplicity only half of the entire model is herein presented (i.e. 25 m in the axis direction). It can be seen that the water flow within embankment follows a common seepage pattern encountered in general cases. From the observations at the downstream exit, for each vertical cross section the seepage patterns are the same as each other, verifying the viewpoint that a 2D coupled analysis is considered reasonable and accurate enough if only the deterministic soil is analyzed. The computed total flow rate passing through the 3D embankment obtained with the finite element method, for upstream water levels with 7 m and 9 m, respectively, are  $28.5 \text{ m}^3/\text{h}$  and  $68.2 \text{ m}^3/\text{h}$ . Moreover, since the entire embankment soil is assumed to be at a saturated state under rainstorm conditions, a part of water flow above the phreatic line can be observed apparently. By comparing the two cases presented in Fig. 5, the rise of water level varying from 7 m to 9 m significantly raises the position of the outflow, forming a free outflow surface at the downstream slope of the embankment as shown in Fig. 5b. These observations resulting from the 3D deterministic analyses give a reasonable approximation to the coupled performance of a large-scale embankment, which offers a solid basis for the random finite element analysis.

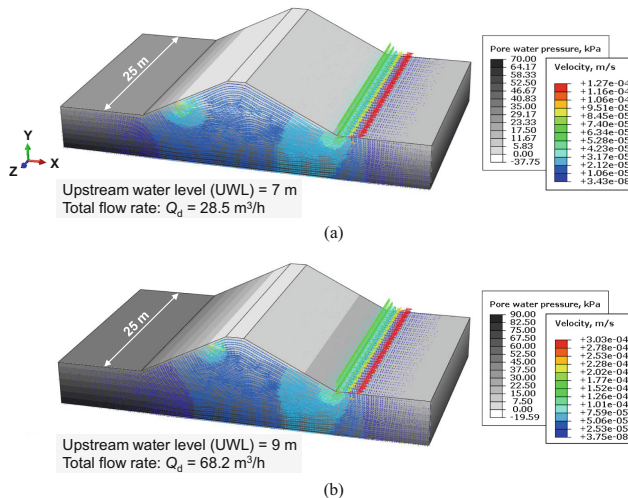


**Fig. 5.** Distribution of pore water pressure and vectors of seepage velocity in deterministic soils for the embankment with an upstream water level of (a) 7 m and (b) 9 m.



## 4.2 Estimation of Total Flow Rate Through Embankment

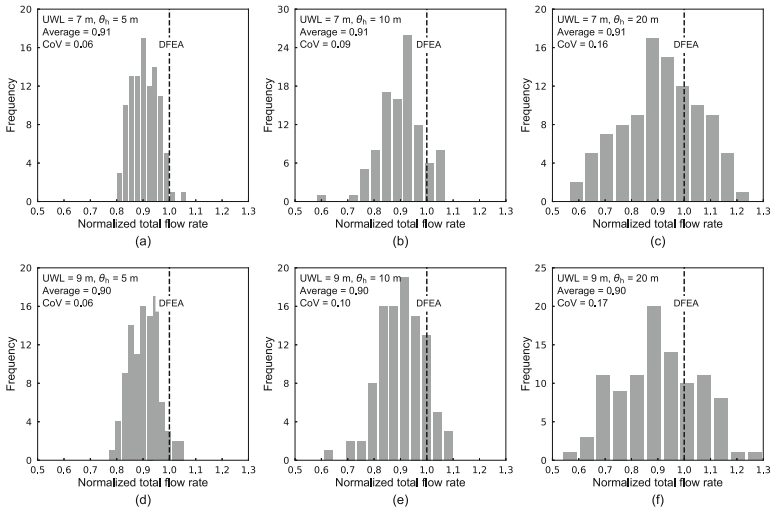
In this section, a parametric study on the horizontal correlation length of the 3D uniformly distributed random field is carried out to estimate the quantity of the flow rate through the embankment. Each realization of random field for the cases with the same correlation length but different water levels are identical to guarantee the consistency of the site.

Figure 6 shows the effects of horizontal correlation length  $\theta_h$  on the histograms of normalized total flow rate for embankments under different water levels. Without loss of generality, for simplicity all the results of flow rate obtained from random models are normalized by the corresponding deterministic result marked as the vertical dotted line in those graphs. Only the results of these cases with a water level of 7 m are illustrated due to its similarity in histogram distributions with that of 9 m water level. For a small correlation length  $\theta_h$  of 5 m relative to the embankment geometry, as shown in Fig. 6a, the deterministic result can give a relatively conservative estimation of the possible quantity of flow rate. The computed random results are distributed within a small range being represented by a low coefficient of variation. This is probably because that when the water flow passes through the soils with random permeability, it is more likely to flow along the zones of higher permeability. On the basis of this fact, since a relatively small correlation length is considered, it may lead to a limited variation of the permeability field for each realization as a whole. It can be seen from Fig. 6b that the increase of the correlation length leads to an increase in the coefficient of variation of these random results. Although the position of soils with low or high permeability is different in each simulation, the water is generally more concentrated due to the better continuity of soils of higher permeability, which can affect the quantity of the total flow rate through the embankment. This effect becomes more apparent when the correlation length is 20 m as illustrated in Fig. 6c, and it leads to a greater coefficient of variation of flow rate than that of the above two cases. Under such a scenario, the difference in the resulted flow rate depends largely on each realization of the permeability field; therefore, the larger the areas of higher permeability in one realization, the greater the computed flow rate.

For all the cases applied with a water level of 9 m but under various correlation lengths, the histogram distributions of the resulted normalized flow rate shown in Figs. 6d–f are highly similar to that from the corresponding cases with a 7 m water level (see Figs. 6a–c). Such a high similarity in terms of these dimensionless results may be attributed to a fact that the same sample of the permeability field is utilized in a sequence of realizations of Monte Carlo simulations. By use of the consistency of the basic tend presented in Fig. 6, the dimensionless results of flow rate can be used reasonably for probabilistically evaluating the seepage performance of embankments with other water levels that are not considered in this study, with a combination of the corresponding deterministic coupled result.

## 4.3 Seepage Pattern

Figure 7 shows the profiles of seepage patterns occurred in random soils with different correlation lengths for the embankments applied with a water level of 7 m, which are illustrated based on a typical realization of random field for each scenario presented. For a better understanding, three vertical cross-sections (i.e. sections of A-A, B-B and C-C



**Fig. 6.** Histograms of normalized total flow rate for embankments with different combinations of upstream water level (UWL) and horizontal correlation length ( $\theta_h$ ). CoV = coefficient of variation; DFEA = deterministic finite element analysis. The value of coefficient of permeability used in the DFEA is the arithmetic average of the uniform distribution, as listed in Table 1b.

as depicted in Fig. 7a) across the embankment model at different locations are selected to provide more details of the internal variation of water flow.

For a small value  $\theta_h$  of 5 m as shown in Fig. 7a, the flow path of the water is significantly affected by the non-uniform soils with random permeability. As expected, the water flows more easily along those regions of higher permeability, which leads to a grossly irregular seepage pattern differing from the deterministic case shown in Fig. 5a. For the soils with lower permeability near the upstream surface, it has certain positive effects on preventing the water from entering into the embankment. This effect may be more apparent and controlled when it uses a 2D model that is essentially a cross-section of a 3D embankment. According to the overall velocity vectors distribution at the exit, the permeability field also greatly affects the maximum exit gradient reflecting the local seepage behavior, but of which the estimation of the maximum exit gradient is beyond the scope of this study. When a slightly larger correlation length  $\theta_h$  of 10 m is considered, as shown in Fig. 7b, a more horizontally continuous flow pattern can be observed throughout each vertical cross-section of the embankment. Such a situation provides a more direct channel for the water flow, although the areas of lower permeability are also relatively larger. Another scenario is also possible that the regions of low permeability is greater than that of high permeability, which can reduce the quantity of total flow rate passing through the embankment. For the case considering a  $\theta_h$  of 20 m shown in Fig. 7c, the locations of concentrated water flow change more significantly due to the greater blocked effect of soil regions with lower permeability. The variation of flow rate depends largely on the realization of permeability field in which it is likely to obtain a smaller or larger flow rate, which can be inferred from the results shown in Fig. 6c.

For the cases with a 9 m water level, the corresponding seepage patterns at each cross-section of the embankment are presented in Fig. 8, where its realizations of permeability field under various correlation lengths remain the same as shown in Fig. 7. Comparison of these contours between Figs. 7 and 8 shows that the rise of water level mainly affects the flow pattern on the upper part of the embankment and increases the magnitude of velocity vectors at the exit positions, which is consistent with most of the observations and measured data from an engineering site. Under such a situation of raising water level, the resulted flow rate will also increase obviously as presented in Figs. 5 and 6. These results of seepage patterns in various scenarios explained above can serve as a valuable basis for reducing the risk of seepage failure of a soil embankment subjected to fluctuation in water level.

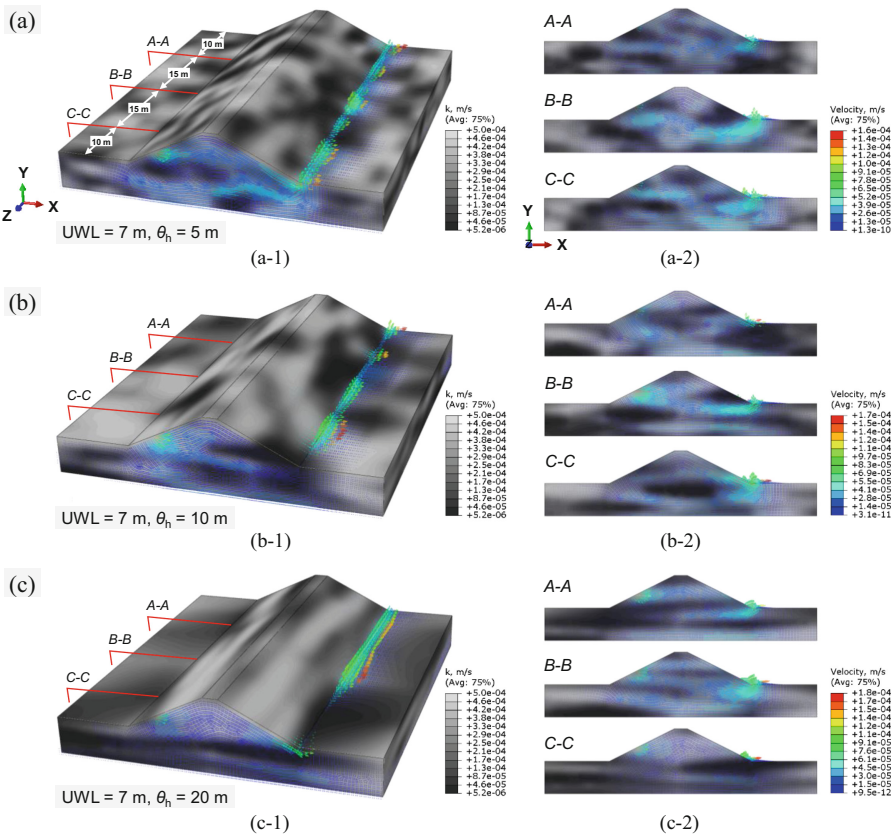


**Fig. 7.** Velocity vectors of seepage in random soils with a horizontal correlation length of (a) 5 m, (b) 10 m, and (c) 20 m for the embankment applied with a 7 m water level. UWL = upstream water level;  $\theta_h$  = horizontal correlation length.

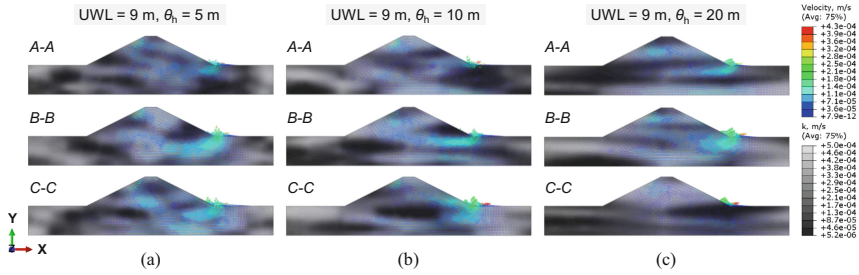


**Fig. 8.** Velocity vectors of seepage in random soils with a horizontal correlation length of (a) 5 m, (b) 10 m, and (c) 20 m at each cross-section of the same realization shown in Fig. 7 for the embankment applied with a 9 m water level.

#### 4.4 Failure Mechanism

Figure 9 shows the contours of maximum principal plastic strain for the embankments subjected to different water levels, of which the case with a 5 m water level presented in Fig. 9a is considered as a comparison example. Note that the failure modes of all the random models under various water levels are basically identical with the corresponding deterministic cases. The main reason for this phenomenon may be attributed to the failure mechanism that, the rise of a certain water level results in the increase of pore water pressure applied on the soil skeletons near the toe of the upstream slope, and the shear strength of the soils is then reduced in accordance with the principle of effective stress. This statement can be exemplified indirectly by the result of the case with the same water level at the upstream and downstream sides of the embankment (see Fig. 9a), in which two basically symmetrical failure modes can be observed and the overall stability of this embankment represented by a factor of safety of 1.62 is much better than the other scenarios. In accordance with the non-convergence of finite element program, with the increase of water level, the shear strength of the soils in those regions of higher pore water pressure will be faster to reach a threshold value in the process of strength reduction operation. For this reason, the shear failure zones of an embankment with higher water level will be reduced in different degree and a corresponding smaller factor of safety can be obtained associated with the failure state (see Figs. 9b and c).

Another issue related to the coupled performance is the effect of internal uneven seepage forces caused by the random soil permeability on the stability of the embankment. Based on the results of irregular seepage patterns described earlier, a greater seepage force may be likely generated in the soil regions of higher permeability due to the faster speed of water flow, which may result in some local seepage failures in reality, such as piping. Although this fact is relatively important from a practical viewpoint, in the numerical coupled analysis the overall stability of an embankment depends mainly on the shear strength of soils. Therefore, a rise of water level plays a more dominant role in inducing the stability failure of an embankment than the irregular seepage force acted on the soils.

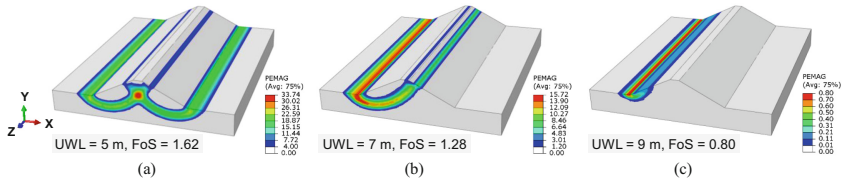


**Fig. 9.** Failure modes and the corresponding factors of safety for the embankments under various water levels of (a) 5 m, (b) 7 m, and (c) 9 m. UWL = upstream water level; FoS = factor of safety.

## 5 Concluding Remarks

The coupled solutions of a large-scale 3D soil embankment subjected to water level fluctuation are evaluated by using the random finite element method in this study. The soil permeability controlling the seepage behavior is considered as spatially variable, being represented by a random field with a uniform distribution. The histogram results of normalized total flow rate indicate that the horizontal correlation length of the permeability field has significant effects on the seepage response; that is, the variability of the obtained flow rate increases with the increase of correlation length. This is mainly due to the effect of irregular seepage patterns caused by the heterogeneous soil permeability. The profiles of seepage velocity vectors in random soils demonstrate that the water is more likely to flow along the regions of higher permeability and a relatively concentrated flow field then is formed, especially when a greater correlation length is considered in the analysis. The contour results also show that in the same site the variation of water level mainly affects the seepage pattern near the upstream part of an embankment. In addition, the failure mechanism indicates that a rise of water level plays a dominant role in leading to the instability of the embankment compared with the generated irregular seepage force, due mainly to the great reduction of the effective stress of soil skeletons near the upstream slope toe. The factor of safety of the embankment decreases with the increase of upstream water level, and the corresponding failure mode changes significantly. The investigated results from this study contribute to the design or reinforcement of a soil embankment and serve as a basis of the green cycle and sustainable development of embankment engineering.

This study mainly highlights the effect of spatial heterogeneity in soil permeability, whereas the shear strength parameters of soils are treated as constant. However, the soil strength should also be spatially varying in different degree, which may affect the global stability of an embankment (e.g. Ji and Chan 2014; Liu et al. 2018). Moreover, transient-state analysis considering the dynamic hydraulic head is desirable as it may replicate the factual failure mechanism in high flow speed conditions. These issues form strands of future works.

**Acknowledgements.** This research is supported by the National Natural Science Foundation of China (Grant No.: 52079099; 51879203).

## References

- Chen, J.: Breaching of Lianfeng reservoir in Xinjiang due to leakage. *Chinanews* (2013). <http://www.chinanews.com/tp/hd2011/2013/02-02/171499.shtml>
- Chen, W.T.: Crevasse rescue of embankment in the east and west sides of Poyang Lake. *Bjnews* (2020). <https://www.bjnews.com.cn/detail/159464002415876.html>
- Cho, S.E.: Probabilistic analysis of seepage that considers the spatial variability of permeability for an embankment on soil foundation. *Eng. Geol.* **133–134**, 30–39 (2012)
- Fenton, G.A., Griffiths, D.V.: *Risk Assessment in Geotechnical Engineering*. Wiley, Hoboken (2008)
- Grigoriu, M.: *Applied Non-Gaussian Processes: Examples, Theory, Simulation, Linear Random Vibration, and MATLAB Solutions*. Prentice-Hall International (UK) Limited, London (1995)
- Griffiths, D.V., Fenton, G.A.: Three-dimensional seepage through spatially random soil. *J. Geotech. Geoenviron. Eng.* **123**(2), 153–160 (1997)
- Gholami Korzani, M., Galindo-Torres, S.A., Scheuermann, A., Williams, D.J.: Smoothed Particle hydrodynamics for investigating hydraulic and mechanical behaviour of an embankment under action of flooding and overburden loads. *Comput. Geotech.* **94**, 31–45 (2018)
- Ji, J., Chan, C.L.: Long embankment failure accounting for longitudinal spatial variation – a probabilistic study. *Comput. Geotech.* **61**, 50–56 (2014)
- Jia, G.W., Zhan, T.L.T., Chen, Y.M., Fredlund, D.G.: Performance of a large-scale slope model subjected to rising and lowering water levels. *Eng. Geol.* **106**(1–2), 92–103 (2009)
- Liu, Y., Lee, F.H., Quek, S.T., Beer, M.: Modified linear estimation method for generating multi-dimensional multi-variate Gaussian field in modelling material properties. *Probab. Eng. Mech.* **38**, 42–53 (2014)
- Liu, Y., Zhang, W., Zhang, L., Zhu, Z., Hu, J., Wei, H.: Probabilistic stability analyses of undrained slopes by 3D random fields and finite element methods. *Geosci. Front.* **9**(6), 1657–1664 (2018)
- Li, Z., Ye, W., Marence, M., Bricker, J.: Unsteady seepage behavior of an earthfill dam during drought-flood cycles. *Geosciences* **9**(1), 17 (2018)
- Phoon, K.K., Kulhawy, F.H.: Evaluation of geotechnical property variability. *Can. Geotech. J.* **36**(4), 625–639 (1999)
- Qi, S., Vanapalli, S.K.: Hydro-mechanical coupling effect on surficial layer stability of unsaturated expansive soil slopes. *Comput. Geotech.* **70**, 68–82 (2015)
- Rivera-Hernandez, X.A., Ellithy, G.S., Vahedifard, F.: Integrating field monitoring and numerical modeling to evaluate performance of a Levee under climatic and tidal variations. *J. Geotech. Geoenviron. Eng.* **145**(10), 05019009 (2019)
- Swiss Standard SN 670 010b: Characteristic coefficients of soils. Association of Swiss Road and Traffic Engineers, Zurich (1999)
- Srivastava, A., Babu, G.L.S., Haldar, S.: Influence of spatial variability of permeability property on steady state seepage flow and slope stability analysis. *Eng. Geol.* **110**(3–4), 93–101 (2010)
- Wang, M.Y., Liu, Y., Ding, Y.N., Yi, B.L.: Probabilistic stability analyses of multi-stage soil slopes by bivariate random fields and finite element methods. *Comput. Geotech.* **122**, 103529 (2020)
- Yu, X.: Bursting of embankment in Leizhou Youth Canal in Guangdong Province. *Chinadaily* (2014). [http://cnews.chinadaily.com.cn/2014-05/21/content\\_17528086.htm](http://cnews.chinadaily.com.cn/2014-05/21/content_17528086.htm)
- Zhang, L., Wu, F., Zheng, Y., Chen, L., Zhang, J., Li, X.: Probabilistic calibration of a coupled hydro-mechanical slope stability model with integration of multiple observations. *Georisk Assess. Manage. Risk Eng. Syst. Geohazards* **12**(3), 169–182 (2018)



# River Levees Monitoring Using Three Dimensional Laser Point Clouds with SLAM Technology

Nanoka Akiyama<sup>1</sup>(✉), Satoshi Nishiyama<sup>2</sup>, Koki Sakita<sup>2</sup>, Junsheng Song<sup>3</sup>, and Fumiaki Yamazaki<sup>4</sup>

<sup>1</sup> Faculty of Environmental Science and Technology, Okayama University,  
3 Chome-1 Tsushimanaka, Kita Ward, Okayama, Japan  
p02j21g1@s.okayama-u.ac.jp

<sup>2</sup> Graduate School of Natural Science and Technology, Okayama University,  
3 Chome-1 Tsushimanaka, Kita Ward, Okayama, Japan

<sup>3</sup> China University of Mining and Technology, Wu Dao Kou, Haidian District, Beijing, China

<sup>4</sup> KASIK-VISION, 2 Chome-4 Suminoe, Otaru, Hokkaido, Japan

**Abstract.** In recent years, record rainfalls have frequently occurred due to global warming, and river patrols and inspections are becoming increasingly important to prevent large-scale disasters such as levee breaks. The purpose of this paper is to introduce an IoT-based surveying method termed Simultaneous Localization and Mapping (SLAM) for river patrols and inspections. SLAM estimates the position of the technology itself and creates an entire map at the same time. Specifically, by performing the river patrols and inspections using SLAM technology with backpack-type LiDAR sensors, we could obtain the three-dimensional coordinate data of the levee at low cost. We have developed a monitoring method to quantitatively identify the locations of river levee deformations. We can obtain a high density of 56.5 million points with the LiDAR and present the accuracy of three-dimensional levee reproducibility using SLAM technology. In this paper, we demonstrate the usefulness of the LiDAR with SLAM technology based on monitoring data.

**Keywords:** River inspections · Three-dimensional laser point group · SLAM · Drone

## 1 Introduction

In recent years, record rainfalls have frequently occurred due to global warming, and river inspection to understand local situations has become more important for preventing large-scale disasters, such as levee breaches. In Japan, in 2017 and 2018, river levees managed by central and prefectural governments broke, causing severe damage. In these disasters, it became clear that even a single breach in a river levee, which is a linear structure, can cause serious damage. Considering that the frequency of rainfalls exceeding 50 mm per hour is increasing, it is even more important to carefully check the soundness of

the levees over significant distances. However, the paucity of engineers and financial resources on the national and local government levels has become serious, and it is difficult to perform detailed levee inspection. Furthermore, the current levee inspection data are qualitative from visual inspection, and soundness is judged based on engineer experience. Overall, sufficient measures have not been taken to prioritize the necessary points.

Therefore, efficiently acquiring 3D data for levees by drone survey has attracted attention in recent years. This method makes it possible to quantitatively identify the changes that have only been understood qualitatively thus far. There are two methods of acquiring 3D data by drone survey: using digital images or using a laser scanner. The latter method has been expected to be effective for river levees because it requires less labor to install control points in the target area to be surveyed compared to the former method, which uses digital images. However, the self-positioning accuracy during drone surveys depends on the reception environment of GNSS, and sometimes, high-precision surveying cannot be expected depending on the time and place. Another issue is that if a drone is equipped with a heavy measurement device such as a laser, the flight time is limited to several tens of minutes due to the battery life, making it difficult to monitor a large area efficiently.

On the other hand, laser surveying methods implementing simultaneous localization and mapping (SLAM) technology, which has been practically applied in vehicle autonomous driving technology in recent years, are currently receiving attention. SLAM is a generic term for technologies that perform self-location estimation and whole map creation simultaneously. For an autonomous vehicle to recognize a place for the first time, it must create a map based on the information obtained while moving and estimate its own position on the map, and SLAM is used for this application. Because the system configuration is simple, 3D laser surveying while walking can be realized by combining it with a portable laser scanner. By combining this technology with the current patrol and inspection work, it is expected that 3D coordinate data for levees can be easily acquired and the technology for grasping the deformed portion of the river levee in real time can be realized. However, the deformation grasping technology of river embankment by combination of this SLAM and laser survey has not yet been generalized.

Against this background, this paper summarizes the advantages and disadvantages of 3D laser point cloud acquisition technology given by the portable laser measurement system incorporating drone survey and SLAM and presents the possibility of future 3D river levee monitoring. Specially, a system equipped with a green laser scanner of wavelength 532 nm was used for drone surveys. Because green lasers have the ability to penetrate water, it is expected to be applied to the regular cross-section measurement of rivers. In addition, the method is also expected to be able to acquire continuous 3D data from above the ground surface to below the water surface, as it will be possible to perform surveys with the same degree of accuracy as compared to conventional surveys using near-infrared lasers. This study applies both technologies, which are expected to be put



to practical use in the future, to concrete sites, and summarizes the problems concerning survey accuracy and convenience based on actual examples. Furthermore, in this paper, the detection of river structure deformation such as foot protection is also targeted as a method of using 3D data. These results are expected to contribute to the provision of useful data when applying the monitoring method by 3D data to river management in the future.

## 2 Outline of the 3D Laser Point Cloud Acquisition System for the River Levee

### 2.1 Overview of Drone Equipped with Green Laser

Figure 1 shows a drone equipped with a green laser scanner, Fig. 2 shows the green laser scanner, and Table 1 presents the scanner specifications. The scanner weighs 2.8 kg, and the drone can fly for approximately 30 min. The scanner has a scanning range of 300 m and a scan rate of 60,000 points/s. The drone is equipped with a GNSS system with  $\pm 10$  mm horizontal and  $\pm 20$  mm altitude positioning accuracy.



**Fig. 1.** Drone-mounted LiDAR system



**Fig. 2.** Scanner

**Table 1.** Specifications of drone-mounted LiDAR

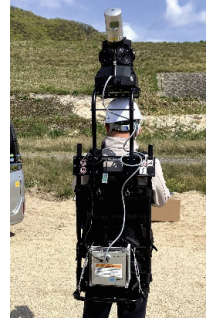
Laser wavelength	$532 \pm 1$ nm
Laser pulse rate	60,000 Hz
Scan speed	30 scan/s
Beam divergence	0.3 mrad
Weight	2.8 kg

## 2.2 Outline of Portable Laser Measurement System

Figure 3 shows the portable laser measurement system tried in this research, and Table 2 details the system characteristics, including the specifications of the laser scanner. Here, we attempted measurements using two measurement systems with different self-position survey methods. One used SLAM, and the other used GNSS and an Inertial Measurement Unit (IMU). We call these survey method A and B, respectively. The lasers used were all in the near infrared wavelength range.



(a) Survey method A



(b) Survey method B

**Fig. 3.** Overview of the portable laser scanner

**Table 2.** Specifications of the portable laser measurement system

	Survey method A	Survey method B
Maximum scope of laser measurements	80–100 m	100 m
Laser scan rate	300,000 Hz	700,000 Hz
Self-positioning method	SLAM	IMU + GNSS

## 3 Measurement Results

### 3.1 Overview of Measurement Site and Work

Figure 4 shows the site situation where the 3D laser point cloud was acquired. The measurements were taken in the 1.2 km portion denoted by the red line in the figure. The drone conducted measurements at an altitude of 50 m above ground, with a side lap of 75% and a flight speed at 2.5 m/s. Using the portable drone measurement system, the measurement was completed in about 90 min on foot for the range shown in Fig. 4. On the other hand, the drone flew 5 courses over approximately 120 min. Although the difference in the time spent for measurement was not significant, the former had the advantage of easy on-site assembly, convenience that could be taken by walking, and has the advantage of not requiring specialized flight skill training like the latter.

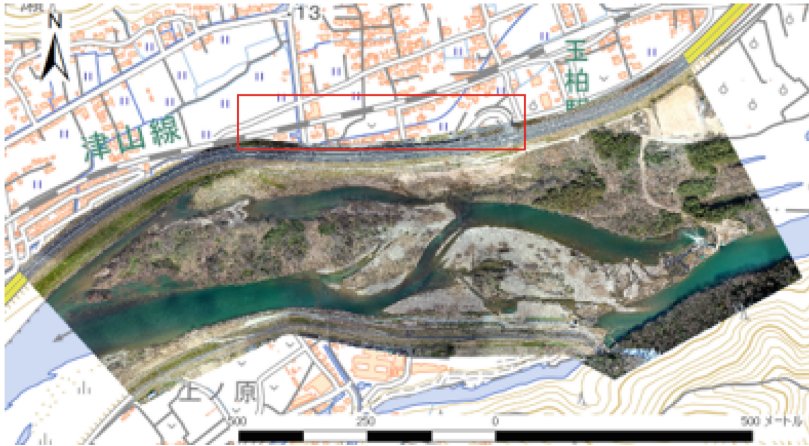
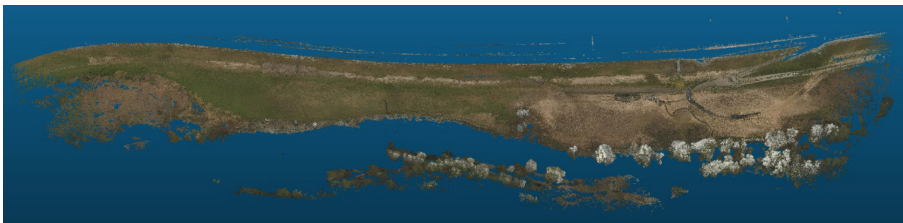


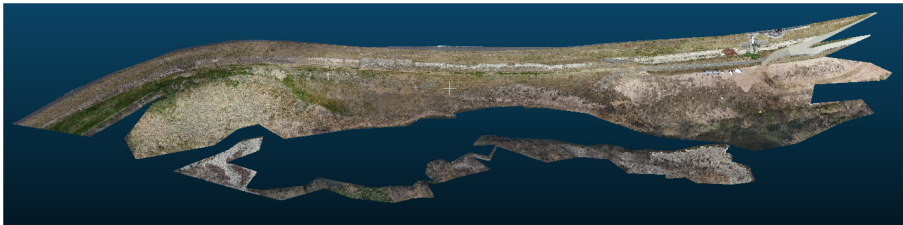
Fig. 4. Measurement site

### 3.2 Results of 3D Model Creation from Measurement Data

Figure 5 shows the river levee reproduction results obtained by survey method A. The laser point cloud obtained by the drone was trimmed according to the shape of the laser cloud obtained by the portable laser measurement system. The point density in the figure consists of 25.3 million points for the drone and 56.5 million points for the portable laser measurement system. In both cases, the levee can be reproduced with a high density of points. Figure 6 shows a slope that was reproduced using the portable laser measurement system on foot. Because obtaining measurements by walking on the inside of the levee is easy, it is possible to understand the sluice gate shape in detail, unlike the measurement from a drone at an altitude of 50 m above ground.



(a)Results of the portable laser measurement system



(b)Results of the drone survey

Fig. 5. Results of reproduction by laser point cloud



**Fig. 6.** Laser point cloud obtained by on-foot measurements on the inside of the levee using the portable laser measurement system

### 3.3 Accuracy Verification Results

Table 3 is a comparison of the survey results using the total station (TS) with the drone survey results, using the verification points installed within the measurement range. There are five verification points, and RMSE is the root mean square error of these. Both the X and Y planes and the elevation indicated by Z in the table are within  $\pm 50$  mm of the average or RMSE with respect to the TS result.

**Table 3.** Drone survey accuracy verification results

(units: mm)	X	Y	Z
Average difference	0.0	13.0	-8.0
RMSE	40.0	15.0	27.0

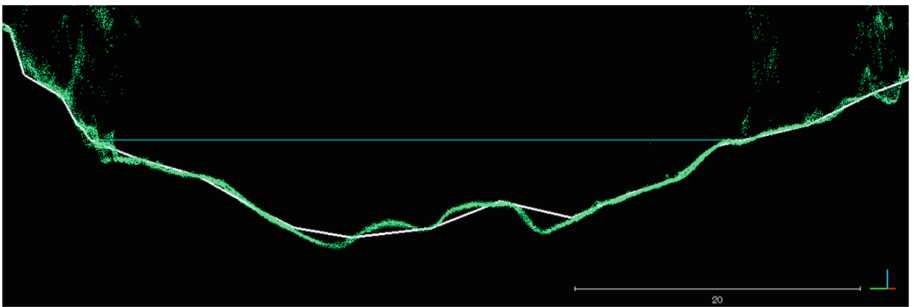
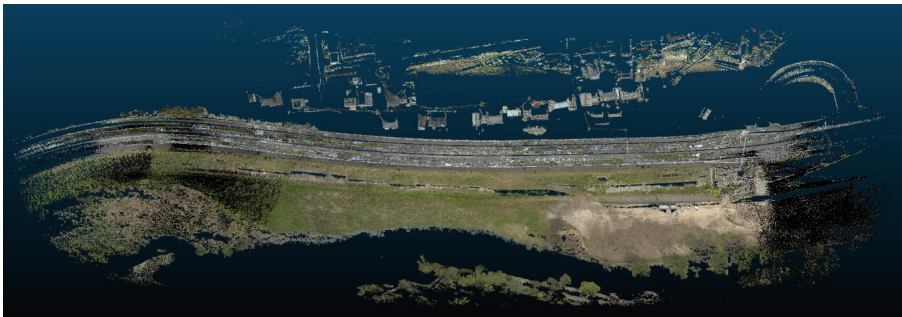


**Fig. 7.** Riverbed measurement results by drone survey (Blue solid line represents the water surface).

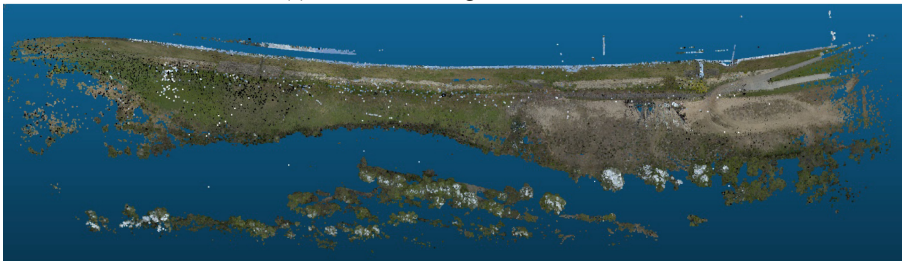
Figure 7 shows the results of measuring the riverbed by leveraging the characteristics of the green laser. The green point clouds in the figure is the measurement data by the laser, and the white solid line is the measurement result by bathymetric survey. By the

way, the water depth of the cross-section survey diagram was 1.9 m. The water depth that can be measured depends on the transparency, but it was shown that at this site, the shape can be measured with almost the same accuracy as the white solid line up to a water depth of approximately 2.0 m.

In the measurement using the portable laser measurement system, the linearly structured levee was divided into several sections, and the measured data were overlaid without installing landmarks. For survey method A, the accuracy of integrating the 3D data obtained by continuously walking the entire 800 m section (Fig. 4) and the data obtained by in 150 to 200 m section increments was verified. Moreover, for survey method B, the accuracy of the measurement data obtained by walking the levee crown and the measurement data obtained by walking the flood-channel were both verified. Figure 8 shows the measurement results of survey method B, and Table 4 shows the accuracy results of each measurement data compared with the drone survey accuracy verification results.



(a) Result of walking the levee crown



(b) Result of walking the flood-channel

**Fig. 8.** Reproduction results from survey method B

For the two data collection methods used for survey method A, a difference in accuracy of about 0.2 m was observed. This is thought to be due to an issue with the SLAM technology whereby it accumulates errors. Moreover, for survey method B, a difference in accuracy of about 0.2 m was observed in places with no noise, such as sidewalks, and places with a significant noise due to vegetation, such as the flood channel. But it was found that even with the self-positioning measurement using only SLAM, the same degree of accuracy was obtained as that using GNSS and IMU. Hence, 3D data can be acquired with a lower-cost hardware configuration by dividing the measurement area into sections and conducting measurements in consideration of SLAM features.

**Table 4.** Accuracy verification results for survey methods A and B of the portable laser measurement system

(units: m)	Survey method A		Survey method B	
	Walk sections	Continuous walking	Levee crown	Flood channel
RMSE	0.31	0.49	0.33	0.50

## 4 Conclusion

In this study, we attempted to measure a river levee using a portable laser scanner and a drone. As methods for 3D reproducing the shape of it. The former method does not depend on the accuracy of GNSS positioning by introducing SLAM technology, and the latter uses a green laser that can be applied to riverbed measurements. Both methods are expected to be applied for river inspections in the future. The usage of each method derived from the results of this research is presented as follows.

- (1) The drone survey equipped with the green laser has the advantage that not only can the riverbed be measured, but also the levee shape can be reproduced with high accuracy. In river management, the accuracy required when measuring the levee height and shape is  $\pm 50$  mm, and this method met these requirements. Furthermore, the range that can be measured with one flight is several km, but changes in levee height from the riverbed can be monitored with high accuracy.
- (2) Measurements using the portable laser scanner can obtain an accuracy of 0.3 m even with the method of self-positioning by SLAM which is a low-cost hardware configuration. Since the accuracy required for aerial laser surveying used in river management is 0.3 m, we proved that it can be used as simple and low-cost measurements instead of aerial laser surveying. In particular, we found that because 3D data of levees can be obtained by walking on the levee crown or slope, the detailed measurement of shapes such as sluice gates and foot protection were obtained at the level of accuracy required to detect deformations. In river management, the accuracy required for measuring river management facilities and permitted structures is  $\pm 0.3$  m. Therefore, the portable laser scanner is effective for measuring the deformation of river structures.

SLAM is known to have the problem of accumulating position estimation errors with walking, which was observed in this study; thus, it is necessary to further investigate this error when measuring long distances. In addition, measurement using a drone requires processes such as optimal trajectory analysis using GNSS and IMU data to calculate the flight trajectory after measurement, which can problematize real-time measurements and requires further investigation. In the future, we aim to identify solutions to the problems that arise in the practical application of portable laser measurements and laser drone surveys, including the development of high-density point cloud superposition technology.

## References

- Fuentes-Pacheco, J., Ruiz-Ascencio, J., Rendón-Mancha, J.M.: Visual simultaneous localization and mapping: a survey. *Artif. Intell. Rev.* **43**(1), 55–81 (2012). <https://doi.org/10.1007/s10462-012-9365-8>
- Zou, D., Tan, P., Yu, W.: Collaborative visual SLAM for multiple agents: a brief survey. *Virt. Real. Intell. Hardw.* **1**(5), 461–482 (2019)
- Itsukushima, R.: Countermeasures against floods that exceed design levels based on topographical and historical analyses of the September 2015 Kinu River flooding. *J. Hydrol. Reg. Stud.* **19**, 211–223 (2018)
- Smith M. W.: Direct acquisition of elevation data: Terrestrial Laser Scanning. *Geomorphological Techniques*, chap. 2, sec. 1.5 (2015)
- Gallay, M.: Direct Acquisition of Data: Airborne laser scanning. *Geomorphological Techniques*, chap. 2, sect. 1.4 (2013)
- Nishimura, S., et al.: Disaster report of 2018 July heavy rain for geo-structures and slopes in Okayama. *Soils Found.* **60**(1), 300–314 (2020)
- Javanmardi, E., Javanmardi, M., Gu, Y., Kamijo, S.: Factors to evaluate capability of map for vehicle localization. *IEEE Access* **6**, 49850–49867 (2018)
- Jo, K., Kim, C., Sunwoo, M.: Simultaneous localization and map change update for the high definition map-based autonomous driving car. *Sensor* **18**(9), 3145 (2018)
- Bailey, T., Durrant-Whyte, H.: Simultaneous Localization and Mapping (SLAM): Part II. *IEEE Robot. Autom. Mag.* **13**(3), 108–117 (2006)



# Modeling of Pervious Pile-Supported Embankment Under the Consolidation Process

Yanrou Guo<sup>(✉)</sup>, Jessica U. N. Jeong, Zan Zhou, and Thomas M. H. Lok

Department of Civil and Environmental Engineering, University of Macau, Macau SAR, China

**Abstract.** Pile supported and geosynthetics reinforced embankments are widely used in construction in recent years, especially for highway and high-speed railway as an effective method to improve the bearing capacity and to reduce the settlement of the foundation. As an improvement, pervious piles can be used as drainage elements in addition to vertical reinforcement as they can increase both the rate of consolidation and the bearing capacity of soft foundations. The purpose of this study is to investigate the behaviour of pervious pile-supported embankment during the consolidation process. A series of finite element models were established using the software PLAXIS to investigate the consolidation of soft soil. It was observed that the variation of stress concentration from soil to the pile is consistent with the consolidation of the foundation soil. In general, the rate of consolidation affects the rate of stress concentration. Parametric study showed that the larger the modulus ratio of the pile and the soil, the larger the stress acting on the pile, and the absolute size of the pile has a greater influence on stress distribution between soil and pile than the relative volume of pile and soil has.

**Keywords:** Pervious pile · Consolidation · Stress concentration

## 1 Introduction

A pile-supported embankment is an effective solution for construction over soft soils that have a low bearing capacity. It has been widely used in many countries in recent years (Low et al. 1994; Quigley and Naughton 2007; Jiang et al. 2008; Han et al. 2014; Zhang et al. 2018; Huang et al. 2019). The construction of embankment over soft soil poses many difficulties such as excessive settlement and low bearing capacity. There are many different techniques for soil improvement but with the combination of piles and geosynthetics for reinforcement, rapid construction of embankment over soft soils can take place. As an improvement, pervious piles can be used as drainage elements in addition to vertical reinforcement as they can increase both the rate of consolidation and the bearing capacity of soft foundations (Suleiman et al. 2014; Zhang et al. 2016). Pervious piles, with high stiffness and high permeability, can dissipate the excess pore-pressure generated by the embankment load at a quicker rate, making them especially suitable for reinforcing soils and accelerate consolidation for soil with low bearing capacity and permeability.

In this study, a finite element model was established in PLAXIS 3D to investigate pervious piled-supported embankments. Consolidation of the soil is especially important



in this study as it plays a major role in the arching of the soil (Zhuang and Wang 2017), which enables the effective transfer of stress to the piles. Different factors such as pore pressure, degree of consolidation, and the soil arching of the embankment will be analyzed for detailed investigation.

## 2 Modeling of the Unit Cell by PLAXIS 3D

The simulation of the pile-supported embankment is based on a unit cell consisting of a square prism of soil with one-quarter of a pervious pile at each of its corners as shown in Fig. 1. To verify the numerical model, a series of verification by comparing the results obtained from the PLAXIS model and that from existing analytical solutions are made. The consolidation of the foundation with pervious piles installed in a square pattern is modeled like a foundation with vertical drains installed. The analytical solutions for one-dimensional consolidation and radial consolidation with vertical drains were well established by Terzaghi (1943) and Hansbo (1981), respectively. Zeng and Zie (1989) also proposed an improved solution for vertical drains with an expression for the degree of consolidation at a certain location in the soil. These solutions were used to verify the numerical model, which was proved to be reliable, and therefore further parametric studies can be done, but the details of the comparison will not be given here due to space limitation.

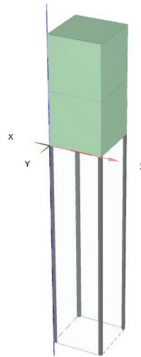
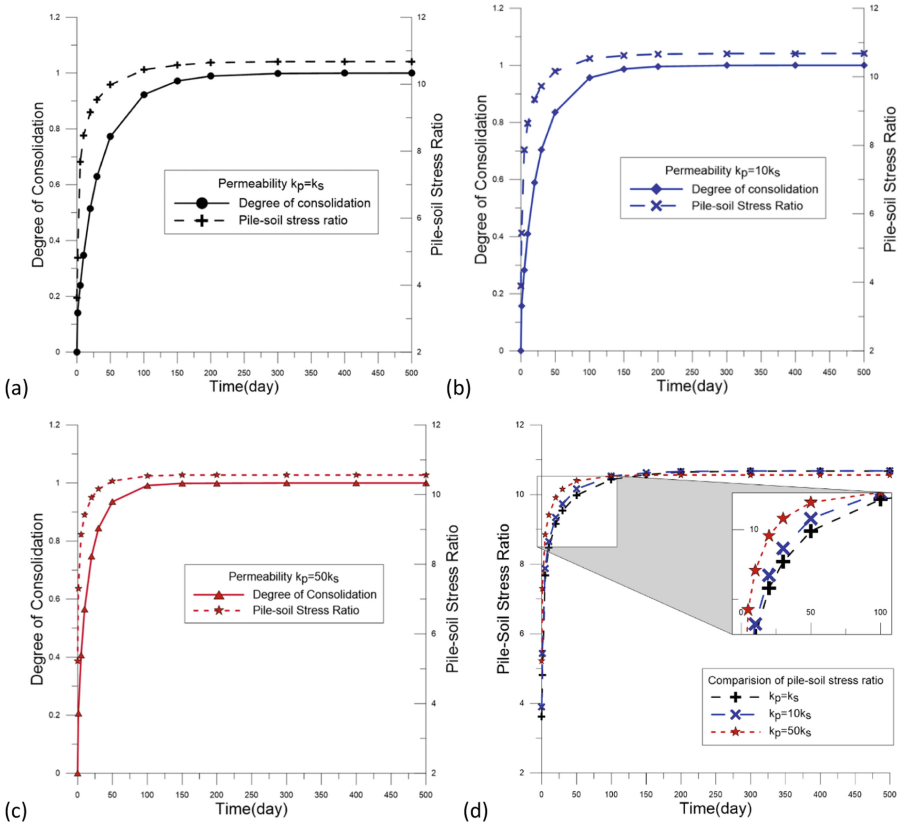


Fig. 1. Unit cell model in PLAXIS 3D

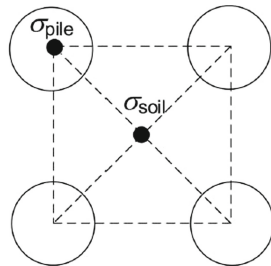
## 3 Influence of the Permeability Ratio

The permeability ratio, defined as  $\frac{k_p}{k_s}$  where  $k_p$  is the permeability of the pile and  $k_s$  is the permeability of the soil, is chosen to be an influencing parameter in the study. Three values of the permeability ratio, 1, 10, and 50, were adopted for the analyses of the model. For each case, the variations between the average degree of consolidation and the pile-soil stress ratio versus time are shown in Fig. 2 for various permeability ratios. The dashed lines represent the pile-soil stress ratio and the solid lines represent

the average degree of consolidation. The pile-soil stress ratio is defined in Fig. 3 as the ratio of stress in the pile to that at the center of the soil at the ground level (Zhang et al. 2016).



**Fig. 2.** Variation of the average degree of consolidation and the pile-soil stress ratio: (a) permeability ratio = 1; (b) permeability ratio = 10; (c) permeability ratio = 50; (d) extraction of the curves of pile-soil stress ratio.



$$\text{Pile-soil stress ratio} = \sigma_{pile} / \sigma_{soil}$$

**Fig. 3.** The pile-soil stress ratio

It can be observed from Fig. 2(a) that, the curve representing the pile-soil stress ratio increases rapidly in early days and reaches to the peak at about 150 days corresponding to 95% degree of consolidation and then the value of the stress ratio remains unchanged until the consolidation process finishes. The other two curves also have a similar trend, except the time for a 95% degree of consolidation because of the difference in permeability. Additionally, the curves of the stress ratio and the degree of consolidation have similar trends, thus, implying that the transformation of stress from the soil to the pile is mainly due to the consolidation and settlement of the soil.

In addition, the ultimate stress concentration ratio when the consolidation process is over can be observed in Fig. 2(d). Through comparing the ultimate stress concentration ratio with different permeability ratios, it can be concluded that the rate of consolidation will not affect the ultimate value of the stress concentration ratio. In Fig. 2(a) to (c), the three curves have a different rate from 0 to nearly 100 days because of the different permeability ratio, but they achieve the same value of the pile-soil stress ratio at the end, implying the ultimate stress concentration efficiency being independent of the rate of consolidation. In conclusion, the results show that the value of permeability gives rise to the consolidation rate but does not affect the ultimate value of the stress concentration ratio.

#### 4 Influence of the Area Replacement Ratio

For group piles in a rectangular pattern of spacing,  $s$ , assuming each pile of diameter,  $d$ , sharing the same influence zone of diameter,  $d_e$ , in the foundation, the area replacement ratio,  $m$ , of the composite foundation can be calculated as (Table 1):

$$m = \frac{d^2}{d_e^2} \quad (1)$$

$$d_e = 1.13s \quad (2)$$

**Table 1.** Parameters for area ratio of the model

Area replacement ratio $m = \frac{d^2}{d_e^2}$	Pile diameter (m)	Pile spacing (m)
$m = \frac{0.3^2}{(1.13 \times 2.4)^2} = 0.012$	0.3	2.4
$m = \frac{0.6^2}{(1.13 \times 4.8)^2} = 0.012$	0.6	4.8
$m = \frac{0.6^2}{(1.13 \times 2.4)^2} = 0.049$	0.6	2.4
$m = \frac{1.2^2}{(1.13 \times 4.8)^2} = 0.049$	1.2	4.8

The comparison of the vertical stress in the pile at depths from 1m to 9m when the consolidation process is nearly over is shown in Fig. 4. As shown in Fig. 4(b), When the area replacement ratio is larger ( $m_2 = 0.049$ ), the variation of the vertical stress in the pile with the depth is smaller, and the difference between the models with different pile diameters has also become smaller.

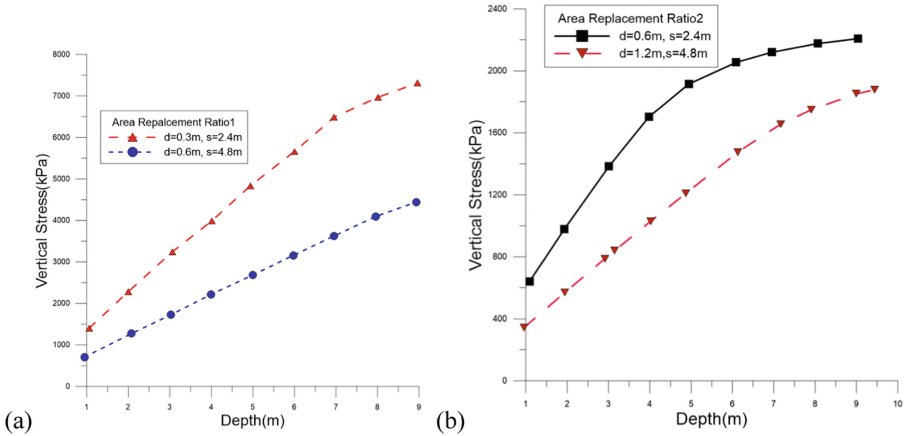


**Fig. 4.** Vertical stress vs. depth of the pile (a) area replacement ratio  $m_1 = 0.012$ ; (b) area replacement ratio  $m_2 = 0.049$ .

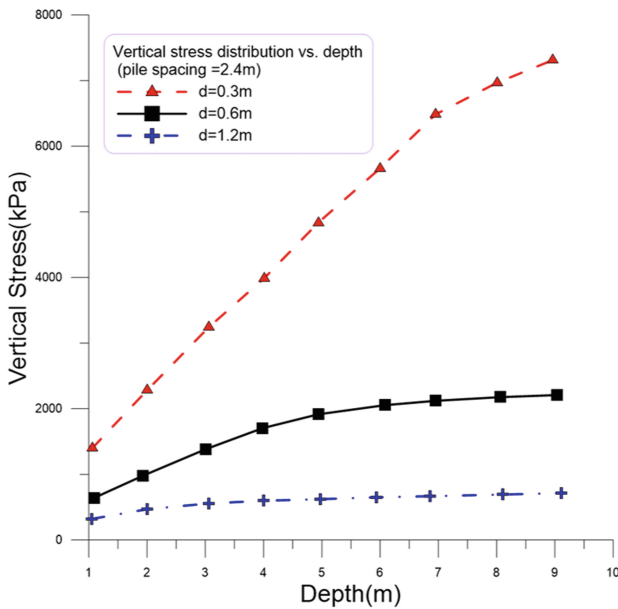


**Fig. 5.** Comparison of vertical stress distribution vs. the depth with different diameters of the pile.

Figure 5 shows the variation of vertical stress with depth of the pile for three different pile diameters of 0.3 to 1.2 m. The foundation volume is kept constant by adopting a constant pile spacing of 2.4 m and a constant thickness of the soil layer of 10 m. With this configuration, the influence of the diameter of the pile as well as the area replacement ration can be observed. In general, the vertical stress in the pile increases with decreasing pile diameter, which implies higher stress concentration is caused by lower area replacement ratio. Further, it can be seen from Fig. 5, the vertical stress in the pile increases with the depth almost linearly in the first half of the pile, and the rate decreases after passing a certain depth.

### 5 Influence of the Modulus Ratio

The Modulus Ratio, defined as  $\frac{E_p}{E_s}$ , where  $E_p$  and  $E_s$  are Young’s modulus of the pile and the soil, respectively, is chosen as an influencing parameter, for which the values adopted in this study are shown in Table 2.

**Table 2.** Young’s Modulus of the pile and the soil

Modulus ratio = $\frac{E_p}{E_s}$	Modulus of the pile (MPa)	Modulus of the soil (MPa)
20	100	5
100	500	5
200	1000	5
500	2500	5
1000	5000	5
2000	10000	5
2400	12000	5
500	500	1
500	12000	24

Figure 6 reveals that the pile-soil stress ratio increases with the time which implies the formation of the soil arch during the consolidation process. For further comparison, the ultimate value of the pile-soil stress ratio will be plotted against the different modulus ratios in Fig. 7. It can be observed that when the modulus ratio exceeds a certain value around 200, further increasing the modulus of the pile has almost no influence on the load transferring from soil to the pile due to the large stiffness contrast between the pile and the soil.

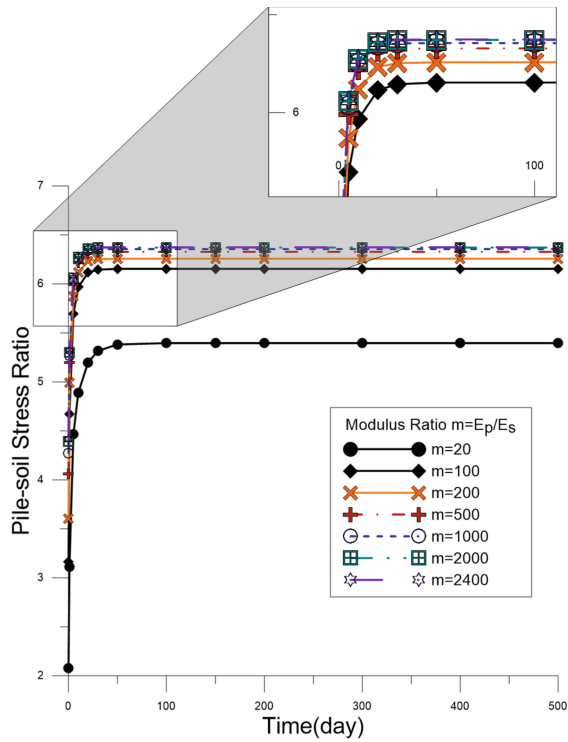


Fig. 6. The variation of pile-soil stress ratio with time.

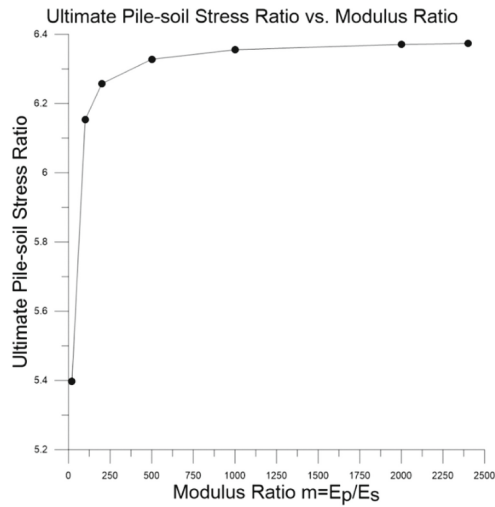


Fig. 7. Relationship of the ultimate pile-soil stress ratio and the modulus ratio.

## 6 Conclusions

Numerical analyses were performed to investigate the behavior of pervious pile-supported embankment during consolidation. It is observed that the evolution of stress concentration from the soil to the pile is consistent with the consolidation process. When the degree of consolidation reached 95%, the increase of the pile-soil stress ratio slows down and approaches stability, which is consistent with the completion of consolidation.

Two groups of models with different area replacement ratios were established by changing the diameter of the pile and the pile spacing accordingly. When the area replacement ratio is smaller, the difference of the vertical stress in the pile is larger. The vertical stress in the pile increases as the diameter of the pile decreases even if the area replacement ratio is the same.

The parametric study on the modulus ratio indicates that the greater the modulus ratio the larger the stress in the pile. When the modulus ratio reaches a certain value around 200 times, further increasing the pile modulus has a small influence on the stress distribution.

In general, the rate of consolidation affects the rate of stress concentration. The absolute size of the pile has a greater influence on stress transferring from the soil to the pile than the area replacement ratio and the pile spacing.

## References

- Han, G.X., Gong, Q.M., Zhou, S.H.: Soil arching in a piled embankment under dynamic load. *Int. J. Geomech.* **15**(6) (2014)
- Hansbo, S.: Consolidation of fine-grained soils by prefabricated drains. *Proc. 10th ICSMFE* **3**, 677–682 (1981)
- Huang, Z.Y., Ziotopoulou, K., Filz, G.M.: 3D numerical limiting case analyses of lateral spreading in a column-supported embankment. *J. Geotech. Geoenviron. Eng.* **145**(11), 04019096 (2019)
- Jiang, X., Ling, J.M., Qiu, Y.J.: FEA of large deformation consolidation for reinforced embankment on soft soil. *Chinese J. Undergr. Space Eng.* **4**(1), 66–72 (2008)
- Low, B.K., Tang, S.K., Choa, V.: Arching in piled embankments. *J. Geotech. Eng.* **120**(11), 1917–1938 (1994)
- Quigley, P., Naughton, P.J.: Design of piled embankments. In: *Proceedings of Conference on soft ground engineering*, Geotechnical Society of Ireland, 2–3 (2007)
- Suleiman, M.T., Ni, L., Raich, A.: Development of pervious concrete pile ground-improvement alternative and behavior under vertical loading. *J. Geotech. Geoenviron. Eng.* **140**(7), 04014035 (2014)
- Terzaghi, K.: *Theoretical Soil Mechanics*. Wiley, New York (1943)
- Zeng, G.X., Xie, K.H.: New development of the vertical drain theories. *Congrès International de Mécanique des Sols et des Travaux de Fondations* **12**, 1435–1437 (1989)
- Zhang, J., Cui, X.Z., Huang, D., Jin, Q., Lou, J.J., Tang, W.Z.: Numerical simulation of consolidation settlement of pervious concrete pile composite foundation under road embankment. *Int. J. Geomech.* **16**(1), B4015006 (2016)
- Zhang, L., Zhou, S., Zhao, H., Deng, Y.: Performance of geosynthetic-reinforced and pile-supported embankment with consideration of soil arching. *J. Eng. Mech.* **144**(12), 06018005 (2018)
- Zhuang, Y., Wang, K.Y.: Analytical solution for reinforcement piled embankment on elastoplastic consolidated soil. *Int. J. Geomech.* **17**(9), 06017010 (2017)



# Seismic Response and Fragility Estimates of Highway Bridges Considering Various Modeling Uncertainty Parameters

Huihui Li<sup>1</sup>(✉), Lifeng Li<sup>2</sup>, and Liang Xu<sup>3</sup>

<sup>1</sup> Department of Civil Engineering, The City College of New York, New York, NY, USA  
hli004@citymail.cuny.edu

<sup>2</sup> College of Civil Engineering, Hunan University, Changsha, China

<sup>3</sup> College of Civil Engineering, Chongqing University, Chongqing, China

**Abstract.** This paper proposes an alternative seismic assessment framework considering various modeling uncertainty parameters, and investigates their effects on the seismic response and seismic fragility estimates of a case-study bridge. Firstly, sensitivity analyses with the tornado diagram technique are performed to determine the sensitivity of some typical bridge engineering demand parameters (EDPs) to twenty-two modeling related uncertain parameters, and the results indicate that the variability in ten identified critical parameters has significant effects on the bridge EDPs. Subsequently, based on a series of nonlinear time history analyses (NLTHAs) on the sample models generated by using Latin hypercube sampling (LHS) method, comparative studies for the seismic responses of some typical bridge members and the seismic fragility estimates both at bridge component and system levels incorporating different levels of uncertainty are performed, respectively. It is concluded that (1) the uncertainty of the modeling related parameters may lead to the difference in the trajectory of seismic response for a given bridge member, whereas the variation of the peak value of such seismic response may due to the joint actions of the uncertainty of ground motions and modeling parameters; (2) the inclusion of only ground motion uncertainty is inadequate and inappropriate, and the proper way is incorporating the uncertainty in those identified significant modeling parameters and ground motions into the seismic response and seismic fragility assessment of highway bridges.

**Keywords:** Bridges · Seismic fragility analysis · Modeling uncertainty parameters · Sensitivity analysis

## 1 Introduction

Various sources of uncertainty, such as structural geometric, material, and boundary conditions related parameters may exist due to the structure-to-structure (STS) variation in the seismic fragility assessment of highway bridges (Padgett and DesRoches 2007; Mangalathu and Jeon 2018). Based on the work done by Kiureghian and Ditlevsen (2009), all sources of uncertainty can be categorized into either aleatory uncertainty



or epistemic uncertainty. The former mainly stems from the intrinsic randomness of ground motions, material, static or dynamic forces, and geometric parameters, whereas the latter may derive from the incomplete of statistic data, lack of human knowledge, and several modeling assumptions. One may either ignore the critical uncertain parameters which could lead to the unreliable seismic fragility assessment; or conversely may devote efforts unnecessarily to the computationally expensive simulations which have minimal effects on the seismic response and seismic vulnerability estimates of highway bridges (Padgett and DesRoches 2007). Thus, there is a need for a schematic sensitivity analysis to investigate the effects of the input uncertain parameters and identify the critical parameters on the seismic response and seismic fragility estimates of highway bridges.

Recently, significant research efforts have focused on the investigations of the sensitivity of seismic response and seismic fragility of highway bridges to parameter uncertainty. For example, Padgett and DesRoches (2007) evaluated the sensitivity of seismic responses for some critical bridge components to the uncertainty in the modeling related uncertain parameters, structural geometries, and ground motions by an analysis of variance (ANOVA) technique. Afterward, the sensitivity study was further extended by Padgett et al. (2010) to evaluate the relative importance of 13 random variables on the seismic reliability of critical structural components for steel bridges. Likewise, by taking the steel-concrete composite (SCC) bridges with a dual load path as case-study bridges, Tubaldi et al. (2012) investigated the sensitivity of seismic response and seismic fragility assessment of SCC bridges to the uncertainty in ground motions and 23 modeling related uncertain parameters. They suggested that it is significant to consider the influence of the variability in modeling related uncertain parameters on the safety of SCC bridges. Pang et al. (2014) studied the influence of different sources of uncertainty on the seismic fragility estimates of a cable-stayed bridge, and they found that the seismic vulnerability of the cable-stayed bridge considering the uncertainty in ground motions, structural geometry, and material parameters is more severe than that considering only the uncertainty in ground motions. Similarly, based on a multiparameter fragility model using the Lasso regression technique, Mangalathu and Jeon (2018) found that ignoring the uncertainty in the critical parameters identified from the sensitivity analysis may lead to inaccurate estimates of seismic demand models and seismic fragilities. Therefore, the above-mentioned studies highlight the importance of sensitivity study of the seismic response and fragility estimates of highway bridges to the uncertainty in modeling related uncertain parameters.

The objective of the present study is to (i) identify the critical modeling parameters that impose significant effects on the seismic demand models of the case-study bridge through the sensitivity analysis; (ii) investigate the influence of different levels of uncertainty on the seismic response and seismic fragility estimates of highway bridges; and (iii) suggest an appropriate framework to treat the uncertainty of modeling related uncertain parameters in the seismic response and vulnerability estimates of the highway bridges. Therefore, the current study is organized into several sections. Following this introduction, Sect. 2 focuses on the introduction of the proposed seismic fragility assessment framework considering various modeling related uncertain parameters. Then, Sect. 3 presents the basic information regarding the numerical modeling of

the case-study bridge and summarizes the probabilistic models of 22 modeling related uncertain parameters from three aspects. Subsequently, Sect. 4 performs the sensitivity study of some typical bridge EDPs of the case-study bridge to these 22 modeling parameters and obtains 10 critical parameters through sensitivity analysis with the tornado diagram technique. Next, Sect. 5 investigates the effects of different levels of uncertainty impose on the seismic responses and seismic fragilities both at bridge component and system levels of the case-study bridge. Finally, this study ends with a summary of conclusions in Sect. 6.

## 2 Seismic Fragility Analysis Considering Various Modeling Uncertainty Parameters

Seismic fragility can be generally defined as the conditional probability of the structural seismic demand,  $D$ , exceeding the seismic capacity,  $C$ , under different intensity measure (IM) levels. The seismic fragility function can be represented by the following lognormal cumulative distribution function (Li et al. 2020).

$$P(D > C|IM) = \Phi \left\{ \frac{\ln[S_D/S_{ci}]}{\sqrt{\beta_{DIM}^2 + \beta_{ci}^2}} \right\} = \Phi \left[ \frac{a + b \ln(IM) - \ln(S_{ci})}{\sqrt{\beta_{DIM}^2 + \beta_{ci}^2}} \right] \quad (1)$$

where  $S_D$  is the median structural seismic demand,  $S_{ci}$  is the median structural seismic capacity at  $i^{\text{th}}$  ( $i$  equals 1, 2, 3 and 4) limit state (LS),  $\beta_{DIM}$  is the logarithmic standard deviation of seismic demand, and  $\beta_{ci}$  is the logarithmic standard deviation of seismic capacity at  $i^{\text{th}}$  limit state, respectively.  $\Phi\{\cdot\}$  is the standard normal cumulative distribution function,  $a$  and  $b$  are the regression coefficients that can be obtained from the linear regression analysis. To simplify the seismic fragility function, Eq. (1) can be further expressed as

$$P_f(LS_i|IM) = \Phi \left[ \frac{\ln(IM) - \ln(\lambda)}{\xi} \right] \quad (2)$$

where  $\lambda$  represents the median IM and  $\xi$  is the logarithmic standard deviation of the seismic fragility function. Generally,  $\lambda$  and  $\xi$  can be used as the seismic fragility parameters to evaluate the seismic fragility of highway bridges, which can be represented as

$$\begin{aligned} \lambda &= e^{[\ln(S_{ci}) - a]/b} \\ \xi &= \sqrt{\beta_{DIM}^2 + \beta_{ci}^2} / b \end{aligned} \quad (3)$$

To incorporate various modeling related uncertain parameters within the seismic fragility assessment framework of highway bridges,  $\beta_{DIM}$  can be expressed as

$$\beta_{DIM} = \sqrt{\beta_{RTR}^2 + \beta_{Model}^2} \quad (4)$$

where  $\beta_{DIM}$  can be determined by the probabilistic seismic demand analysis (PSDA);  $\beta_{RTR}$  and  $\beta_{Model}$  represent the deviations due to the uncertainty in ground motions

and modeling related uncertain parameters, respectively. Thus, the logarithmic standard deviation of the seismic fragility function can be computed as

$$\xi = \sqrt{\beta_{RTR}^2 + \beta_{Model}^2 + \beta_{ci}^2} / b \tag{5}$$

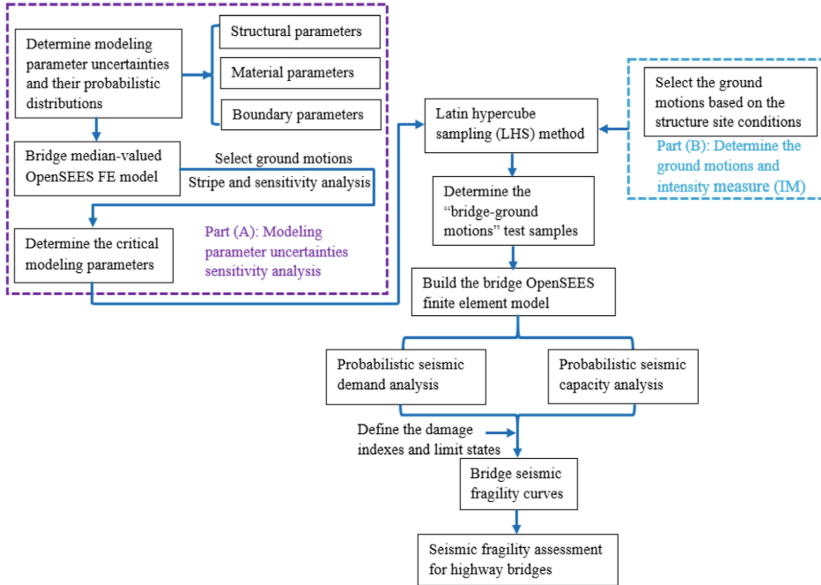


**Fig. 1.** Seismic fragility assessment framework considering various modeling uncertain parameters.

According to the theory of parameter sensitivity analysis with the tornado diagram technique and seismic fragility modeling, Fig. 1 illustrates the proposed seismic fragility assessment framework considering different modeling uncertainty parameters. As shown in Fig. 1, in part (A), three aspects of modeling related uncertain parameters, such as structural geometric, material, and boundary conditions related parameters, are first determined and then utilized to yield the strip analysis through the median-valued OpenSEES model. Based on the strip analysis, some specific tornado diagrams based sensitivity analyses of some typical EDPs to the modeling uncertainty parameters are performed, and the critical modeling parameters can be determined. Subsequently, in part (B), based on the site condition of the case-study bridge, a series of ground motions and the appropriate IM can be determined. Then, to incorporate the record-to-record (RTR) variability in ground motions, the sample bridge structures are randomly paired with the selected seismic records that used for the seismic fragility analysis by using the Latin hypercube sampling (LHS) method, and a series of “bridge-ground motions” samples are generated. Following this, based on the relevant probabilistic seismic demand and capacity analysis from the finite element (FE) model of the case-study bridge built in the OpenSEES, the seismic fragility curves are developed and utilized for deriving the practical estimates of seismic vulnerability of highway bridges.

### 3 Bridge Characteristics and the Modeling Related Uncertain Parameters

#### 3.1 Case-Study Bridge and FE Modeling

The case-study bridge shown in Fig. 2 is a representative multi-span reinforced concrete continuous girder (MSRCCG) bridge, which consists of five spans, 30 m each, and a 16 m wide deck supported by four RC circular piers and two RC abutments. The superstructure consists of a 1.8 m high box girder and a cap beam. The height of each pier is 10 m. According to the guidelines for seismic design of Chinese highway bridges (JTG/TB02-01 2008), each pier is reinforced by longitudinal bars and transverse spiral hoops at a reinforcing ratio of 1.08% and 0.58%, respectively. The bridge utilizes the plate-type elastomeric bearing (PTEB) and the lead rubber bearing (LRB) to transfer the forces from the superstructure to substructure through the piers and abutments. The foundation system of each pier consists of nine RC piles with a diameter of 1.5 m and a length of 30 m, and the soil condition belongs to the medium-hard soil profiles.

A general overview of the simulations of some critical bridge components in the OpenSEES database (Opensees Manual 2009) is provided herein. For instance, the composite action of the deck and cap beam is simulated by using the linear elastic beam-column elements since their damages are not expected in the bridge superstructure during the seismic shaking events (JTG/TB02-01 2008). Bridge piers are modeled using nonlinear beam-column elements with fiber defined cross-sections considering the axial force-moment interaction and material nonlinearities. The stress-strain relationship of the confined and unconfined concrete in RC columns are simulated with Concrete 04 material, whereas the longitudinal steel bars, as well as the transverse spiral hoops, are simulated using the Steel 02 material, both of which are available material models in the OpenSEES database (Opensees Manual 2009). Linear translational and rotational springs are utilized to simulate the pile foundations under the piers to capture the translation and rotation behavior of the foundation system. The stiffness of these springs is determined by the “m” method according to the guidelines for the seismic design of Chinese highway bridges (JTG/TB02-01 2008). Moreover, the PTEB and LRB bearings are simulated by using the elastomeric bearing (plasticity) element, and the behavior of abutments is considered by incorporating the contribution of back-fill soil and piles, which can be modeled by using the hyperbolic material and the hysteretic material in the OpenSEES database (Opensees Manual 2009), respectively. Furthermore, the transverse concrete stoppers are simulated by the hysteretic material and elastic-perfectly plastic gap elements. The pounding effect between the deck and abutments can be simulated using the contact element (i.e., nonlinear translational springs) considering the effects of hysteretic energy loss, which can be simulated by the impact materials in the OpenSEES database (Opensees Manual 2009). Thus, the three-dimensional nonlinear dynamic FE model of the case-study bridge and the force-deformation backbone curves of all critical bridge components are presented in Fig. 2.

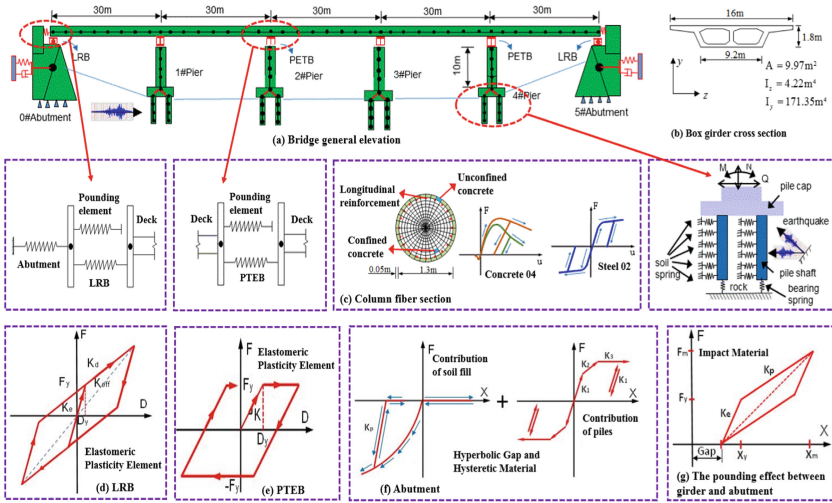


Fig. 2. Nonlinear dynamic FE model of the case-study offshore bridge.

### 3.2 Modeling Related Uncertain Parameters

The modeling related uncertain parameters considered in this paper mainly include three different aspects, such as (i) structurally related uncertainty (SU) parameters, (ii) material related uncertainty (MU) parameters, and (iii) boundary conditions related uncertainty (BU) parameters. Firstly, SU parameters mainly affect the global dynamic characteristics of the bridge structures. From the perspective of structural dynamics, these uncertainties associated with mass, stiffness, and damping can be attributed to this category, but this paper mainly considers the uncertainty parameters that are related to the geometric dimensions of bridge components and damping ratio. Similarly, MU parameters mainly affect the nonlinear response of bridge columns under the earthquake actions. Due to the superstructure and the cap beam are simulated by the elastic beam-column element, this paper mainly considers the material related uncertain parameters of RC columns. In addition, the case-study bridge considers the complicated nonlinear mechanical properties of bearings (i.e., LRB and PTEB), abutments, and pounding between the girder and the abutments. These nonlinear features are of great importance to the seismic analysis of bridge structures. Therefore, it is necessary to consider the BU parameters. To investigate and quantify the significance of different modeling related uncertain parameters, Table 1 summarizes the associated probability distributions of various modeling related uncertain parameters based on some previous studies.

**Table 1.** Statistical information on the modeling related uncertainty parameters

Uncertainty parameters	Description	Distribution	Parameter 1	Parameter 2	Reference
$\lambda_w$	Concrete weight coefficient	Normal	1.04	10%	Wu et al. (2018), Ma et al. (2019)
$D$ (m)	Pier diameter	Normal	1.4	5%	Padgett et al. (2008), Ma et al. (2019)
$c$ (m)	Concrete cover thickness	Normal	0.05	5%	Padgett et al. (2008), Ma et al. (2019)
$\phi$ (m)	Longitudinal reinforcement diameter	Normal	28	5%	Padgett et al. (2008), Ma et al. (2019)
$\xi$	Damping ratio	Normal	0.05	30%	Nielson (2005), Ma et al. (2019)
$E_c$ (MPa)	Young's modulus of concrete	Lognormal	$3 \times 10^4$	14%	Wu et al. (2018)
$f_{c,cover}$ (MPa)	The peak strength of cover concrete	Lognormal	27.58	20%	Barbato et al. (2010)
$\varepsilon_{c,cover}$	Peak strain of cover concrete	Lognormal	0.002	20%	Barbato et al. (2010)
$\varepsilon_{cu,cover}$	The ultimate strain of cover concrete	Lognormal	0.006	20%	Barbato et al. (2010)
$f_{c,core}$ (MPa)	The peak strength of core concrete	Lognormal	34.47	20%	Barbato et al. (2010)
$\varepsilon_{c,core}$	Peak strain of core concrete	Lognormal	0.005	20%	Barbato et al. (2010)
$\varepsilon_{cu,core}$	The ultimate strain of core concrete	Lognormal	0.02	20%	Barbato et al. (2010)
$E_s$ (MPa)	Young's modulus of steel rebar	Lognormal	$2 \times 10^5$	5%	Barbato et al. (2010), Pang et al. (2014)

(continued)

**Table 1.** (continued)

Uncertainty parameters	Description	Distribution	Parameter 1	Parameter 2	Reference
$f_y$ (MPa)	Yield strength of steel rebar	Lognormal	335	10%	Pang et al. (2014)
$\gamma$	Post-yield to initial stiffness ratio	Lognormal	0.02	20%	Barbato et al. (2010)
$\mu_{PTEB}$	The friction coefficient of PTEB	Uniform	0.15	0.25	Wu et al. (2018)
$G_{PTEB}$ (MPa)	Shear modulus of PTEB	Normal	1180	14%	Wu et al. (2018)
$K_{P\_LRB}$ (kN/m)	Post-yield stiffness of LRB	Normal	1500	14%	Wu et al. (2018)
$P_{ult}$ (kN)	Abutment ultimate capacity	Uniform	$0.5P$	$1.5P$	Nielson (2005), Wu et al. (2018)
$K_{Passive}$ (kN/m)	Abutment passive stiffness	Uniform	$0.5K_p$	$1.5K_p$	Nielson (2005), Wu et al. (2018)
$K_{Active}$ (kN/m)	Abutment active stiffness	Uniform	$0.5K_A$	$1.5K_A$	Nielson (2005), Wu et al. (2018)
$K_{eff}$ (kN/m)	Pounding effective stiffness	Lognormal	$1.94 \times 10^6$	14%	Wu et al. (2018)

Note: parameter 1 and parameter 2 represents the mean and coefficient of variation (COV) for the normal and lognormal distributions; lower bound and upper bound for uniform distribution, respectively;  $P$ ,  $K_p$ , and  $K_A$  represent the design value of the abutment ultimate capacity, the abutment passive and active stiffness, and  $P = 10853$  kN,  $K_p = 3.04 \times 10^5$  kN/m,  $K_A = 1.86 \times 10^4$  kN/m

## 4 Sensitivity Analysis of Seismic Response to the Modeling Uncertainty Parameters

### 4.1 Ground Motions Used for the Sensitivity Analysis

According to the guidelines for the seismic design of Chinese highway bridges (JTG/TB02-01 2008), the case-study bridge requires two probabilistic seismic design

levels of E1 and E2. In which, E1 and E2 seismic design levels need the frequent earthquake evaluation and the rare earthquake evaluation. E1 level of seismic design corresponds to the earthquake with a return period of 475 years, while the E2 level corresponds to the earthquake with a return period of 2500 years. For the ground motions used for the sensitivity analysis in this section, this paper selects 22 pairs of far-field strong earthquake records recommended by the US Federal Emergency Management Agency FEMA-P695 Research Report (FEMA 2009) as the input ground motions. These far-field ground motions were originated from the measured records of 14 major earthquakes that took place between 1971 and 1999. The detailed information for these ground motions can be found in the report (FEMA 2009). According to the given requirements in this report, the original ground motions should be first normalized based on the peak ground velocity (PGV) before using these original records. This is because such a standardized process is significant to reduce the effects of uncertainty in ground motions derived from the magnitude, the epicenter distance, and the site categories. Meanwhile, this normalized procedure can still keep the inherent uncertainty of the selected seismic records. Figure 3 displays the scaling of the selected ground motions under the probabilistic seismic design levels of E1 and E2 in the guidelines for seismic design of Chinese highway bridges (JTG/TB02-01 2008).

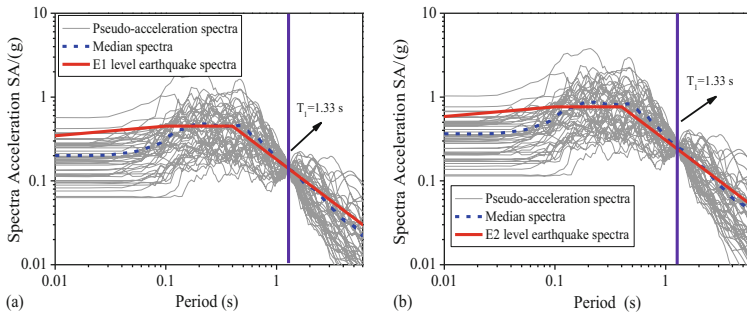


**Fig. 3.** Response spectra of ground motions for sensitivity analysis: (a) E1 level and (b) E2 level.

As shown in Fig. 3, corresponding to the case-study bridge fundamental period of  $T_1 = 1.33$  s, the spectral acceleration (SA) of the selected 22 pairs of ground motions after scaling is matching well with the standard spectral acceleration. It should be mentioned herein that the recommended seismic records in FEMA report (FEMA 2009) are derived from the strong earthquake database of the Pacific Earthquake Engineering Research Centre Ground Motion Database (PEER Ground Motion Database 2015) and each pair of seismic record contains both FP (Fault Parallel) and FN (Fault Normal) directions. Furthermore, due to the differences in spectral characteristics for each pair of seismic record, the corresponding PGA, PGV, and SA are inconsistent and varied. Thus, each pair of the seismic record should be considered as two independent ground motions, and a total of 44 ground motions are utilized for the following sensitivity analysis.



## 4.2 Sensitivity Analysis of Seismic Response to Different Modeling Uncertainty Parameters

It is necessary to investigate the effects of various uncertain parameters on some typical EDPs (as presented in Table 2) of the case-study bridge, and based on a series of previous studies (Porter et al 2002; Celik and Ellingwood 2010; Zhong et al. 2018; Wu et al. 2018), sensitivity analyses of seismic responses for different bridge components to the modeling related uncertain parameters are performed herein using the tornado diagram technique.

**Table 2.** Bridge engineering demand parameters (EDPs)

ID	Seismic demand parameters	Variable	Unit	Note
1	The curvature of the column	$\Phi_L$	m <sup>-2</sup>	Longitudinal
2	The relative displacement of LRB	$\delta_{LRB\_L}$	cm	Longitudinal
3	The relative displacement of PTEB	$\delta_{PTEB\_L}$	cm	Longitudinal
4	Abutment deformation	$\Delta_{Abut\_active}$	cm	Active
5	Abutment deformation	$\Delta_{Abut\_passive}$	cm	Passive

According to the work done by Celik and Ellingwood (2010), Zhong et al. (2018), and Wu et al. (2018), sensitivity analysis with the tornado diagram technique can be performed as following. Firstly, all of the considered modeling related uncertain parameters listed in Table 1 are set equal to their respective median values, and then 44 nonlinear time history analyses (NLTHAs) are conducted to develop the median-valued model for the critical EDPs listed in Table 2. Then, this procedure is carried out repeatedly for each of the 22 modeling related uncertain parameters, in turn, varying only one at a time and setting each parameter to its lower bound (5<sup>th</sup> percentile) and upper bound (95<sup>th</sup> percentile) while holding the remaining parameters at their median values. Furthermore, after a series of NLTHAs are performed, the variation in median values of the seismic responses with each modeling uncertain parameter can be displayed through a tornado diagram (Porter et al 2002; Celik and Ellingwood 2010; Zhong et al 2018). For example, Figs. 4, 5, 6, 7 and 8 illustrate the tornado diagrams for the seismic responses,  $\Phi_L$ ,  $\delta_{LRB\_L}$ ,  $\delta_{PTEB\_L}$ ,  $\Delta_{Abut\_active}$ , and  $\Delta_{Abut\_passive}$ , under E1 and E2 designed levels of ground motions. However, it should be noted that the NLTHAs may fail to converge for some ground motions when they are scaled to a higher seismic hazard event (i.e., E2 design level). For such cases, the maximum likelihood function can be used to estimate the parameters of the lognormal probability distribution (Celik and Ellingwood 2010). This paper presents only a brief introduction of the sensitivity analysis using the tornado diagram technique, interested readers can refer to more relevant works (Celik and Ellingwood 2010; Zhong et al. 2018).

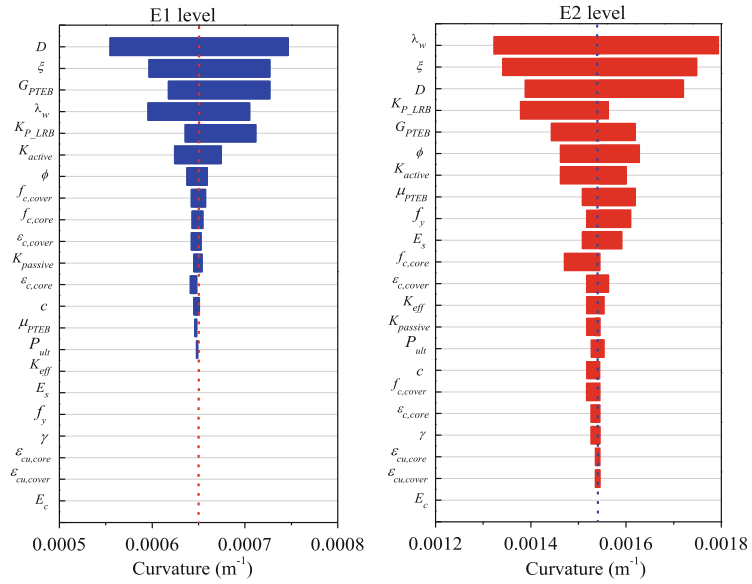


**Fig. 4.** Tornado diagrams for pier curvature ( $\Phi_L$ ) under different levels of ground motions.

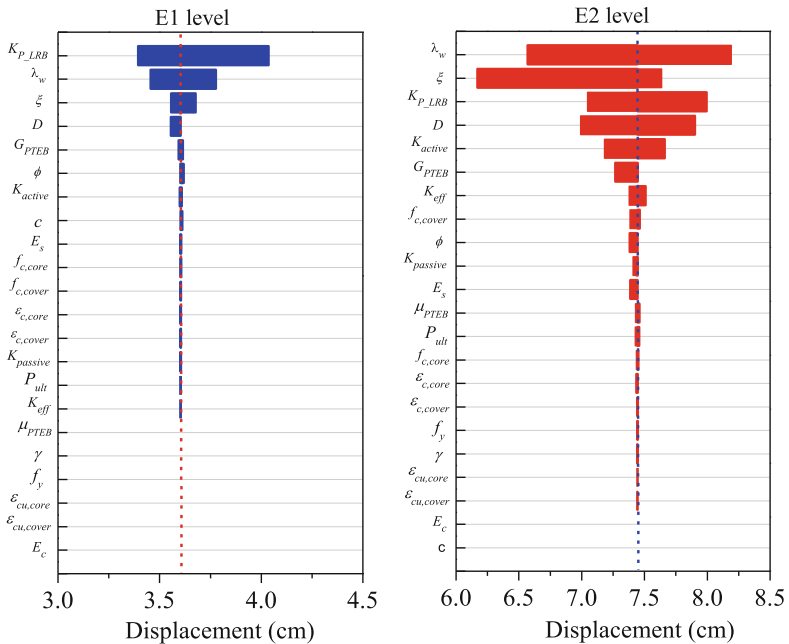


**Fig. 5.** Tornado diagrams for the displacement of LRB ( $\delta_{LRB\_L}$ ) under different levels of ground motions.

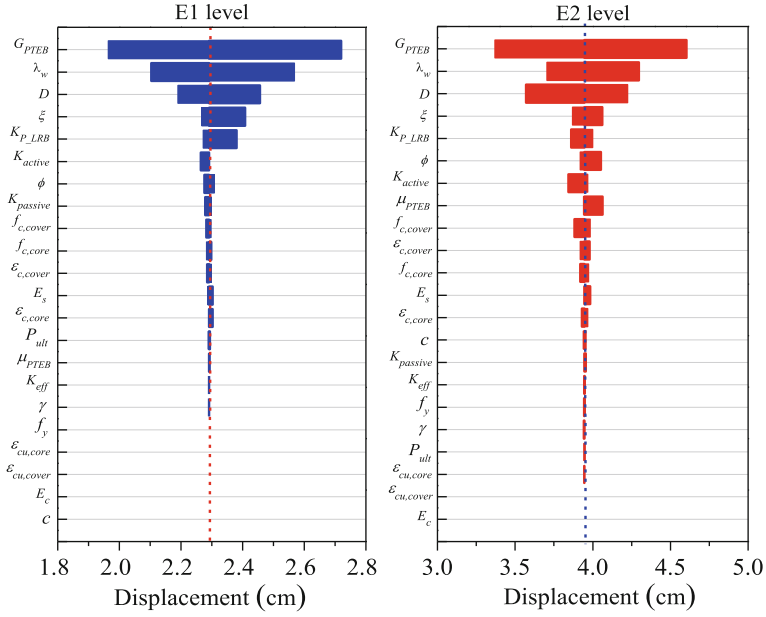


**Fig. 6.** Tornado diagrams for the displacement of PTEB ( $\delta_{PTEB\_L}$ ) under different levels of ground motions.

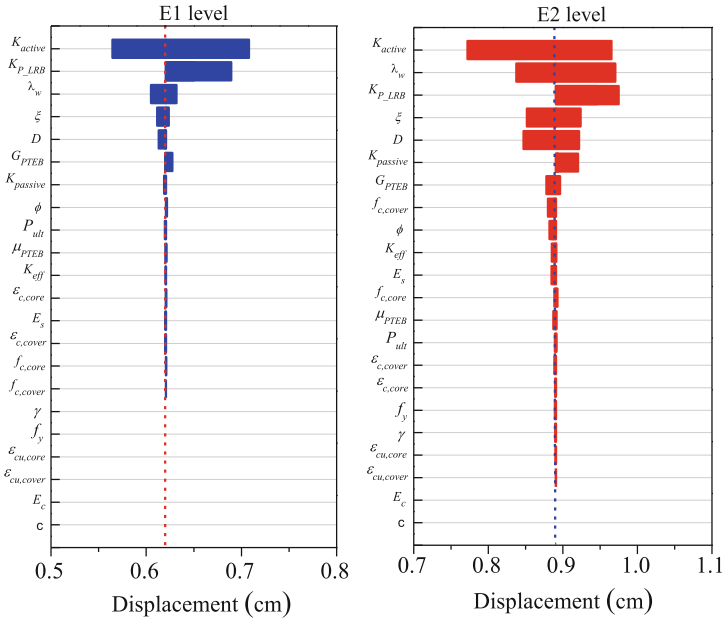


**Fig. 7.** Tornado diagrams for the displacement of abutment-active ( $\Delta_{Abut\_active}$ ) under different levels of ground motions.

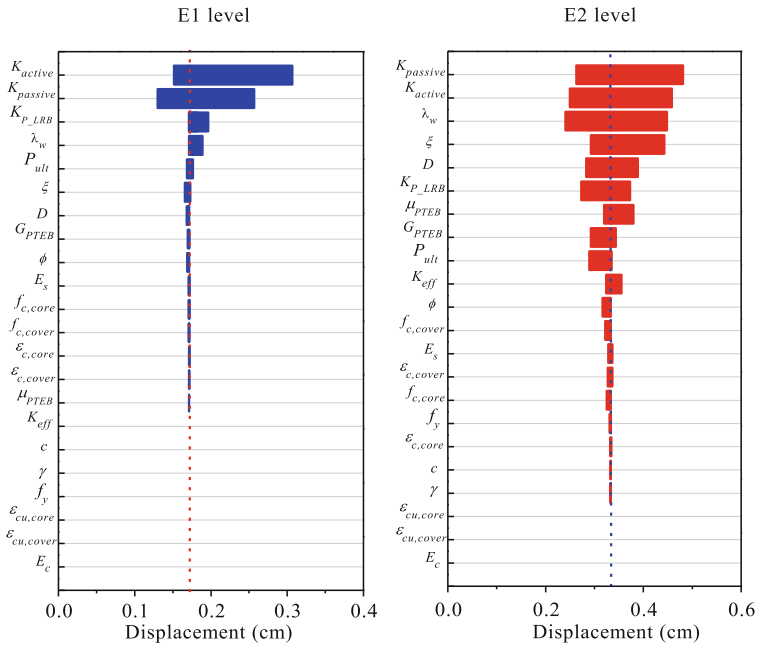


**Fig. 8.** Tornado diagrams for the displacement of abutment-passive ( $\Delta_{Abut\_passive}$ ) under different levels of ground motions.

**Table 3.** Critical modeling uncertain parameters obtained from the sensitivity analysis

ID	Uncertain parameters	Description
1	$\lambda_w$	Concrete weight coefficient
2	$D$ (m)	Pier diameter
3	$\varphi$ (mm)	Longitudinal reinforcement diameter
4	$\xi$	Damping ratio
5	$f_{c, cover}$	The peak stress of cover concrete
6	$\mu_{PTEB}$	The friction coefficient of PTEB
7	$G_{PTEB}$ (MPa)	Shear modulus of PTEB
8	$K_{P\_LRB}$ (kN/m)	Post-yield stiffness of LRB
9	$K_{passive}$ (kN/m)	Abutment passive stiffness
10	$K_{active}$ (kN/m)	Abutment active stiffness

As seen from Fig. 4 to Fig. 8, for a specific tornado diagram, the length of the histogram in a tornado diagram identifies the influential effect of the modeling related uncertain parameter, and the longer the histogram is the more significant of the modeling uncertain parameter is (Celik and Ellingwood 2010). It can be observed from Fig. 4 to Fig. 8 that the effects of different modeling related uncertain parameters impose on the seismic responses of different bridge components are significantly varied. Thus, it is necessary to consider the influence of various modeling uncertainty parameters. Sensitivity analysis through the tornado diagram technique provides new insight into the identification of the critical modeling parameters. By counting the total number of times each modeling parameter has been ranked in the top ten, we can obtain the corresponding critical parameters as summarized in Table 3, while the rest of the random parameters have much smaller or no discernible effects on the seismic responses of the given bridge components. Therefore, these 10 identified critical parameters are suggested to be regarded as random variables, while the uncertainty in the other 12 remaining parameters can be neglected without resulting in a significant loss of accuracy. Thus, these 12 remaining parameters can be set to their median values (deterministic) in the FE models used for the following seismic fragility analysis of the case-study bridge.

## 5 Effects of Modeling Uncertainty Parameters on the Seismic Response and Fragility Estimates of the Case-Study Bridge

### 5.1 Effects of Modeling Related Uncertain Parameters on the Seismic Responses

To qualitatively investigate the influence of various modeling uncertainty parameters on the nonlinear seismic responses of the case-study bridge, Fig. 9 performs a comparative study of seismic hysteretic responses for different bridge components obtained by using the NLTHAs under two different ground motions (i.e., Northridge and Kobe). The acceleration time histories of these two seismic records are displayed in Fig. 10. As shown in Fig. 9, the given nonlinear seismic hysteretic curves with two levels of uncertainty are developed under two different ground motions. In which, uncertainty case 1 and case 2 can be termed as “RTR only” and “RTR+All”, respectively. Case 1 (“RTR only”) incorporates only the uncertainty in the ground motions and set all of the modeling related uncertain parameters listed in Table 1 equal to their median values, while case 2 (“RTR+All”) considers both the uncertainty of ground motions and all of the modeling parameters listed in Table 1. Since all of the modeling related uncertain parameters in case of “RTR only” equal to their respective median values (deterministic), this case herein can be defined as the “Deterministic model”, which only considers the uncertainty in ground motions. However, since all of the modeling related uncertain parameters in case of “RTR+All” are treated as random variables, this case is defined as the “Stochastic model”, which considers both the uncertainty in ground motions and the modeling related uncertain parameters.

As seen from Fig. 9(a1), (b1), (c1) and (d1), for the “Deterministic model”, due to the uncertainty of seismic records, the peak value of nonlinear seismic hysteretic response for each component of the case-study bridge is different, while the trajectory of seismic hysteretic response for each bridge component is almost the same under the action of

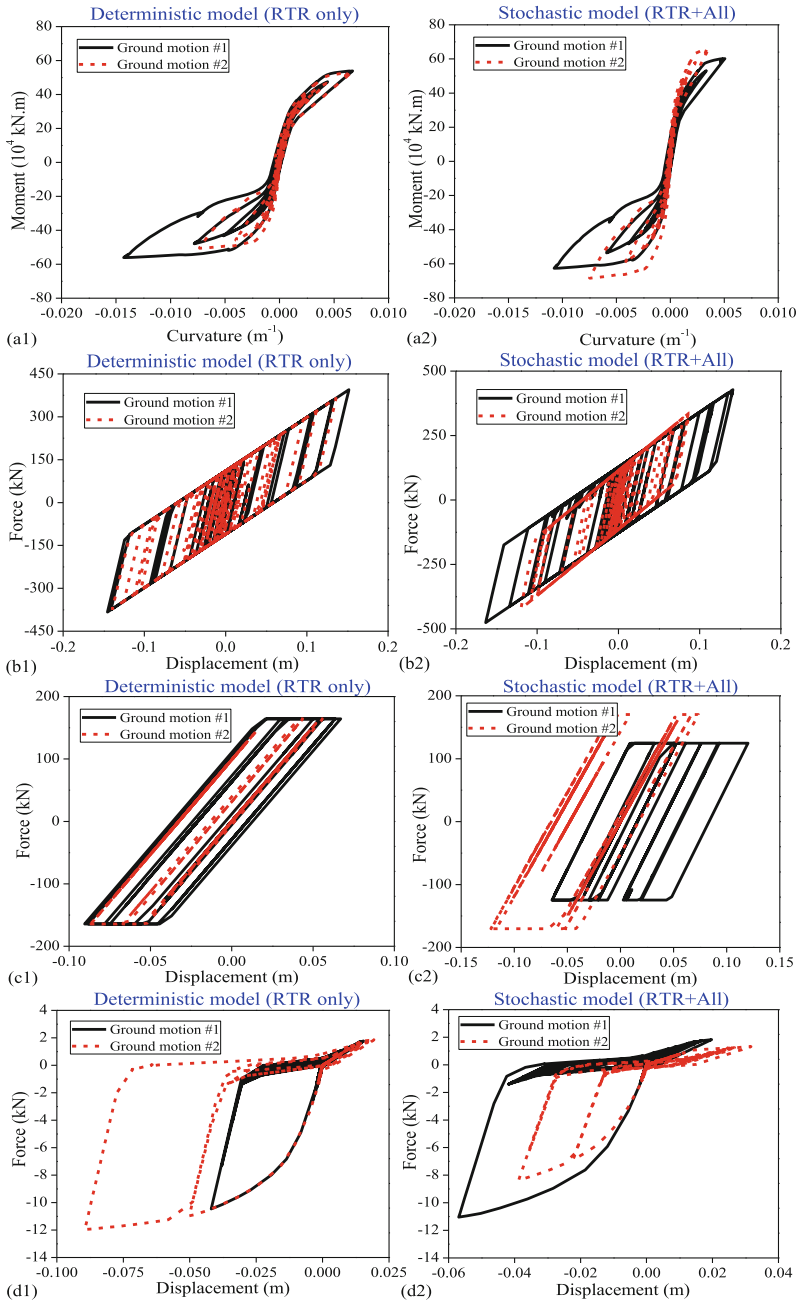


**Fig. 9.** Seismic responses for different components of the pristine case-study bridge under two different ground motions: (a) pier, (b) LRB, (c) PTEB, and (d) abutment.

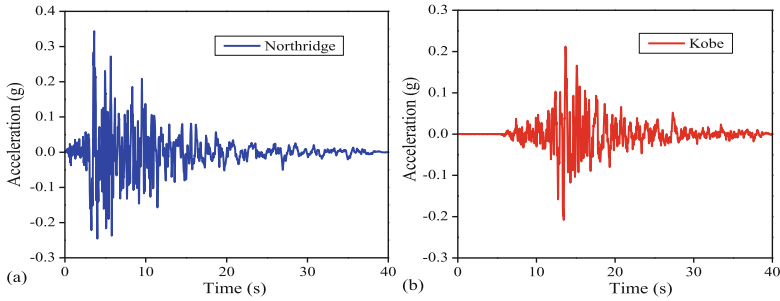


**Fig. 10.** Acceleration time history curve for (a) ground motion #1: Northridge and (b) ground motion #2: Kobe seismic record.

Northridge and Kobe seismic records. However, from Fig. 9(a2), (b2), (c2) and (d2), as for the “Stochastic model”, under the impact caused by the uncertainty both of the ground motions and all of the modeling related uncertain parameters, not only the peak value but also the trajectory of seismic hysteretic response for each bridge member may vary with the input ground motions. These findings indicate that the difference of the trajectory of seismic hysteretic response for a specific bridge component may due to the uncertainty of modeling parameters, whereas the variation of the peak seismic response could be caused by the joint actions of the uncertainty of ground motions and modeling related uncertain parameters.

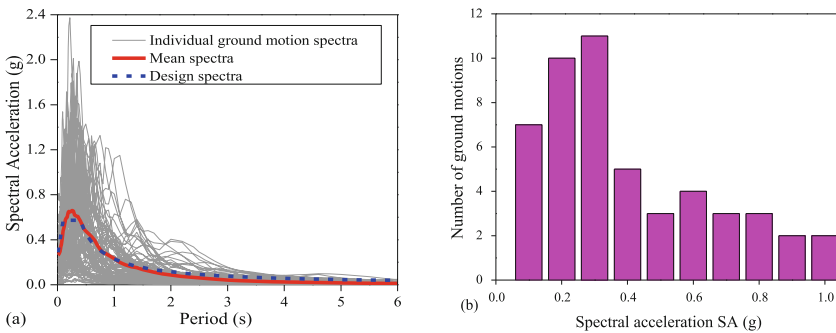


**Fig. 11.** Response spectra of the selected ground motions used for the seismic fragility analysis of the case-study bridge.

## 5.2 Ground Motions and Limit States

The selection of ground motions is critical to provide a good prediction of seismic response for highway bridges. According to the site condition of the case-study bridge, this paper selects 50 pairs of seismic records from the PEER Centre Ground Motion Database (PEER Ground Motion Database 2015) as the input ground motions used for the following seismic fragility analysis. Figure 11(a) shows the response spectra of the

selected ground motions. It is observed that the mean value of the acceleration spectra of the selected seismic records is well matching with the design spectra for the case study bridge (JTG/TB02-01 2008). For the regular RC girder bridges that are similar to the case-study bridge, the seismic response is mainly dominated by the first mode of dynamic analysis. As a consequence, the 5% damped first-mode spectral acceleration (SA) is employed as the intensity measure for the seismic fragility analysis in this study (Li et al. 2020). Figure 11(b) shows the distribution of SA values for the selected ground motions. Thus, it can be observed that the selected seismic records cover a relatively broad range of SA values. For the selected seismic records, their moment magnitudes vary from 6.5 to 7.5 and their hypo-central distances range from 15 and 100 km. This shows that the selected ground motions can represent both small and large earthquakes with different epicentral distances.

**Table 4.** Damage indexes of different bridge components under different limit states.

Components	SL		MO		EX		CO	
	$S_c$	$\beta_c$	$S_c$	$\beta_c$	$S_c$	$\beta_c$	$S_c$	$\beta_c$
$\mu_\phi$	1.0	0.127	2.21	0.246	5.40	0.472	11.12	0.383
$\mu_z$	1.0	0.246	1.5	0.246	2.0	0.472	2.5	0.472
$\gamma_a$	100%	0.246	150%	0.246	200%	0.472	525%	0.472
$\delta_{active}$ (mm)	13	0.246	26	0.246	78	0.472	150	0.472
$\delta_{passive}$ (mm)	5.5	0.246	11	0.246	35	0.472	100	0.472

Within the performance-based earthquake engineering (PBEE) framework, the most widely accepted limit state definitions are proposed by HAZUS (1999), which defines four limit states, such as slight (SL), moderate (MO), extensive (EX) and complete (CO) limit states. According to several previous studies (Nielson 2005; Pan et al. 2007), the ductility factor can be utilized as the damage index of concrete components, whereas for other bridge components, such as abutments and bearings can be indicated by the relative displacement or shear strain. This study considers the damage of RC pier, LRB, PTEB, and abutment. Hence, based on the studies of Nielson (2005), the defined damage indexes under different limit states for different bridge components are summarized in Table 4, where  $\mu_\phi$  is the curvature ductility at the base section of the columns,  $\mu_z$  is the displacement ductility of PTEB,  $\gamma_a$  is the allowable shear strain of LRB,  $\delta_{active}$  and  $\delta_{passive}$  is the active and passive displacement of the abutment, respectively.

### 5.3 Effects of Modeling Related Uncertain Parameters on the Seismic Fragilities

According to the proposed seismic fragility analysis framework in Sect. 2, the seismic fragility curves of different bridge components can be developed as shown in Fig. 12. As seen from Fig. 12, LRB is the most fragile component at the former three limit states, and the failure probability of LRB is much higher than that of PTEB. This may be because the lateral stiffness of piers is less than that of the abutment, so the relative displacement



of LRB under the earthquake excitation is much less than that of PTEB. However, in Fig. 12(d), the failure probability of LRB at CO damage state is less than that of PTEB, which may result from the damage of LRB at this condition is not be determined by the damage of the bearing itself but the girder falling during the seismic shaking events. In addition, it should be noted that the fragility curves of the abutment passive direction at the latter two damage states are relatively flat, which may be a consequence of the complicated pounding effects imposed by the deck and abutments.

Generally, both the seismic fragility curves and fragility parameters ( $\lambda$  and  $\xi$  in Eq. (3)) can be utilized to assess the seismic vulnerabilities of highway bridges. Thus, to investigate the effects of incorporating different levels of uncertainty in modeling related uncertain parameters on the seismic fragility estimates of the case-study bridge, three cases of uncertainty treatment are taken into consideration. Apart from two uncertainty level cases (“RTR only” and “RTR+All”) that have mentioned in Sect. 5.1, a third case termed as “RTR+Critical” is also considered herein. To be specific, “RTR+Critical” incorporates the uncertainty in ground motions along with the uncertainty of these 10 critical parameters (Table 3) identified from the sensitivity analysis, while the other 12 remaining parameters in Table 1 equal to their respective median values. To examine the influence of including different levels of uncertainty in modeling related uncertainty parameters on component seismic fragilities, and due to the failure probabilities for bridge components under EX and CO damage state are relatively small (as seen from Fig. 12), Fig. 13 only compares the median SA (corresponding to 50% failure probability) under SL and MO damage states.

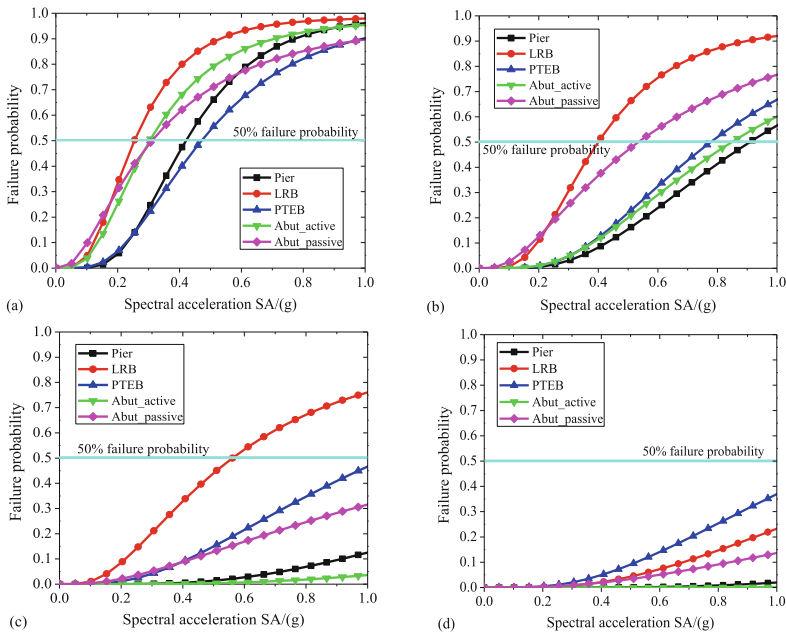


**Fig. 12.** Bridge component seismic fragility curves: (a) SL, (b) MO, (c) EX, and (d) CO damage state.

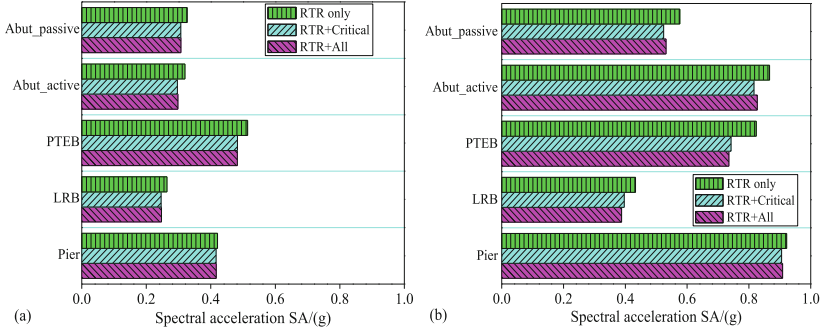


**Fig. 13.** Median SA of different bridge members with different levels of uncertainty: (a) SL (b) MO damage state.

As observed from Fig. 13, compared to the median SA considering only the uncertainty in the ground motions (case “RTR only”), there is a relatively significant difference from those considering additional uncertainty of critical or all modeling related uncertain parameters, and the difference tends to increase with the severity of limit states. However, the difference between the set of fragility parameters (median SA) incorporating the uncertainty in ground motions as well as the critical parameters (case “RTR+Critical”) and those with the additional uncertainty in the remaining 12 parameters (case “RTR+All”) are very little. This indicates that the bridge component seismic fragilities are sensitive to these 10 critical parameters identified in the preceding sensitive analysis but much less sensitive to the remaining 12 modeling parameters. In addition, the influence of uncertainty levels on the seismic fragility of different bridge components is varied. For example, the impact due to different cases of uncertainty treatment on the seismic fragility of the pier is relatively minor to those on other bridge components, such as LRB, PTEB, and abutment.

Similarly, to investigate the effect of different cases of uncertainty treatment impose on the logarithmic standard deviation  $\xi$  in the seismic fragility function, Table 5 shows the uncertainty in the corresponding logarithmic standard deviations of different bridge components. As seen from Table 5, both the deviations result from the uncertainty in ground motions ( $\beta_{RTR}$ ) and modeling related parameters ( $\beta_{Model}$ ) are varied with the bridge EDPs. From an overall perspective,  $\beta_{Model}$  are less than  $\beta_{RTR}$  for all bridge components, and the range for  $\beta_{Model}$  and  $\beta_{RTR}$  of the case-study bridge is 0.251 to 0.456 and 0.310 to 0.671, respectively. Moreover, the fragility parameters ( $\xi$ ) for all bridge components tend to increase with the severity of limit states, and  $\xi$  for both the active and passive direction of abutment are relatively larger than that for other bridge members. This may result from the complicated and nonlinear pounding or impact that occurs between the deck and abutments. However, to investigate the effects imposed by the uncertainty in ground motions and modeling related uncertain parameters on the deviations of different bridge components, Fig. 14 compares the contributions of  $\beta_{RTR}$ ,  $\beta_{Model\_All}$  parameters, and  $\beta_{Model\_Critical}$  parameters on different bridge EDPs. From Eq. (4) in Sect. 2, we can calculate  $\beta_{Model}$  by the following equation as

$$\beta_{Model} = \sqrt{\beta_{D|IM}^2 - \beta_{RTR}^2} \quad (6)$$

**Table 5.** Uncertainty in logarithmic standard deviations for different bridge components.

Component	$\beta_{RTR}$	$\beta_{Model}$	$\beta_{DIM}$	$\beta_{ci}$	$\xi$
Pier	0.310	0.251	0.399	0.127	0.402
				0.274	0.463
				0.321	0.488
				0.383	0.529
LRB	0.247	0.198	0.317	0.246*	0.473
				0.472**	0.675
PTEB	0.284	0.224	0.362	0.246*	0.522
				0.472**	0.714
Abut_active	0.389	0.339	0.516	0.246*	0.725
				0.472**	0.856
Abut_passive	0.671	0.456	0.811	0.246*	0.753
				0.472**	0.828

Note: where  $\beta_{DIM} = \sqrt{\beta_{RTR}^2 + \beta_{Model}^2}$ ,  $\xi = \sqrt{\beta_{DIM}^2 + \beta_{ci}^2}/b$ ; “\*” represents the deviations for SL and MO damage states, and “\*\*” denotes the deviations EX and CO damage states

where  $\beta_{DIM}$  can be obtained by PSDA and when  $\beta_{DIM}$  equals to  $\beta_{RTR}$ ,  $\beta_{Model}$  equals 0. This corresponds to the case of uncertainty treatment (“RTR only”) when all the modeling related uncertain parameters are set to their median values.  $\beta_{Model\_All}$  parameters and  $\beta_{Model\_Critical}$  parameters can be determined through Eq. (6) by considering the uncertainty in all of the modeling parameters or only the critical modeling related parameters. As shown in Fig. 14, for all bridge members, compared to the influence of  $\beta_{RTR}$  on different bridge EDPs, there is a relatively significant difference from those of  $\beta_{Model}$ . However, the differences between  $\beta_{Model\_All}$  parameters and  $\beta_{Model\_Critical}$  parameters are very little. This indicates that the deviations are sensitive to these 10 significant modeling parameters but much less sensitive to the remaining 12 parameters.

Likewise, to investigate the effect of modeling uncertainty parameters on the bridge system-level seismic fragility, Fig. 15 compares the seismic fragility curves and the median SA plots with three different levels of uncertainty. As observed from Fig. 15, similar results about the influence generated by different levels of uncertainty in modeling related uncertain parameters on the system-level seismic fragility can be found similar to that on the bridge component-level seismic vulnerability. Therefore, based on the above analysis, the results suggest that the inclusion of only the uncertainty derived from the ground motions (case “RTR only”) may not sufficient to evaluate the seismic fragility of highway bridges, and it is necessary to take into consideration the uncertainty contributions of different modeling related uncertain parameters. The results also indicate that we can reduce the number of NLTHA simulations for PSDA and thereby

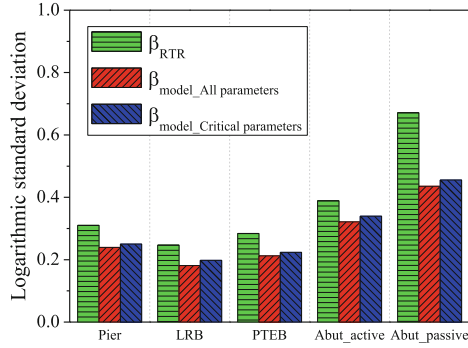


**Fig. 14.** The logarithmic standard deviation of bridge components with a different source of uncertainty.

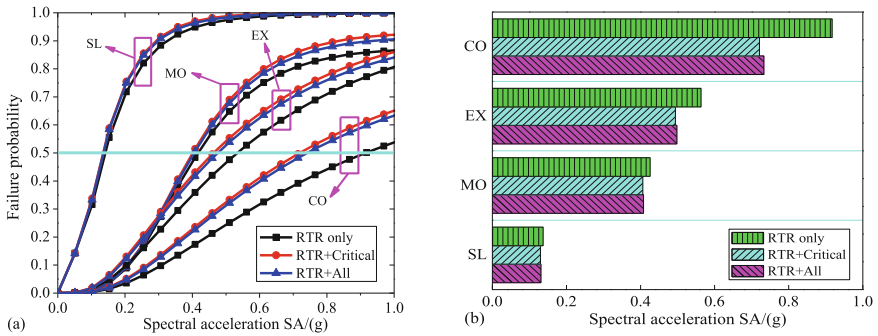


**Fig. 15.** System seismic fragility curve and fragility parameter with different levels of uncertainty.

save time as well as the computational efforts by considering only the critical modeling related parameters identified through the sensitivity analysis in the future seismic fragility assessment of highway bridges. Such a method in identification of significant modeling parameters by sensitivity analysis with the tornado diagram technique helps bridge owners and engineers to identify the critical variables to pay attention to the design and corresponding seismic performance evaluation of highway bridges.

## 6 Conclusion

This paper proposes a schematic seismic fragility assessment framework for highway bridges considering various modeling related uncertain parameters. A total of twenty-two random variables are probabilistically characterized to represent the modeling related uncertain parameters from three different aspects. A variety of bridge EDPs are employed as measures to investigate the sensitivity of the seismic responses of the case-study bridge to these modeling uncertainty parameters. Then, ten critical modeling parameters are identified through the sensitivity analysis with the tornado diagram technique, and these critical parameters are suggested to be treated as random variables, while the remaining

12 parameters can be selected as deterministic by set equal to their respective median values. In addition, the findings of the sensitivity analysis are extended to investigate the influence of incorporating different levels of uncertainty on the seismic response and seismic fragility estimates both at bridge component and system levels. Finally, the following conclusions can be summarized as.

- (1) The difference of the trajectory of seismic hysteretic response for a specific bridge component may vary due to the uncertainty of modeling related uncertain parameters, whereas the variation of the peak seismic response may vary due to the joint contributions of the ground motion uncertainty and modeling parameters variability.
- (2) It is essential to consider the variability of the identified significant modeling parameters from the sensitivity analysis because the uncertainty in these critical parameters has considerable effects on the seismic demand models, seismic response, and seismic fragility estimates of highway bridges.
- (3) The differences of the developed bridge component and system-level seismic fragilities between the case of “RTR+Critical” and “RTR+All” are negligible. Thus, sensitivity analysis with the tornado diagram technique is a good candidate method to identify the critical modeling parameters, and it helps reduce the number of nonlinear simulations and minimizing the computational efforts in the seismic response and fragility estimates of highway bridges.

**Acknowledgements.** This work was financially supported by the National Natural Science Foundation of China (Grants No. 51278183). The authors are very grateful to the financial support.


## References

- Barbato, M., Gu, Q., Conte, J.P.: Probabilistic push-over analysis of structural and soil-structure systems. *J. Struct. Eng.* **136**(11), 1330–1341 (2010)
- Celik, O.C., Ellingwood, B.R.: Seismic fragilities for non-ductile reinforced concrete frames - role of aleatoric and epistemic uncertainties. *Struct. Saf.* **32**(1), 1–12 (2010)
- FEMA: Quantification of building seismic performance factors. Applied Technology Council, Federal Emergency Management Agency: Washington, D.C. (2009)
- HAZUS: Earthquake loss estimation methodology, SR2 edition. National Institute of Building Sciences for Federal Emergency Management Agency, Washington D.C. (1999)
- Kiureghian, A.D., Ditlevsen, O.: Aleatory or epistemic? Does it matter? *Struct. Saf.* **31**(2), 105–112 (2009)
- Li, H., Li, L., Wu, W., Xu, L.: Seismic fragility assessment framework for highway bridges based on an improved uniform design-response surface model methodology. *Bull. Earthq. Eng.* **18**(5), 2329–2353 (2020). <https://doi.org/10.1007/s10518-019-00783-1>
- Ma, H.-B., et al.: Probabilistic seismic response and uncertainty analysis of continuous bridges under near-fault ground motions. *Front. Struct. Civ. Eng.* **13**(6), 1510–1519 (2019). <https://doi.org/10.1007/s11709-019-0577-8>
- Mangalathu, S., Jeon, J.S.: Critical uncertainty parameters influencing the seismic performance of bridges using Lasso regression. *Earthq. Eng. Struct. Dyn.* **47**(3), 784–801 (2018)
- Ministry of Communications of PRC: Guidelines for seismic design of highway bridges (JTG/TB02-01). Beijing: China Communications Press (2008). (in Chinese)

- Nielson, B.G.: Analytical fragility curves for highway bridges in moderate seismic zones. Ph.D. thesis, Georgia Institute of Technology, Atlanta, United States (2005)
- OpenSees Manual: Open system for earthquake engineering simulation user command-language manual. Pacific Earthquake Engineering Research Center, University of California, Berkeley, United States (2009)
- Padgett, J.E., DesRoches, R.: Sensitivity of seismic response and fragility to parameter uncertainty. *J. Struct. Eng.* **133**(12), 1710–1718 (2007)
- Padgett, J.E., Ghosh, J., Dueñas-Osorio, L.: Effects of liquefiable soil and bridge modeling parameters on the seismic reliability of critical structural components. *Struct. Infrastruct. Eng.* **9**(1), 59–77 (2010)
- Padgett, J.E., Nielson, B.G., DesRoches, R.: Selection of optimal intensity measures in probabilistic seismic demand models of highway bridge portfolios. *Earthq. Eng. Struct. Dyn.* **37**(5), 711–725 (2008)
- Pan, Y., Agrawal, A.K., Ghosn, M.: Seismic fragility of continuous steel highway bridges in New York State. *J. Bridge. Eng.* **12**(6), 689–699 (2007)
- Pang, Y.T., Wu, X., Shen, G.Y., et al.: Seismic fragility analysis of cable-stayed bridges considering different sources of uncertainties. *J. Bridge. Eng.* **19**(4), 1–11 (2014)
- PEER Ground Motion Database: PEER (Pacific Earthquake Engineering Research Center) (2015). <http://ngawest2.Berkeley.edu/site>
- Porter, K.A., Beck, J.L., Shaikhutdinov, R.V.: Sensitivity of building loss estimates to major uncertain variables. *Earthq. Spectra.* **18**(4), 719–743 (2002)
- Tubaldi, E., Barbato, M., Dall'Asta, A.: Influence of model parameter uncertainty on seismic transverse response and vulnerability of steel-concrete composite bridges with dual load path. *J. Struct. Eng.* **138**(3), 363–374 (2012)
- Wu, W.P., Li, L.F., Tang, S.H., Zhang, X.H.: Sensitivity investigation of modeling uncertainty for seismic demand analysis of bridges. *J. Vib. Shock.* **37**, 257–270 (2018). (in Chinese)
- Zhong, J., Zhi, X.D., Fan, F.: Sensitivity of seismic response and fragility to parameter uncertainty of single-layer reticulated domes. *Int. J. Steel. Struct.* **18**(5), 1607–1616 (2018)



# Considerations of Vertical Acceleration Induced by Horizontal Earthquake Record for a Building with Underground Stories Based on a SSI 3D Model

Mohammad Amin Mohammadyar<sup>1</sup> and Ali Akhtarpour<sup>2</sup> 

<sup>1</sup> Department of Civil Engineering, Faculty of Engineering, Ferdowsi University of Mashhad, P.O. Box, 91849-95433 Mashhad, Iran

amin.mohammadyar@mail.um.ac.ir

<sup>2</sup> Department of Civil Engineering, Ferdowsi University of Mashhad, P.O. Box, 91779-48974 Mashhad, Iran

akhtarpour@um.ac.ir

**Abstract.** The effects of the vertical earthquake on buildings have typically been less of a concern than the horizontal effects. This is primarily due to the misconception that both the amplitude of the vertical component is smaller than the horizontal component and that the building is stiffer in the vertical direction than in the horizontal direction. The seismic building codes have given less attention to the vertical seismic effect in buildings. In many articles, that have examined the seismic behavior of structures due to horizontal earthquakes without considering soil-structure interaction, the effects of the vertical response of a building to the earthquake are based on the recommendations of codes as a combination of the percentage of dead load and horizontal seismic load or the vertical seismic effect is permitted to be taken as zero for some conditions. Seismic accurate analysis of structures due to the complex dynamic behavior of the soil and SSI, involves consideration of the simultaneous modeling and dynamic analysis of soil and structure. The present study investigated the effects of SSI on the vertical acceleration components of earthquakes by taking time history analysis for three records using ABAQUS software. To achieve this, vertical acceleration induced by horizontal earthquakes record for a 13-storey building with four underground ones, were examined by comparing the results of the time history analysis with or without considering soil. The results show that the effect of SSI on the vertical acceleration component of earthquakes of the building was generally significant.

**Keywords:** Vertical component of earthquakes · Soil-structure interaction · Time history analysis

## 1 Introduction

Soil-structure interactions have been the main issue in designing heavy and hard structures with deep foundations such as the offshore platforms, high-rise buildings, and

nuclear power plants. However, it is usually assumed in the dynamic analysis of structures that there is a bedrock under the foundation; hence, soil-structure interaction effects are ignored. In this case, the structural response is affected only by the dynamic properties of the structure so that soil flexibility will have not any impact on the structure's response. However, previous evidence and experiences indicate that the structural response is influenced by the dynamic properties of the soil, foundation, and structure, which is in contrast with the assumption of bedrock under the foundation (Venanzi et al. 2014). Soil-structure interaction plays a vital role in the dynamic behavior of them under the external forces or seismic waves. The nature and rate of this mutual effect not only depends on the soil rigidity but also on the stiffness and mass of the structure (Ucak and Tsopelas 2008). Vibrations affecting the structures depend on various parameters such as effects of earthquake focus, waves' travel path, site, and soil-structure interaction (Stewart et al. 1998). Therefore, it is essential to take into account the soil-structure interaction in order to find the real response and predict the behavior of structure (Venanzi et al. 2014).

It is assumed that is enough to consider the impact of the horizontal component of earthquakes in seismic analysis of structures but it has been proved in reports associated with destructive earthquakes and studies related to the near-field earthquakes that the vertical component is as important as the horizontal one (Papazoglou and Elnashai 1996). Researchers carried out a study on the altering spectrum vertical to horizontal acceleration ratio and found that this ratio in long periods is smaller than short corresponding values (Bozorgnia and Niazi 1993). Another research studied the properties of vertical motion response spectrum recorded during the Northridge Earthquake, concluded that spectrum vertical to horizontal response ratio depends on the intensity, time, and site distance from the seismic source. They also found that the ratio of vertical acceleration to horizontal acceleration (that is now taken into account in seismic codes) is minor for structures with short natural period and is conservative for structures with long period (Bozorgnia and Campbell 2004).

Most of the analytical studies on seismic evaluation of urban structures are done based on fixed-base under the horizontal seismic force to examine the effect of a vertical earthquake of the structural response considering a percent of dead and live loads. Few studies have assessed the site response effect on the vertical component of earthquakes in a three-dimensional platform. This study aims to examine the vertical acceleration imposed on the urban structures under a horizontal earthquake considering soil-structure interaction using urbanely constructed complex geometry. To this end, time history comparative analysis of 3D structures was done within two models of fixed-base and soil-structure interaction (SSI).

## 2 The Studied Model

In the current research, the studied model was analyzed based on a real model of a 13-story structure in which 4 stories are located under the ground. This building is located in Iran, Mashhad city. The structural system of this model consisted of a steel joint frame and a concrete shear wall constructed to tolerate the seismic forces. Figure 1 depicts the placement of shear walls and columns in the plan. The European IPE standard and box sections were used for beams and columns, respectively in constructing the steel



joint frame. Rayleigh's damping method was used for structure damping based on the 5% value (Council 1997). ETABS software was employed to model the plant using fixed-base (Fig. 2).

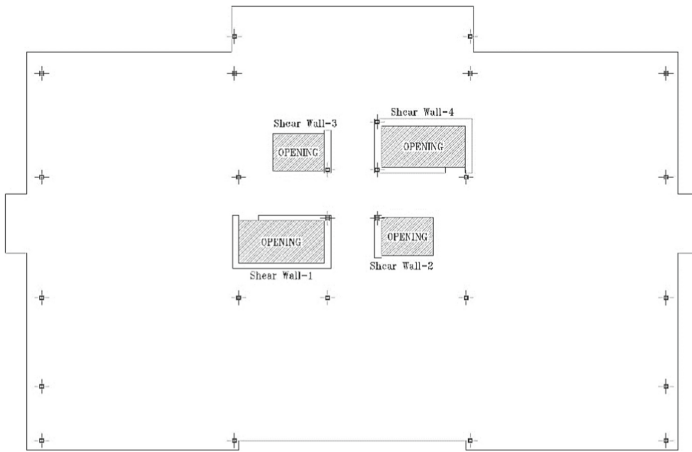


**Fig. 1.** Placement plan of shear walls and columns

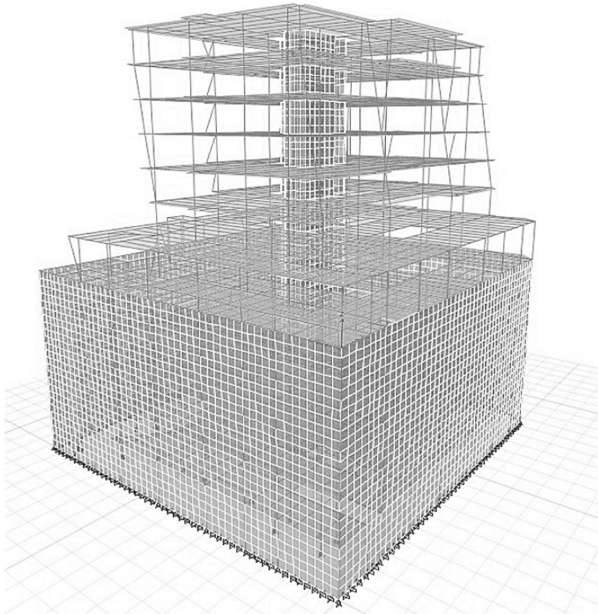


**Fig. 2.** Structure model with fixed-base through ETABS software

## 2.1 Geotechnical Parameters of Site Soil

Using the geotechnical studies, to determine the engineering parameters of soil, field and laboratory examinations were used to complete the computations. Regarding the relationship between the geotechnical parameters and the Corrected SPT-N Value, the researchers have presented the experimental relations between soil friction angle and density of the soil, as presented in Table 1.

**Table 1.** Corrected SPT-N Value in site

Soil classification (USCS)	$N_{(SPT)}$	(Sabatini et al. 2002) relative density
SC	40	Dense
Soil classification (USCS)	$N_{(SPT)}$	(Sabatini et al. 2002) rigidity
CL	42	Rigid

After an analysis of all the results of experimental and field tests based on the mentioned geotechnical project, the properties of the modelled soil are presented in Table 2.

**Table 2.** Properties of soil layers in the model

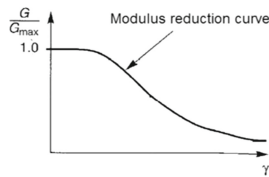
Soil classification (USCS)	Depth range (m)	Soil mass density ( $\text{kg/m}^3$ )	Poisson's ratio	Friction angle	Cohesion (kPa)
SC	0–46	1986	0.25	30.93	7.3
CL	46–60	2040	0.3	29	19.6

As the Elasticity modulus depends on stress (Brinkgreve et al. 2012) and the excavation method is Top-Down type, the unloading modulus of elasticity was used for static analysis and the relevant values are reported in Table 3. Moreover, the maximum shear modulus was calculated based on the Eq. (1) (Kramer 1996) to determine the dynamic shear modulus of soil for seismic analysis of soil-structure interaction considering geophysical experiments. The shear modulus ratio ( $G/G_{\max}$ ) in this research was 0.4 (Yeganeh et al. 2015) to use for the reduction of the stiffness of the soil (Fig. 3) and the obtained results reported in Table 3. Furthermore, the Mohr-Coulomp Plasticity constitutive model was used to model soil behavior. The damping rate of soil was determined based on the ASCE 7-16 and ASCE-SEI 41-17 codes in which, this rate is equal to 3.3% (ASCE 2016; Engineers 2017).

$$G_{\max} = \rho v_s^2 \quad (1)$$

**Table 3.** Stiffness properties of soil

Thickness (m)	$E_{ur}$ static (MPa)	E dynamic (MPa)
5.4	74.34	412.04
5.4	105.41	508.08
5.4	128.77	614.18
5.4	170.27	690.51
5.8	191.78	792.52
8.6	243.05	947.04
10	295.74	1111.52
14	147.96	1193.4

**Fig. 3.** Modulus of reduction curve (Kramer 1996)

## 2.2 Modeling SSI

To model SSI 3D Model, the direct method was used through the finite element software, Abaqus. Relevant dimensions should be selected properly for soil modeling in order to consider structure and soil vibration effects directly in the equations. Many references suggest considering the numerical model's dimensions 3–5 times greater than the structure dimensions with a soil depth of 30m. According to the mentioned points, the model in 250m in dimensions and 60m in height (Fig. 4) (Far et al. 2010; Briaud and Lim 1997).

Considering the fact that in the event of an earthquake, there is common surface and thus slips between the soil, the retaining walls and the foundation, the researchers used the option of Interactional Contact (surface to surface) in Abaqus software so as to model the fictional contact surface of the mentioned item (Khazaei and Amiri 2017; ABAQUS 2014).

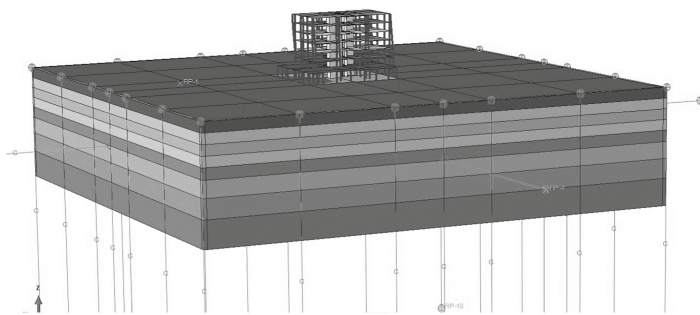


**Fig. 4.** Structure model considering SSI in Abaqus Software

### 2.3 Determining Seismic Acceleration Records to the Base of the Numerical Model

According to seismic microzonation studies in Mashhad, Iran, three acceleration records were proposed based on Table 4 with a 500-year return period for the Design Basis Level that its occurrence probability or earthquakes with a higher magnitude are less than 10% within 50-year of the building lifetime (Moghaddas 2009).

**Table 4.** Selected acceleration records and properties

Earthquake	Date of the occurrence	Station	Magnitude (M)	PHA longitudinal (g)	PHA transverse (g)
Kojur–Firoozabad (poul), Iran	May, 28, 2004	Poul	6.4	0.27	0.28
Karehbass, Iran	May, 6, 1999	Deh-Bala	6.3	0.275	0.278
Athens, Greece	Sep, 7, 1999	Sepolia	5.9	0.224	0.253

## 3 Analysis Results

Imposing the earthquake record to base of the structure with assumed it’s placed on bedrock is a method that is usually used to evaluate the structural response and behavior. Although soil rigidity does not lead to a significant alteration in the behavior of structures constructed on the bedrock, an increase in soil flexibility leads to irreversible changes in SSI and structural behavior. The results of vertical acceleration caused by horizontal seismic loads have been presented after conducting time history analysis for models with fixed-base and SSI under the records introduced in Sect. 2 (Fig. 5).

According to the results, considering SSI in dynamic analyses has a considerable effect on increased vertical acceleration in structure leading to a 2–3 times increase in vertical acceleration. However, non-considering this variable may be non-conservative.



floors and structural system of concrete shear wall on the vertical acceleration, using 3-D complex geometry model. The obtained results imply that considering SSI leads to an increase in vertical acceleration of all stories. Therefore, this subject should be considered in further studies on the SSI effect on the buildings, in particular in the field of vertical earthquakes.

## References

- Venanzi, I., Salciarini, D., Tamagnini, C.: The effect of soil–foundation–structure interaction on the wind-induced response of tall buildings. *Eng. Struct.* **79**, 117–130 (2014)
- Ucak, A., Tsopelas, P.: Effect of soil–structure interaction on seismic isolated bridges. *J. Struct. Eng.* **134**(7), 1154–1164 (2008)
- Stewart, J.P., Seed, R.B., Fenves, G.L.: Empirical evaluation of inertial soil-structure interaction effects. Pacific Earthquake Engineering Research Center (1998)
- Papazoglou, A., Elnashai, A.: Analytical and field evidence of the damaging effect of vertical earthquake ground motion. *Earthq. Eng. Struct. Dynam.* **25**(10), 1109–1137 (1996)
- Bozorgnia, Y., Niazi, M.: Distance scaling of vertical and horizontal response spectra of the Loma Prieta earthquake. *Earthq. Eng. Struct. Dynam.* **22**(8), 695–707 (1993)
- Bozorgnia, Y., Campbell, K.W.: The vertical-to-horizontal response spectral ratio and tentative procedures for developing simplified V/H and vertical design spectra. *J. Earthq. Eng.* **8**(02), 175–207 (2004)
- Council, B.S.S.: NEHRP recommended provisions for seismic regulations for new buildings and other structures. FEMA **302**, 303 (1997)
- Sabatini, P., Bachus, R.C., Mayne, P.W., Schneider, J.A., Zettler, T.: Geotechnical Engineering Circular No. 5 Evaluation of Soil and Rock Properties, United States. Federal Highway Administration. Office of Bridge Technology (2002)
- Brinkgreve, R., Engin, E., Swolfs, W.: PLAXIS 3D material models manual. Plaxis bv (2012)
- Kramer, S.L.: Geotechnical Earthquake Engineering. Prentice Hall, New York (1996)
- Yeganeh, N., Bazaz, J.B., Akhtarpour, A.: Seismic analysis of the soil–structure interaction for a high rise building adjacent to deep excavation. *Soil Dyn. Earthq. Eng.* **79**, 149–170 (2015)
- ASCE: Minimum design loads and associated criteria for buildings and other structures. ASCE standard ASCE/SEI 7–16 (in preparation). American Society of Civil Engineers, Reston, VA (2016)
- A. S. o. C. Engineers: Seismic Evaluation and Retrofit of Existing Buildings: ASCE/SEI, 41-17
- Tabatabaiefar, H.R., Samali, B., Fatahi, B.: Effects of dynamic soil-structure interaction on inelastic behaviour of mid-rise moment resisting buildings on soft soils. In: Australian Earthquake Engineering Society Conference (2010)
- Briaud, J.-L., Lim, Y.: Soil-nailed wall under piled bridge abutment: simulation and guidelines. *J. Geotech. Geoenviron. Eng.* **123**(11), 1043–1050 (1997)
- Khazaei, J., Amiri, A.: Evaluation of the dynamic responses of high-rise buildings with respect to the direct methods for soil-foundation-structure interaction effects and comparison with the approximate methods. *J. Struct. Constr. Eng.* **4**(2), 106–122 (2017)
- V. ABAQUS: 6.14 Documentation. Dassault Systemes Simulia Corporation (2014)
- Hafezy Moghaddas, N.: Seismic microzonation of Mashhad city. geological survey of Iran north east territory, Mashhad (2009). (in Persian).
- Far, H., Samali, B., Fatahi, B.: Effects of dynamic soil-structure interaction on inelastic behaviour of mid-rise moment resisting buildings on soft soils. In: Australian Earthquake Engineering Society Conference. Australian Earthquake Engineering Society (2010)



# Tip Post-grouting Using Smart Cells at Urubó Bridge - Premobilization and Improvement of End Resistance

Antonio Marinucci<sup>1</sup>, Mario Terceros Arce<sup>2</sup>(✉), and Mario A. Terceros Herrera<sup>2</sup>(✉)

<sup>1</sup> V2C Strategists, LLC, New York, NY, USA  
amarinucci@v2cstrategists.com

<sup>2</sup> Incotec S.A., Santa Cruz de la Sierra, Bolivia  
{mta, math}@incotec.cc

**Abstract.** This paper describes the results of the tip post-grouting that was performed to improve the nominal axial resistance of 34 bored piles for the Urubó Bridge project crossing the Piraí River in Santa Cruz, Bolivia. A Smart Cell is a closed-type tip post-grouting device that is attached to the bottom of the steel reinforcement cage of a bored pile to premobilize end resistance and reduce uncertainty. Control of the grout is maintained within the device during injection and a uniform stress is imparted across entire base area simultaneously, inducing a pre-mobilization load into the pile as well as the soil. The induced load is computed directly from the grout pressure and known geometry of the device. During the grouting process, there were noticeable differences in the grouting pressures achieved and responses observed, even within short distances between the piles, which were likely caused by the highly variable soil conditions, composition, alterations during construction and engineering characteristics. This paper will provide an overview and principles of the tip post-grouting system, the design methodology, and select grouting and static load testing results.

**Keywords:** Tip post-grouting · Design · Performance · Risk · Uncertainty

## 1 Introduction

As an axial compressive load is applied to the top of a bored pile, the pile moves downward relative to the in-situ soil, where the axial resistance afforded by the soil is first mobilized in side resistance and then in end resistance. Successful installation and performance of a bored pile are affected by various factors, including workmanship, base cleanliness, borehole integrity, and concrete placement. An optimized maximum resistance cannot be realized by conventional (i.e., ungrouted) bored piles because the full side resistance is achieved at very small vertical displacements, while the full tip resistance is achieved at relatively large vertical displacements (Fig. 1).

The side resistance of a bored pile will mobilize its peak strength after a normalized displacement (i.e., vertical displacement divided by the diameter of the bored pile:  $D_{vm} = \delta_v/D_p$ ) of about 0.2% to 0.4% (point B, Fig. 1), regardless of soil type. At this vertical

displacement, the end resistance that has mobilized is relatively small. Conversely, the end resistance does not fully mobilize until  $D_{vn}$  of about 4% to 5% in both soil types (point D, Fig. 1). However, the axial resistance continues to increase with continued displacement in cohesionless soils, and a practical limit for  $D_{vn}$  of 10% is commonly used. Chen and Kulhawy (2002) reported on the mobilization of axial resistance in competent soils for different normalized displacements, and a summary is provided in Table 1.

**Table 1.** Mobilization of axial resistance of a conventional (ungROUTED) bored pile in axial compression loading (after Chen and Kulhawy 2002)

Normalized displacement	Mobilized resistance in cohesionless soils			Mobilized resistance in cohesive soils		
	Total axial	Side	End	Total axial	Side	End
		(% of total axial)			(% of total axial)	
0.4%	50%	90%	10%	50%	90%	10%
4%	100%	76%	24%	100%	76%	24%
10%	159%	76%	83%	–	–	–

Due to this strain incompatibility in mobilizing axial resistance, utilizing the full side and end resistance in design is not realistic and designers have typically neglected one component or reduced the relative contributions of side and/or end resistance. Other issues may develop during installation, even with high quality craftsmanship, including the accumulation of sediment (i.e., soft bottom condition) and the change in the state of stress (i.e., stress relief) at the bottom of the shaft. Downward vertical displacement of the pile is required to mobilize the axial resistance; therefore, with greater amounts of sediment on the bottom and/or stress relief of the soils, a greater amount of displacement would be required to mobilize the axial resistance. For example, a high quality, well-constructed bored pile with a diameter of 1500 mm would require about 60 mm of vertical displacement to mobilize the 100% of the possible geotechnical axial end or tip resistance. If there was excess sediment on the bottom of the pile or if the soil at the bottom of the hole were to relax upon excavation, an additional amount of displacement would likely be required to fully mobilize the tip resistance.

Tip post-grouting beneath the base of a bored pile is used to pre-mobilize the axial end resistance of the pile, to better align the load transfer curves (Fig. 1), to increase the pile’s (usable) axial resistance, and to improve the axial load-displacement performance (at intermediate loads) of the pile as well as to mitigate against a soft bottom condition and stress relief due to installation. Benefits of tip post-grouting with a Smart Cell include stiffening the load-deformation response under working loads, reducing settlement of the pile under applied loading, shortened constructed length of the shaft, ability to be performed in a range of ground conditions, utilizing usable tip resistance in design computations, verifying a lower bound of axial resistance, and improving the ground beneath the base of the shaft.



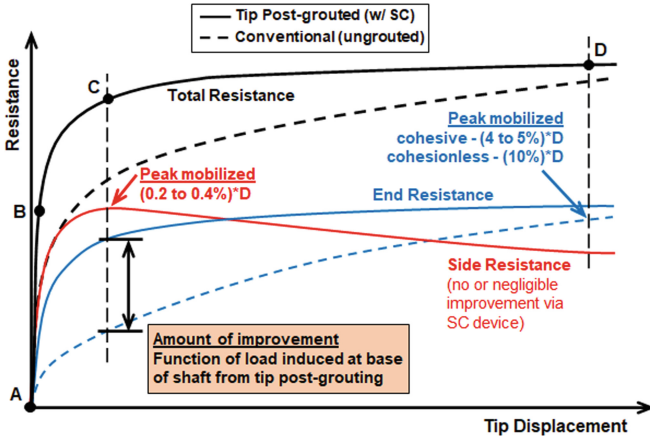


**Fig. 1.** Generalized load transfer behavior of conventional (ungROUTED) and tip post-grouted bored piles (mod. after Brown et al. 2018 and Marinucci et al. 2021)

## 2 Basic Principles

Tip post-grouting is a technique used to inject a neat cement grout, under pressure, beneath the base of a bored pile to improve the post-construction performance of a bored pile when subjected to axial compressive loads, and can be performed using an open- or closed-type grout distribution device. A Smart Cell (SC) is a closed-type tip post-grouting device that is attached to the bottom of the steel reinforcement cage of bored piles. The device itself comprises top and bottom steel plates, cell walls, and internal connections and attachments. The cell is a relatively rigid system where the internal and outside dimensions of the device are known (Fig. 2), which allows the straightforward computation of the amount of bi-directional force or load induced during the grouting (Eq. 1):

$$P_{SC} = p \cdot A_{SC} \tag{1}$$

where:  $P_{SC}$  is the induced force or load,  $p$  is the injection pressure of the grout (measured a short distance above the top of the pile), and  $A_{SC}$  is the cross-sectional area of the device.

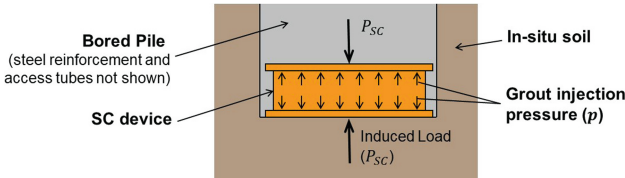


**Fig. 2.** Graphical depiction of grouting and induced load (mod. from Marinucci et al. 2021)

After the borehole is drilled, the steel reinforcement cage along with the embedded attachments (e.g., instrumentation and SC device) is placed into the borehole, which is then filled with concrete (Fig. 3a and point A in Fig. 1). After the concrete has achieved the minimum required unconfined compressive strength ( $f'_c$ ), the tip post-grouting operation can be performed. Control of the grout is maintained within the expanding device. As the grout is injected under pressure into the device, the cell expands and pushes upward against the pile and downward against the in-situ soil below. The injection of pressurized grout induces a bi-directional load ( $P_{SC}$ ) within the device, which simultaneously mobilizes negative side resistance to resist the upward loading and positive tip resistance to resist the downward loading (Fig. 3b, 3c and 3d, which delineated as points B to D in Fig. 1, respectively). Due to the rigidity of the device, the injection pressure ( $p$ ) imparts a uniform stress across the entire base area simultaneously.

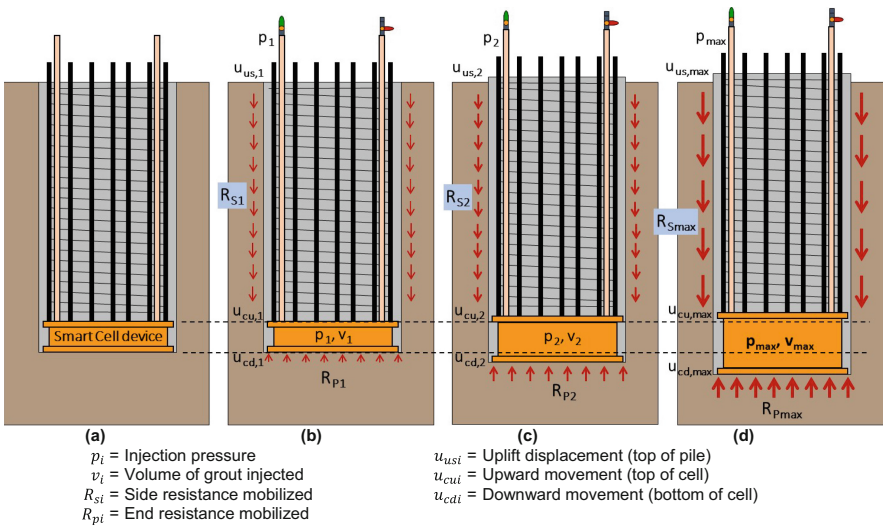


**Fig. 3.** Generalized sequence: (a) installation into borehole and concrete placement, (b) commencement of grouting, (c) intermediate grouting stages, and (d) grouting completed (after Marinucci et al. 2021)

Grouting is performed using a controlled process to ensure proper implementation and performance. The injection pressure, volume and flow rate of grout, and movements at the top of the shaft and at the SC device are measured throughout the grouting operation. The grouting termination criteria for tip post-grouting includes target grout pressure, (net) grout volume, maximum uplift displacement of the pile, and expansion limit of the SC device. The upward displacement measured at the top of the bored pile is limited to between 6 and 19 mm (defined by the project requirements) to mitigate against potentially negative effects to side resistance due to reversal of side resistance (i.e., acting downward against uplift during grouting, then acting upward against axial compression loading).

The relationship between the induced load ( $P_{SC}$ ) and the measured vertical displacement (Fig. 4) provides valuable insight into the behavior during grouting (e.g., estimate amount of loose sediment) and for estimating the stiffness (or modulus) and unit end resistance of the soil at the completion of grouting (Marinucci et al. 2021). The injection pressure or induced load required to initiate the expansion of the cell is the lesser of the reaction from the sum of the pile’s self-weight plus the axial side resistance above the cell or the axial end resistance below the cell.

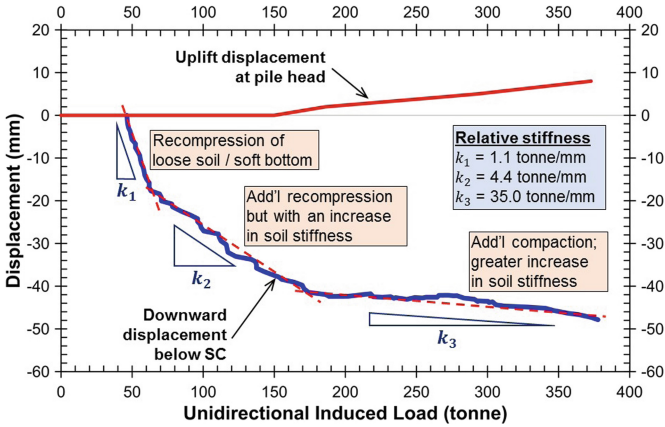


Fig. 4. Representative example of induced load vs. vertical displacement during grouting (mod. after Marinucci et al. 2021).

Graphing the relationship of injection pressure vs. grout volume provides a qualitative indication of local soil type present at the base of the bored pile. Based on experience with performing multiple tip post-grouting operations in various soil conditions, the shape and trend of the pressure vs. volume curve provides evidence whether the soil type is cohesionless or cohesive (Marinucci et al. 2020). If the trend indicated a relatively low maximum grouting pressure that had achieved a maximum value or flattened, this would suggest tip post-grouting in cohesive soils, where the end resistance had fully mobilized. However, if the trend indicated a continued increase in injection pressure with continued grouting, this would be indicative of tip post-grouting in granular soils, where the end resistance may not have fully mobilized. The trend of the pressure-volume curve would be similar to the general trends of the response curves presented in Fig. 5.

### 3 Design Methodology – Target Pressure

For tip post-grouting in Bolivia with a SC device, the load-displacement curves developed by Chen and Kulhawy (2002) and as presented in Brown et al (2018) form the basis to compute the target (or minimum) injection pressure ( $p_t$ ) based on the tolerable post-construction displacement of the bored pile. The key to designing an effective tip post-grouting system is the target injection pressure ( $p_t$ ), which can be estimated but is not guaranteed, as  $p_t$  is dependent upon many different factors, including soil type, in-situ

soil conditions, and available reaction force (i.e., self-weight of the bored pile plus side resistance).

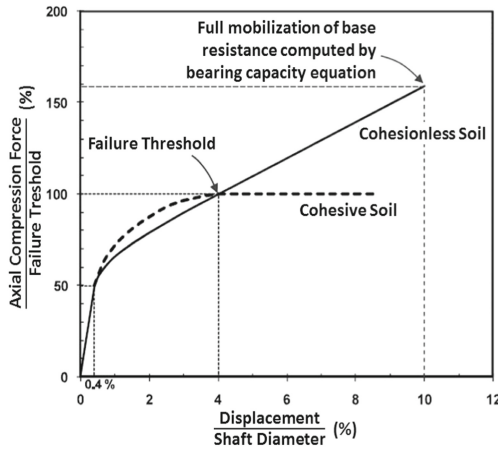


**Fig. 5.** Normalized load-displacement curves of bored piles in axial compression in cohesive and cohesionless soils (mod. after Brown et al. 2018)

The guidance presented in AASHTO §10.8.3.5 (2012) is used to estimate  $p_t$ , which is described below using an example. The nominal axial compression resistance of a single drilled shaft ( $R_n$ ) is estimated using Eq. (2). As shown on Fig. 5, 100% of the failure threshold typically occurs at normalized displacement ( $\Delta D_{vn}$ ) of about 4% for both cohesionless and cohesive soils. The vertical axis (Fig. 5) represents the ratio of axial compression load to failure threshold (i.e., nominal axial compression resistance,  $R_n$ , or amount of resistance that has been mobilized at a given vertical displacement). The side resistance is fully mobilized at  $\Delta D_{vn}$  of about 0.2% to 0.4%, whereas the end resistance is fully mobilized at  $\Delta D_{vn}$  of about 4% to 5% for cohesive soils and about 10% for cohesionless soils (Table 1 and Fig. 5).

$$R_n = R_S + R_P = \sum_{i=1}^n (q_{si}A_{si}) + q_pA_p \quad (2)$$

where:  $R_n$  = nominal axial compression resistance of a single drilled shaft

$R_S$  = nominal side resistance of a single drilled shaft

$R_P$  = nominal end resistance of a single drilled shaft

$q_{si}$  = nominal unit side resistance for soil layer  $i$

$A_{si}$  = nominal surface area of the soil-shaft interface for soil layer  $i$

$n$  = number of soil layers

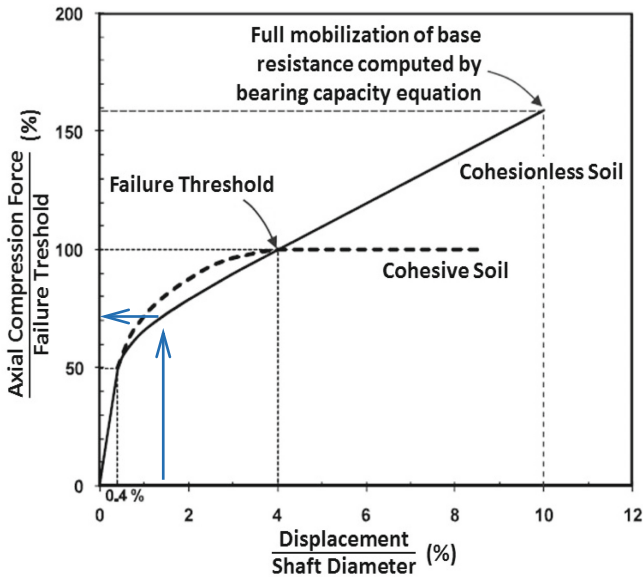
$q_p$  = nominal unit end resistance

$A_p$  = nominal cross-sectional area of the tip of the drilled shaft

Example:

- Known information – pile tipped into sandy soil within heterogeneous deposit
  - Drilled shaft diameter ( $D_p$ ) = 1.8 m = 1800 mm
  - Embedment length ( $L_p$ ) = 40 m
  - Unfactored design load ( $P_{d, serv}$ ) = 5600 kN
  - Maximum allowable post-construction vertical displacement ( $\delta_{v, allow}$ ) = 25 mm
- Computed design parameters
  - Nominal side resistance ( $R_S$ ) = 2625 kN
  - Nominal end resistance ( $R_P$ ) = 3600 kN
  - Nominal axial compression resistance ( $R_n$ ) = 6225 kN
  - Self-weight of the shaft ( $W_p$ ) = 780 kN
  - Normalized displacement ( $\Delta D_{vn}$ ) = 25 mm/1800 mm = 1.4%
- Determine the mobilized axial compressive force ( $R_M$ ):
  - From Fig. 5 for a cohesionless soil:

$$\frac{\text{Displacement}}{\text{Pile Diameter}} = \Delta D_{vn} = 1.4\%$$



$$\frac{\text{Axial Compression Force}}{\text{Failure Threshold}} \approx 71\%$$

$$- R_M = 71\% R_n = 0.71 * 6225 \text{ kN} = 4420 \text{ kN}$$

- Determine the service resistance force ( $R_{Service}$ ):

$$- R_{Service} = R_M - W_p = 4420 \text{ kN} - 780 \text{ kN} = 3640 \text{ kN}$$

- Determine the target injection pressure ( $p_t$ ):

$$- \text{Internal bearing area of the cell } (A_{SC}) = 1.95 \text{ sq m}$$

$$- p_t = (P_{d, serv} - R_{Service})/A_{SC} = (5600 \text{ Kn} - 3640 \text{ kN})/1.95 \text{ sq m} = 1005 \text{ kPa} = 10.1 \text{ bar}$$

## 4 Case History – Urubó Bridge Project

The new Urubó Bridge will be constructed adjacent to the existing bridge, which connects the municipalities of Porongo (west) and Santa Cruz de la Sierra (east) in Bolivia. The new bridge will be about 12 m (40 ft) wide and about 420 m (1,380 ft) in length. The 5-span bridge (Fig. 6) will be supported by four pier structures, located about 100 m (330 ft) apart and each with seven drilled shafts (arranged in two rows), located in the Pirafí River and two abutments supported by 3 drilled shafts each (arranged in one row), which are located beyond the extents of the river's edges. Based on the project drawings, each of the bored piles is 1200 mm in diameter with an embedment depth of about 25 m at the abutments and about 30 m for each of the piers.

### 4.1 Subsurface Conditions

As shown in Fig. 6, one soil boring was performed at each of the four pier locations to a depth of about 40 m along with Standard Penetration Testing (SPT). At the time the soil borings were performed, the elevation of the ground surface at the borings was approximately El. +399.4 m, and the ground water was located just below the ground surface. The soil deposit is classified as quaternary sedimentary silty-clayey sands of alluvial and flood plain origin. In general, the subsurface consists of highly variable soil deposits, bedding, composition, and characteristics, which are the results of a dynamic river environment. The general subsurface profile (Fig. 7) contains an upper layer of granular fill underlain by highly heterogeneous and interbedded layers consisting of clay, silt, and sand. For the west and east abutments, the bored piles were tipped into silty sands and lean clay with silt, respectively. The bored piles for the piers were tipped into lean clay soils: lean clay with sand for piers 1 and 2 and lean clay with silt for piers 3 and 4.

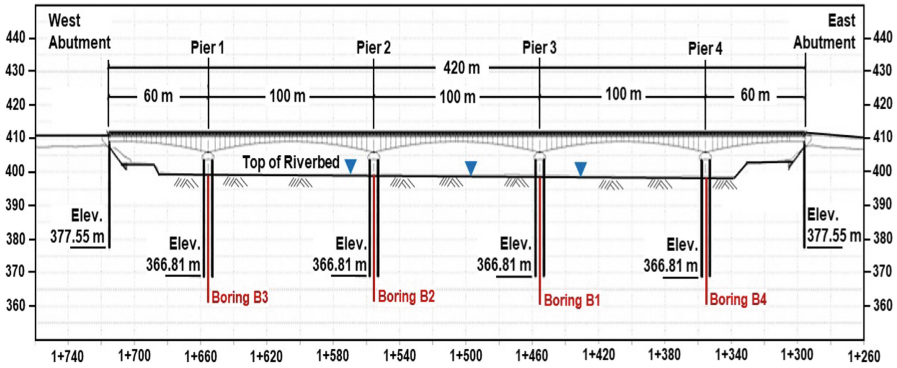


Fig. 6. Elevation profile of the bridge super- and substructure and approximate boring locations

## 4.2 Pile Installation and Tip Post-grouting

The bored piles were constructed using temporary segmental casing with the use of a drilling support fluid (water) to prevent instability at the bottom of the borehole. A SC device and attachments were incorporated into the bottom of the steel reinforcement cages and lowered into the borehole, after which the concrete was placed using the tremie method. After the concrete achieved the required minimum unconfined compressive strength and when the water level within the river permitted work to proceed, the tip post-grouting was performed individually for each bored pile.

The target pressure for the tip post-grouting was computed for its worst-case condition. The upper 1.5 m of side resistance was neglected for the computations. For the pier structures, the unfactored axial compression design load per pile ( $P_{d, serv}$ ) was 400 tonne (3925 kN) with a maximum allowable post-construction vertical settlement ( $\delta_{v, allow}$ ) of 30 mm, resulting in a normalized post-construction displacement ( $\Delta D_{vm}$ ) of 2.5. For the worst-case scenario, the minimum required target pressure was estimated to be about 10.3 bar (1025 kPa). Monitoring and recording of the injection pressure, grout volume injected, and grout flow rate were performed in real time using transducers connected to a data acquisition system and observed on a laptop computer. The uplift and downward movements of the bored pile and the SC were measured using manual readings obtained via visual survey and telltale extensometers, respectively.

The target pressure for the tip post-grouting was computed for its worst-case condition. The upper 1.5 m of side resistance was neglected for the computations. For the pier structures, the unfactored axial compression design load per pile ( $P_{d, serv}$ ) was 400 tonne (3925 kN) with a maximum allowable post-construction vertical settlement ( $\delta_{v, allow}$ ) of 30 mm, resulting in a normalized post-construction displacement ( $\Delta D_{vm}$ ) of 2.5. For the worst-case scenario, the minimum required target pressure was estimated to be about 10.3 bar (1025 kPa). Monitoring and recording of the injection pressure, grout volume injected, and grout flow rate were performed in real time using transducers connected to a data acquisition system and observed on a laptop computer. The uplift and downward movements of the bored pile and the SC were measured using manual readings obtained via visual survey and telltale extensometers, respectively.

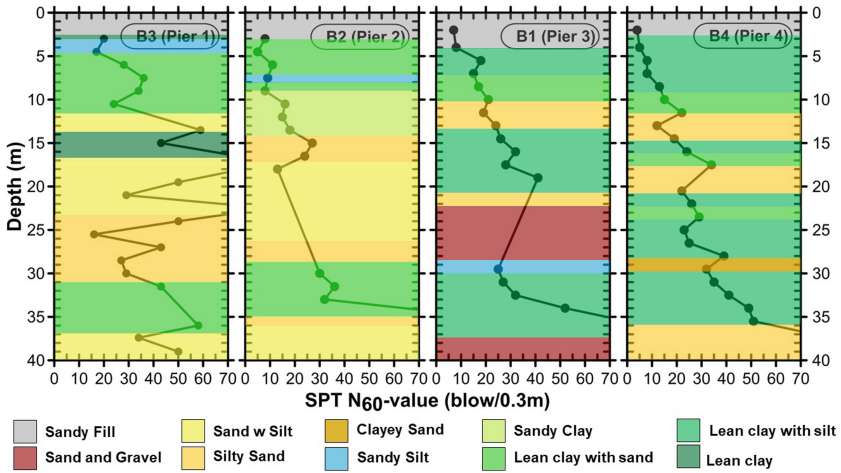


Fig. 7. Subsurface profile and SPT  $N_{60}$ -values at each soil boring

### 4.3 Results from Injection of Production Piles

A summary of the results of the tip post-grouting performed at the abutments and the pier structures is provided in Table 2. As listed, there was considerable variability in the injection pressures achieved and with the observed behavior, even within short distances from each other. The achieved pressures, on average, were notably higher for the piles at the pier structures than for those at the abutments, possibly due to the additional side resistance available for the deeper shafts and due to the increased relative strength at the greater depths. In addition, some of the differences can be attributed to the different soil type present at the base of piles – ranging from silty sand to lean clay.

At the abutments, the unidirectional induced loads ranged from 1538 to 4534 kN, which were about 39% to 116% of the unfactored design load ( $P_{d, serv}$ ). The induced load resulted in a normalized downward displacement ranging from about 1.4% to 4.0%, which corresponds to an average mobilized total axial resistance of about 75% to 100%. For the piles at the pier structures, the unidirectional induced loads ranged from 2239 to 4526 kN, which were about 57% to 115% of the unfactored design load ( $P_{d, serv}$ ). The induced load resulted in a normalized downward displacement ranging from about 0.3% to 4.9%, which corresponds to an average mobilized total axial resistance of about 40% to 109%. As a result of the tip post-grouting and resulting displacement via preloading, increased stiffness of the soil beneath the base of each pile and smaller post-construction vertical displacements would be anticipated.

The maximum achieved injection pressures reported in literature and by firms performing tip post-grouting (not limited to a particular country or region) has been about 150 bar in sands and about 80 bar in clays/silts (Loehr et al. 2017). The injection pressures achieved at the west abutment (in silty sand) were on the low range of what has been reported in the literature and is even on the low expected range based on experience in the Santa Cruz region. The injection pressures achieved at the pier structures and east abutment (lean clay with sand or silt) were in the middle to higher end of what has been



**Table 2.** Results of tip post-grouting performed at the Urubó Bridge

Location	Desc.	Max. pressure achieved	Max. downward displacement		$\frac{P_{max}}{P_t}$	Unidirectional induced load	$\frac{P_{SC}}{P_{d, serv}}$
		(bar)	(mm)	(Norm.)		(kN)	
West abutment	Range	22.0–59.2	65.0–98.2	5.4%–8.2%	214%–575%	1977–4534	50%–116%
	Average	40.6	81.6	6.8%	394%	3255	83%
	Std Dev	26.3	23.5	2.0%	256%	1808	46%
Pier 1	Range	29.3–57.3	8.0–58.2	0.9%–3.0%	284%–556%	2383–4478	61%–114%
	Average	48.6	24.2	2.1%	472%	3814	97%
	Std Dev	9.9	18.1	1.5%	96%	737	19%
Pier 2	Range	35.1–58.0	9.0–26.4	1.3%–2.2%	341%–563%	2907–4526	74%–115%
	Average	46.5	15.9	1.8%	451%	3674	94%
	Std Dev	7.9	5.9	0.5%	77%	570	15%
Pier 3	Range	31.7–52.3	3.0–40.9	0.2%–2.1%	308%–508%	2552–4123	65%–105%
	Average	42.6	17.0	1.0%	414%	3390	86%
	Std Dev	6.0	12.6	1.1%	58.4%	463	12%
Pier 4	Range	27.3–44.8	16.3–32.0	1.4%–2.3%	265%–435%	2239–3595	57%–92%
	Average	34.8	22.8	1.8%	338%	2834	72%
	Std Dev	6.8	5.9	0.5%	66%	501	13%
East abutment	Range	16.8–34.8	17.3–34.0	1.4%–2.8%	163%–338%	1538–2774	39%–71%
	Average	27.2	24.8	2.1%	264%	2247	57%
	Std Dev	9.3	8.5	0.7%	91%	638	16%

reported and is in line with what has been achieved on past projects in this soil type in the Santa Cruz region.

The (computed) induced load-displacement relationships from the tip post-grouting performed at piles 2, 3, 5, and 6 at Pier 3 (tipped in lean clay with silt) and Pier 4 (tipped in lean clay with silt) are shown in Fig. 8. As shown in Eq. (1), the induced load is correlated to the injection pressure:  $P_{SC} = p \cdot A_{SC}$ , and the downward displacement is measured using telltale extensometers (and can be deduced using the grout volume and the internal dimensions of the cell). The differences in the grouting pressures that were achieved varied appreciably over short distances across each pier (Table 2). In addition, the measured downward displacements varied considerably when compared with the neighboring pier as well as at each pier though the displacements were more similar at Pier 4 than at Pier 3, as did the trend or the development of the load-displacement relationships.

The differences in the load-displacement behavior reflect the local differences present at the base of the pile and within the soil below. A stiffer soil response would be reflected by a gradual slope in the curve, whereas the curve for a softer soil would be represented by a steep slope. As each of the responses does not reflect a constant slope (i.e., instances of gradual and steep slopes at each pile), the tip post-grouting is influenced not only by

the soil conditions immediately below the base of the pile but also by the soil within the influence zone of the loading. In addition, the influence zone may be changing during the grouting process as a compacted soil plug is being formed, which is then facilitating the distribution of the injection pressure into the soil.

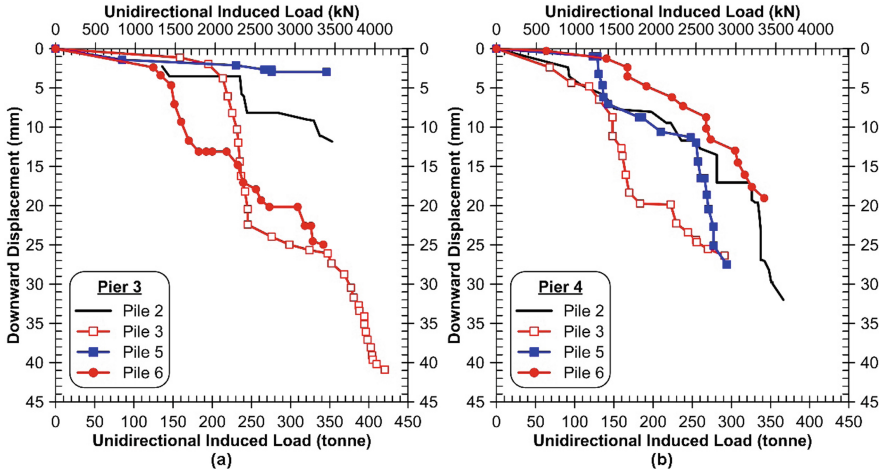


**Fig. 8.** Select results of induced load vs. displacement from tip post-grouting (a) at Pier 3 and (b) at Pier 4

## 5 Conclusions

During grouting, loose soil or debris (i.e., soft bottom condition) is first compacted, and then, as the injection pressure increases, the in-situ soil is compressed, resulting in a pre-mobilization of the end resistance. Select results from the tip post-grouting performed on 34 bored piles for a bridge project in Santa Cruz de la Sierra, Bolivia are presented. There was considerable variability in the injection pressures achieved and trends observed in the measured pressure-volume and inferred induced load-displacement responses, even within short distances at the same support structure. Overall, the unidirectional induced load ranged from 1538 to 4534 kN, which equated to about 39% to 116% of the design service load. Although the difference in the responses of a pile under load is typically attributed to the effects of the construction technique and process employed, many of the differences at the Urubó Bridge project can be explained by the depositional environment and highly variable soil characteristics. The key benefit of using this tip post-grouting technique at each bored pile was the reduction of risk and uncertainty of performance due to the highly variable soil conditions. As a result of the tip post-grouting and resulting displacement via preloading, increased stiffness of the soil beneath the base of each pile and smaller post-construction vertical displacements would be anticipated.

## References

- AASHTO: AASHTO LRFD Bridge Design Specifications, 6th edn. American Association of State Highway and Transportation Officials. Washington, D.C., 1661 p. (2012)
- Brown, D.A., Turner, J.P., Castelli, R.J., Loehr, J.E.: Drilled Shafts: Construction Procedures and Design Methods. Geotechnical Engineering Circular No. 10. Report No. FHWA-NHI-18-024. Federal Highway Administration, March, 758 p. (2018)
- Chen, Y.-J., Kulhawy, F.H.: Evaluation of Drained Axial Capacity for Drilled Shafts. Geotechnical Special Publication No. 116, Deep Foundations 2002, M.W. O'Neill and F.C. Townsend, eds., ASCE, Reston, VA, pp. 1200–1214 (2002)
- Loehr, J.E., et al.: Evaluation and Guidance Development for Post-Grouted Drilled Shafts for Highways, Report No. FHWA-HIF-17-024, Federal Highway Administration, March, 158 p. (2017)
- Marinucci, A., Nichols, S.C.: Optimized Drilled Shaft Design through Post-Grouting. ASCE/Geo-Institute GeoStrata Magazine. May/June (2016)
- Marinucci, A., Nichols, S.C., Large, M.E.B.: Ensuring performance of tip post-grouted bored piles (drilled shafts) through a comprehensive quality assurance program. In: Proceedings of the DFI 43rd Annual Conference on Deep Foundations (2018)
- Marinucci, A., Terceros Herrera, M., Terceros Arce, M.: Improvement of toe resistance of drilled shaft foundations in highly variable sedimentary soils using smart cells. In: DFI Annual Conference. National Harbor, MD (2020)
- Marinucci, A., Terceros Herrera, M., Terceros Arce, M.: Tip post-grouting and premobilization of resistance of drilled shafts using smart-cells at two bridge structures in Bolivia. In: International Foundations Congress and Equipment Exposition (IFCEE), Dallas, TX. In review (2021)
- Mullins, G.: Grouting effectiveness – construction QA/QC of post-grouted shafts. Presentation delivered at FHWA/Caltrans Workshop on Quality Assurance for Post-grouted Drilled Shafts. April 15–16. Oakland, CA (2015)



# Analysis on the Influence of Rainfall Characteristics on the Stability of Granite Residual Soil Slope

Cheng Chen<sup>1,2(✉)</sup>, Jian-fei Liu<sup>1</sup>, and Jun Gong<sup>2</sup>

<sup>1</sup> Hunan Engineering Technology Research Center for High-Speed Railway Operation Safety Assurance, Hunan Vocational College of Railway Technology, Zhuzhou 412006, Hunan, China  
chencheng401@sina.com

<sup>2</sup> College of Civil Engineering and Mechanics, Xiangtan University, Xiangtan 411105, Hunan, China

**Abstract.** Rainfall characteristics have important impacts on slope stability. Aimed to analyze the influence of rainfall on granite residual soil slope stability. The finite element method is used for the calculation of transient seepage in the unsaturated slope, while the method of limit equilibrium is used for computing its safety factor. The change of pore water pressure, slip surface and safety factor are investigated through numerical calculations with consideration of various intensity and duration of rainfall. The results show good agreement with the statistic results of the rainfall-caused landslide cases. The type, intensity, duration of rainfall have significant impact on slope stability. And it is found that sometimes the minimum safety factor may occur several hours or several days after the rainfall, instead of the time during the rainfall or when the rain just stops.

**Keywords:** Granite residual soil · Rainfall · Slope stability · Unsaturated shear strength

## 1 Introduction

In recent years, China has frequently encountered extreme weather such as heavy rainfall, and the result of landslide disaster has attracted more and more attention. Rainfall infiltration is an important inducer of slope instability. In the process of rainwater infiltration, the interaction between the change of soil water content and the soil particles is the focus and difficulty of current research in the field of geotechnical engineering, and the coupling analysis of its interaction has been widely valued. Therefore, the analysis of the slope stability under the influence of rainfall is a subject worthy of attention.

Granite residual soil has engineering characteristics such as anisotropy, inhomogeneity, and easy disintegration and softening after immersion in water. Previous studies have shown that any nonuniform deformation of the slope soil may cause crack propagation and affect the performance of the slope soil. In early studies, the mechanical

component that describe the stress-strain relationship was coupled with the saturation-suction relationship. However, many recent theoretical and experimental studies have demonstrated that the mechanical and hydraulic components should be fully coupled in order to scientifically describe the deformation behavior of unsaturated slope soils [1]. Existing research covers many aspects, such as the stability analysis of slopes under steady-state seepage conditions, and the distribution of matrix suction and stability during slopes during rainfall. Research methods include full-scale model test, scale model centrifuge test, numerical simulation, etc. In terms of experiments, Moriwaki et al. [2] and Lin Hongzhou et al. [3] realized the rainfall-type failure of the slope in the full-scale experiment. The experimental results are very close to the real situation; Zhang Jianmin et al. [4] conducted slopes with weak layers in the centrifuge experiment of long slopes, artificial rainfall was used to destroy the slopes, and the failure modes and laws of special slopes were discovered. In terms of numerical calculation, many researchers have done a lot of work. For example, Ng et al. [5] studied the influence of rainfall and rainfall duration on slope stability. Through calculation, it was found that when the total rainfall is constant, the duration of rainfall will be the safety factor at the end of the rainfall has a significant impact, and there is a critical duration. When the duration is equal to the critical value, the safety factor for soil slope stability is the smallest. Song Erxiang et al. [6] used the slope seepage finite element method and the strength reduction finite element method to load the equivalent nodal force of the seepage with the soils gravity, seismic force and other loads on the soil slope, and calculated the seepage separately. For numerical calculation of such problems, in addition to the above methods, the finite element method and simplified method can also be used to calculate the non-steady state seepage [7, 8].

Previous studies and calculations have covered many aspects of unsaturated soil slope stability analysis, and have also studied the changes in slope stability during rainfall [9]. However, the stability analysis of granite residual soil slopes is rare, especially the stability analysis of the whole rainfall process. In this paper, a typical granite residual soil slope is selected, and through finite element analysis, it is found that the initial pore water pressure distribution law, initial saturation and initial effective stress of the granite residual soil slope have a significant influence on the slope instability during the whole rainfall process.

## 2 Laboratory Test Results

### 2.1 Basic Physical Property Index of Soil

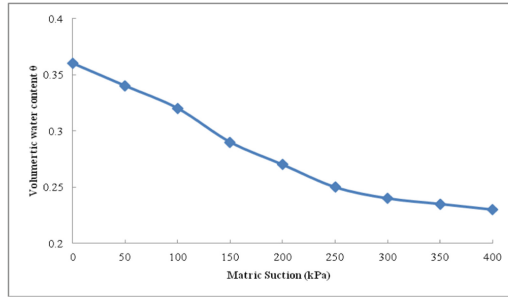
The sample soil was taken from the granite residual soil slope in a certain area of Xiangtan, Hunan. According to GB/T50123-1999 “Standard for Geotechnical Test Methods”, the basic physical property parameters of the sample soil were measured through laboratory tests, as shown in Table 1:

**Table 1.** Basic physical property index of sample soils

$\omega$ (%)	$\rho$ (g/cm <sup>3</sup> )	$\rho_d$ (g/cm <sup>3</sup> )	$S_r$ (%)	$G_s$	$e$
15.27	1.82	1.58	67.35	2.44	0.56
$W_P$ (%)	$W_L$ (%)	$I_L$	$I_P$	$\omega_{opt}$ (%)	$\rho_d \max$ (g/cm <sup>3</sup> )
25.95	50.03	-0.44	24.08	15.96	1.84

## 2.2 Soil-Water Characteristic Curve of Sample Soil

In this paper, a strain-controlled ZFY-1 direct shear instrument is used to apply different matrix suctions to the test soil step by step, so that the sample is in a balanced state under different levels of matrix suction, and the final corresponding water content of the test is determined. The change reversely calculates the volumetric water content of the sample under different matrix suction, and draws the soil-water characteristic curve of the sample, as shown in Fig. 1.

**Fig. 1.** Soil-water characteristic curve of sample soil

## 3 Model Formulation

Using the ABAQUS finite element analysis software, a three-dimensional finite element model of granite residual soil slope was established. The residual soil slope cohesion force was 30 kPa, internal friction angle was taken 36°, elastic modulus  $E = 40$  MPa, Poisson's ratio  $\nu = 0.35$ , soil dry density  $\rho_d = 1.58$  g/cm<sup>3</sup> and bulk density  $\gamma = 10$  KN/m<sup>3</sup>. The slope angle of the slope is taken as 35°. The constitutive model of the soil is selected as MC model, and the size and meshing of the finite element model are shown in Fig. 2.

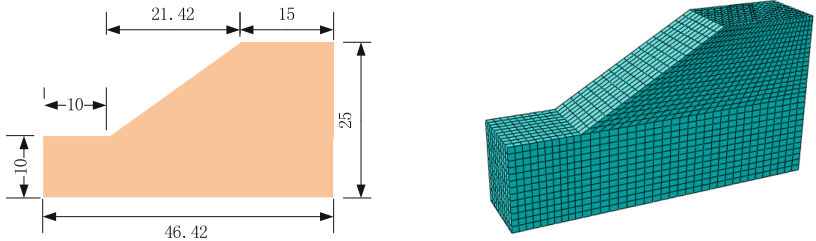


Fig. 2. Finite element model of granite residual soil slope

### 3.1 Variation Trends of Strain and Shear Zone of Granite Residual Soil Slopes

Change the initial dry density value of the soil and choose three different dry densities, namely  $\rho_d = 1.58 \text{ g/cm}^3$ ,  $\rho_d = 1.71 \text{ g/cm}^3$  and  $\rho_d = 1.84 \text{ g/cm}^3$ . Using the strength reduction method, the strain and shear band variation characteristics of the granite residual soil slope at different dry densities are calculated, as shown in Figs. 3 and 4.

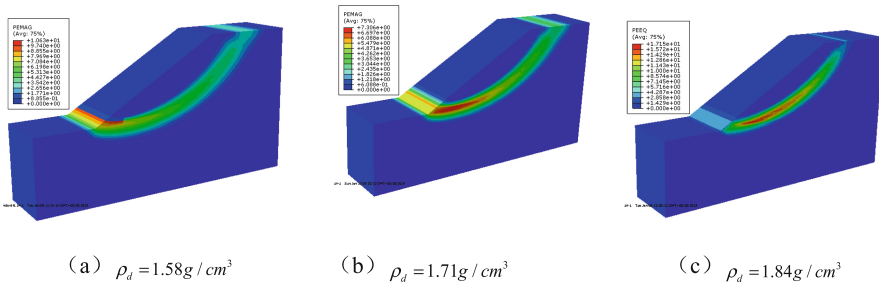


Fig. 3. Cloud map of strain change in plastic zone of granite residual soil slope

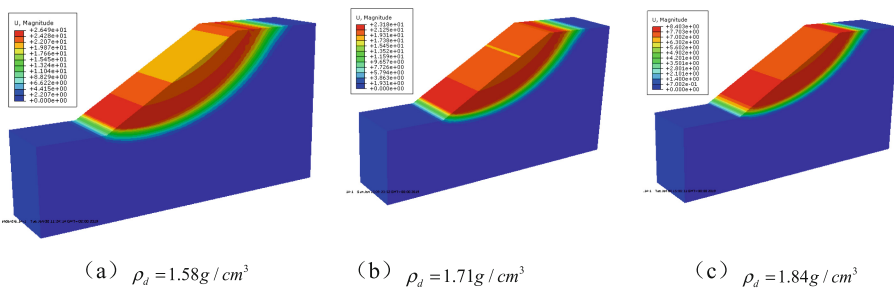


Fig. 4. Cloud maps of the shear zones of granite residual soil slopes

It can be seen from Figs. 3 and 4 that as the dry density continues to increase, the maximum strain in the plastic zone also increases, and the location of the maximum strain in the slope continues from the foot of the slope to the top of the slope as the dry density increases extension, the volume of the circular arc shear zone of the slope is continuously decreasing, and the trend of upward position is obvious, which shows that with the increase of dry density, the shallow slope of the slope first slides, that is, the rate of slope instability is increasing quickly.

### 3.2 Safety Factor of Granite Residual Soil Slope

Based on the strength reduction method theory, using the ABAQUS finite element analysis software to calculate the variation law of the safety factor of the stability of the granite residual soil slope with three different dry densities, as shown in Fig. 5 and Fig. 6. It can be seen from the figure that as the dry density increases, the granite residual soil shear zone damage and instability characteristics become more significant, the maximum shear zone displacement increases continuously, and the stability safety factor of the granite residual soil slope continues to decrease, the largest safety factor value is close to 2, the minimum safety factor value is close to 1, and the safety factor values obtained under different instability criteria are relatively close.

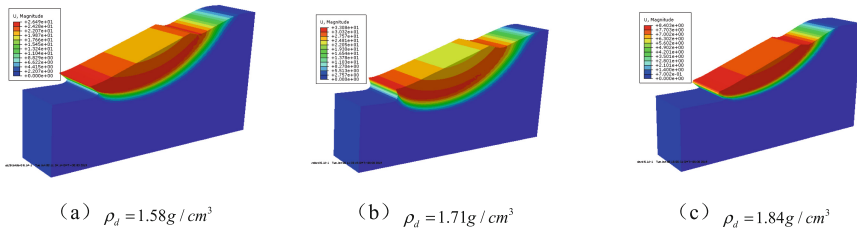


Fig. 5. Cloud image of ultimate failure state of granite residual soil slope

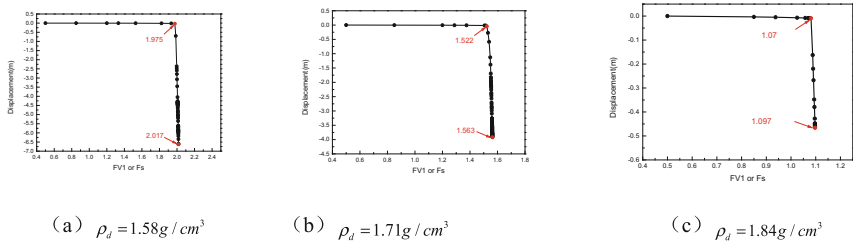


Fig. 6. Relationship between stability factor and horizontal displacement

Taking the sudden displacement inflection point of the characteristic part of the slope and the non-convergence of finite element numerical iteration as the criterion of slope instability, the safety factor of slope under two different instability criteria can be obtained, as shown in Table 2:



**Table 2.** Safety factor of granite residual soil under two different criteria

Criteria	Dry density		
	$\rho_d = 1.58 \text{ g/cm}^3$	$\rho_d = 1.71 \text{ g/cm}^3$	$\rho_d = 1.84 \text{ g/cm}^3$
Displacement inflection point	1.975	1.522	1.07
Numerical iteration method	2.017	1.563	1.097

The calculation results show that the non-convergence of the displacement inflection point of the slope characteristic point is used as the instability criterion, and the safety factor is slightly smaller than the value obtained by using the finite element numerical iterative non-convergence as the instability criterion, and the difference between the two is close to 0.03, Which also shows that it is safer to use the displacement inflection point of the characteristic point as the criterion of slope instability; under different dry densities, as the dry density continues to increase, the safety factor shows a trend of decreasing, and the slope is instability and deformation The displacement value increases continuously, and the arc-shaped sliding surface shows an obvious sliding trend.

### 3.3 Instability and Failure Characteristics Analysis with Fluid-Solid Coupling Theory

A three-dimensional finite element model of granite residual soil slope was established in Abaqus software to simulate the change law of soil stress and strain under the condition of rainfall infiltration, and the stability of the slope under the coupling of seepage and flow was analyzed. It can be seen from the calculation that the pore water pressure in the slope is linearly distributed before the rainfall, and the pore water pressure gradually increases from the top to the bottom of the slope, the maximum pore pressure is 100 kPa, and the saturation of the slope soil body is based on the groundwater level as the boundary. The soil above the site is unsaturated soil, and its saturation is linearly distributed, which decreases continuously from bottom to top, and the pore water pressure also decreases as the saturation decreases. At the same time, the initial effective stress of the slope soil gradually increases from the slope to the slope. The stratification effect of the initial effective stress from the slope to the slope is very obvious. The maximum initial effective stress is close to 200 kPa. During rainfall, the changes of pore water pressure and saturation in the slope are shown in Fig. 7 and Fig. 8.

It can be seen from Fig. 7 that during rainfall, the pore water pressure of the soil above the groundwater level gradually decreases with the duration effect of rainfall, and the matrix suction also continuously decreases; from Fig. 8 we can see that under the rainfall duration effect, the groundwater in the soil The saturation above the gradual increase gradually, the saturation increase value in the initial 12 h is greater than the saturation increase value in the same period thereafter, this phenomenon shows that as the rainfall continues, the rain fills the pores in the soil body, resulting in the reduction of water infiltration channels compared with the initial saturation before the rain, the soil saturation of the slope increases significantly after the rain. Under the effect of rainfall duration, the soil is getting closer to the saturation state. The results show that:

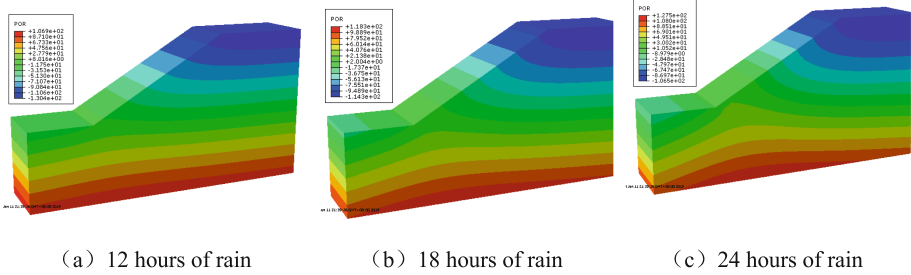


**Fig. 7.** Cloud image of slope pore water pressure under different rainfall duration

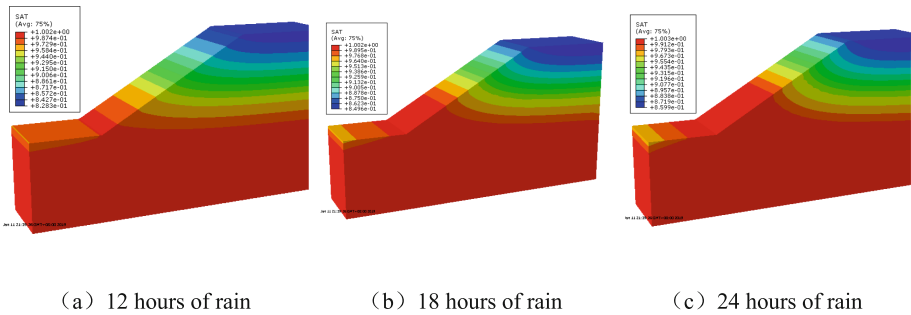


**Fig. 8.** Cloud chart of slope saturation change under different rainfall duration

under the action of rainfall, the pore water pressure of the soil decreases with increasing saturation, and the difference between the pore gas pressure and the pore water pressure of the soil is the suction of the soil matrix, which varies with the saturation increases and decreases. Under the effect of rainfall infiltration, the coupling effect of soil particles and rainwater in the slope will further aggravate the instability and failure of the slope. The simulation results are shown in Fig. 9. It can be seen from Fig. 9 that after 12 h of rainfall, the plastic strain first appeared at the foot of the slope. With the extension of rainfall time, the plastic strain interval in the slope gradually extended from the foot of the slope. After 24 h of rain, the plastic strain concentration first appeared at the foot of the slope. This is because after rainfall infiltration, the soil matrix suction decreased, the pore water pressure increased, and the effective stress continued to decrease. At this time, the maximum displacement vector of the slope appears in the shallow foot of the slope, and the whole slope has a tendency to slide and deform. The shallow foot of the slope is the weakest point of the entire slope. Therefore, a reasonable prediction of the extent of strain extension in the plastic zone and the location of the strain concentration in the plastic zone has important engineering significance for the judgment of slope instability and slope reinforcement.

## 4 Conclusions

The related theories and calculation methods of the influence of rainfall on the stability of homogeneous unsaturated granite residual soil slope are studied. The stability of the

slope during and after the rainfall under different working conditions is calculated by combining examples. The following conclusions can be obtained:

- (1) The rainfall intensity and duration have a significant impact on the slope safety factor. If the rainfall rate is constant, the rainfall time is long enough, the safety factor will continue to decline for a period of time, and then tend to stabilize.
- (2) The dry density of granite residual soil is different, and the stability safety factor of the slope will also be different. The results show that with the increasing dry density, the stability safety factor of the slope is decreasing. During the instability of the slope, the strain in the plastic zone first extends from the foot of the slope to the top of the slope. When the entire plastic zone of the slope is fully penetrated, the whole slope is damaged, the sliding surface of the slope is arc-shaped, and the instability of the displacement and inflection point of the characteristic point is used as the slope instability criterion. Compared with other instability criteria, the stability of the slope is safe.
- (3) Based on the seepage coupling theory, the study found that the initial pore water pressure distribution law, initial saturation and initial effective stress of granite residual soil slope have significant effects on the slope instability during rainfall. By simulating the changing law of the strain in the plastic zone at different moments, the whole gradual change process of slope instability under rainfall infiltration was vividly reflected, and the changing law of the horizontal displacement and vertical settlement of the slope was also analyzed. The results show that during rainfall infiltration, soil saturation is negatively correlated with changes in pore water pressure, and plastic strain occurs first at the foot of the slope. Under the effect of rainfall duration, the strain in the plastic zone of the slope extends upward from the foot of the slope, and the plastic strain of the slope foot extends upward to a certain range.

**Acknowledgments.** This study was financially supported by Hunan Natural Science Foundation of China (No: 2019JJ60010 and No: 2019JJ60070).

## References

1. Fredlund, D.G., Rahardjo, H.: *Soil Mechanics for Unsaturated Soil*. China Architecture and Building Press, Beijing (1997)
2. Moriwaki, H., Inokuchi, T., Hattanji, T., Sassa, K., Ochiai, H., Wang, G.: Failure processes in a full-scale landslide experiment using a rainfall simulator. *Landslides* **1**(4), 277–288 (2004). <https://doi.org/10.1007/s10346-004-0034-0>
3. Lin, H.Z., Yu, Y.Z., Li, G.X., et al.: Influence of rainfall characteristics on soil slope failure. *Chin. J. Rock Mech. Eng.* **28**(1), 198–204 (2009)
4. Zhang, J.M., Wang, R., Zhang, G.: Centrifuge modeling of rainfall-induced deformation of slopes with weak layers. *Chin. J. Geotech. Eng.* **10**, 1582–1587 (2010)
5. Ng, C.W.W., Shi, Q.: Influence of rainfall intensity and duration on slope stability in unsaturated soils. *Q. J. Eng. Geol.* **31**(part2), 105–113 (1998)

6. Zhao, H., Song, E.X.: A method for predicting co-seismic displacements of slopes for landslide hazard zonation. *Soil Dyn. Earthq. Eng.* **40**, 62–67 (2012)
7. Nuth, M., Laloui, L.: Effective stress concept in unsaturated soils: Clarification and validation of a unified framework. *Int. J. Numer. Anal. Methods Geomech.* **32**(7), 771–801 (2008)
8. Tang, M.G., Xu, Q., Huang, R.Q., et al.: Experiment and analysis of suction of unsaturated soil in slope. *Chin. J. Rock Mech. Eng.* **25**(2), 355–362 (2006)
9. Wu, J.J., Wang, C.H., Li, G.X.: Influence of matric suction in unsaturated soils on slope stability. *Rock Soil Mech.* **25**(5), 732–736, 744(2004)



# Development and Field Testing of Geocomposite Cellular Mats (GCM) to Minimize the Ground Movements of Highway Embankments Founded on Peat Ground

Tuan Noor Hasanah Tuan Ismail<sup>1</sup>(✉), Devapriya Chitral Wijeyesekera<sup>2</sup>,  
and Ismail Bakar<sup>3</sup>

<sup>1</sup> Faculty of Technology Engineering, Universiti Tun Hussein Onn Malaysia, Parit Raja,  
Johor, Malaysia

hasanah@uthm.edu.my

<sup>2</sup> University of East London, Docklands Campus, University Way, London E16 2RD, UK

<sup>3</sup> Faculty of Civil and Environmental Engineering, Universiti Tun Hussein Onn Malaysia,  
Parit Raja, Johor, Malaysia

**Abstract.** Challenging grounds are often met in planning, design and construction of highway embankments which as a consequence succumb to undesirably excessive ground movements. Such ground conditions can range from unforeseen cavernous grounds to soft compressible organic soils of variable depths. Often alternate route planning is not feasible, and if necessary alternative construction procedures are not adopted, the net result will be unwanted roads user discomforts such as bumpy roads or even fatal road collapse. Highway constructions norms to circumvent such occurrences are to replace with alternative transported foundation soil/ground improvement or use an appropriate form of geo mats. Hence, this paper presents an alternative and innovative lightweight fill material: Geocomposite Cellular Mat (GCM) used to minimize the ground movements of highway embankments over peat ground. The conceptual development of a stiff mat structure but with a weight lighter than the embankment fill soil is described. The material used for the stiff mat is environmentally friendly in utilizing recycled plastic and its structure, enabling the free movement of water to dissipate any excessive pore water pressures. The performance of the GCM was appraised under field trial conditions on a test site in Parit Nipah, Johor, Malaysia. The site comprised of a vast expanse of hemic peat and environmental conditions at the test site were fully monitored. The geotechnical properties of the peat at Parit Nipah were typically high organic matter content (~85%), high moisture content (>600%) and very low undrained shear strength (<15 kPa). Details of the set up and layout of the trial embankments tested are fully described, and the techniques adopted to get a comprehensive narrative of the settlement characteristics using innovative measurement techniques are also described. The performance of the GCM incorporated embankment was compared with that of a similar embankment that was formed of conventional backfill (sand fill). The findings show that the field ground movement observations confirmed that the maximum settlements were reduced by up to 84% with the GCM fills. Moreover, the differential settlements were reduced by up to 70%.

## 1 Introduction

“The necessity to have well documented full scale field tests of trial embankments” was strongly voiced at an International Symposium on Trial Embankments on Marine clays over three decades ago (Balasubramaniam et al. 1990). A holistic understanding of the geotechnical properties of both the embankment fill and the founding Muar Flats was desired to make a good prediction of the embankment behaviour. This paper describes some field test on embankments at a dominantly peat site in Parit Nipah, (only about 20 km away from Muar, Johor) but in a very different geo environment. It is a prime engineering prerogative to enhance the stiffness of a road subgrade and/or subbase that will have the potential to arrest any indiscriminate road settlement that leads to uneven and bumpy road surfaces. The wide variability of properties and materials encountered in geotechnology demands the applications of Genetic Engineering to bridge between idealist and realism (Ebid 2004). Highway embankments settle when constructed over soft soil subgrades, including silty, clayey and in particular peat. These are very frequently encountered hazardous problems that demand maintenance and repair of such soil-structure scenarios. Figure 1 gives a simple, local example from Malaysia (Kolay et al. 2011). Challenging soft soils have also been described by Zainorabidin and Wijeysekera (2007), Huat (2004), Edil (2003), Zainorabidin and Bakar (2003), Jarret (1997), Mutalib et al. (1991), Andriesse (1988), Hobbs (1986) and Barden (1968). Such soils are characterised by weak shear strength, low stiffness with long term creep characteristics (a consequence of significant secondary and tertiary consolidation), high moisture content and continuous biodegradation. Consequently, soft peaty soils tend to settle in the short term and then progress to consolidate further with time, much more than firmer soil that have lower natural moisture content.



**Fig. 1.** Hazardous settlement of approach road with peat ground subsidence in Sibul, Sarawak, Malaysia (Kolay et al. 2011)

Infrastructure constructions on varying compressible soils cause many post construction problems. Hence, some pertinent, sustainable and lasting remedial geo-techniques are urgently desired to ensure embankments and structures constructed on such problematic ground remain stable and strong to mitigate excessive settlement and/or bearing

failure. Past literature documents various alternative construction and stabilisation methods; intrusive methods (chemical stabilisation, prefabricated vertical drains) or external methods (surface reinforcement, preloading, sand or stone column, and piles) have been suggested and adopted to support structures over soft yielding ground (Huat et al. 2005; Kadir 2009; Construction Research Institute of Malaysia 2015). However, some of these technologies are constrained by their demands on technical feasibility, space and time limitations and process economics. Even after the adoption of these procedures, differential settlement problems can still remain unaddressed. These methods aim to have the initial peat layer thicknesses reduced by over 50%, with a simultaneous increase in preconsolidation pressure and undrained shear strength. However, such methods are both expensive resource intensive, time-consuming and need safe site access for heavy machinery.

Innovative use of lightweight fill technology has been adopted in construction on the soft yielding ground for over three decades. The increase in stress on the subsoil can be reduced so that the settlement is reduced or even eliminated/compensated via the geotechnical concept of “buoyant/floating foundation” if the road embankment is constructed out of fill material lighter than conventional fill (14–20 kN/m<sup>3</sup>). Hence various types of lightweight materials (sawdust, fly ash, slag, cinders, cellular concrete, lightweight aggregates, expanded polystyrene (EPS), shredded tires, and seashells) have been proposed as fills for road embankment construction (Ismail et al. 2019). Table 1 gives properties of some such fills. Most lightweight fills are primarily particulate from that of EPS blocks, which are light (<0.4 kN/m<sup>3</sup>) with low water absorption (<2%). However, EPS blocks have inherent technical challenges of uplift, leading to buoyancy failure, flammability of EPS and being susceptible to rodent attack. The research reported in this paper utilized a potential replacement of the conventional or modified fill material to one that is manufactured and has a cellular lightweight mat structure, referred to as Geocomposite Cellular Mat (GCM).

**Table 1.** Physical properties & performance of some lightweight fills

Lightweight fill	Description	Density (kg/m <sup>3</sup> )	Compressive strength (kPa) @ 10% strain	Initial stiffness (kPa)	Approx. cost (RM/m <sup>3</sup> )	Performance concerns
EPS	Expanded Polystyrene Ultra lightweight	<40	$0.4 \times 10^3$	$6.5 \times 10^3$	200	Hydraulic buoyancy: Flammable: Soluble with oil based products & Chemicals: Prone to rodent attack
Shredded tires	Used above ground water level	<920	80	0.4	90	Geo environment pollution:

(continued)

**Table 1.** (continued)

Lightweight fill	Description	Density (kg/m <sup>3</sup> )	Compressive strength (kPa) @ 10% strain	Initial stiffness (kPa)	Approx. cost (RM/m <sup>3</sup> )	Performance concerns
Wood fibre	Used below ground water	<1020	$0.83 \times 10^6$	$0.83 \times 10^6$	65	Combustible; Decomposable
Expanded clay	Non uniform Depends on compaction	<700	1.2	$4 \times 10^4$	185	Hydraulic buoyancy' Water absorption
Fly ash	Self hardening, non uniform, granular material	<1550	$1.2 \times 10^3$	$11 \times 10^6$	65	Wind erosion

## 2 Road User Safety and Comfort

By virtue of the benefit of the area covered land transport is the most convenient mode of transportation and the main element for a nation's economic development. Sound highway/urban road infrastructure coupled with efficient traffic management gives rise to riding comfort and road safety to their users. Highway design involves the selection of a road's dimensions and its visible features of alignment and controlling highway architecture. Their construction normally involves a vast amount of earthwork; cutting hilly areas, backfilling low lying areas, crossing wetlands and alike. Often in the case of road embankments, the interaction in the behaviour of its essential elements of the pavement, the embankment fill and the foundation provides the user with comfort or otherwise. A significant role is played by the respective construction industries to contribute to the development of a green road/highway, in being environmentally responsible, eco-friendly and sustainable. The condition of the road surface needs to be visually inspected with regular measurements of rut depths, longitudinal evenness to be acceptable to predefined guidelines. The unsustainable common practice of indiscriminate use of transported earth backfill can be replaced with the adoption of an appropriate choice of a lighter backfill given in Table 1. This will have the added benefit of not imposing undesirably higher stresses on soft foundations leading to excessive deformations of the foundation, which will be reflected in giving an uneven road surface.

Conventional embankment fill comprises of well compacted earthen material used to fill a void space during the process of raising the natural ground surface to a predesigned grade level. Two types of granular materials (type 1 and type 2) is specified by the Department of Transport (UK) for road works. Type 1 is a well graded aggregate of crushed rock, well burnt colliery shale with a notable absence of plastic fine grained soil. Type 2 includes additionally natural sand and gravel with an upper limit of 6%



of particles finer than 425  $\mu\text{m}$ . When used as a subbase, CBR (California Bearing Ratio) value of such compacted fills must be higher than 20% and needs protection from wet conditions. The durable performance of a pavement depends on the subgrade with particles finer than sand in it gives lower CBR values and yields unfavourable support to the pavement.

Such particulate fills with low stiffness lack rigidity and imposes a non-uniform stress distribution on the foundation. Consequentially, the settlement of the embankment often closely follows the pattern of the stress distribution giving a characteristic bowl shaped deformation. This in turn can cause severe damage on the overlying layers of the pavement-fill system (Fig. 2). Johansson (2010) used a hydrostatic profiler which can determine the relative movements of a flexible hose buried integrally into the foundation along with fill foundation interface, in order to verify this deformation pattern. Allowable/acceptable settlement will depend on the importance of the infrastructure, the pavement type (flexible/semi rigid or rigid) and factors such as any differential settlement risks. The roadway’s economic life may be considered tolerable if the settlements are uniform and occurring slowly over time.

The behaviour of the pavement-fill-foundation system is best and realistically studied only through well instrumented and monitored full scale trial embankments. Studies using software programs and small scale models have also been done. Table 2 gives summary details of such studies relevant to the core focus of this paper; Peat ground. Outline of the challenges with peat ground follows this.

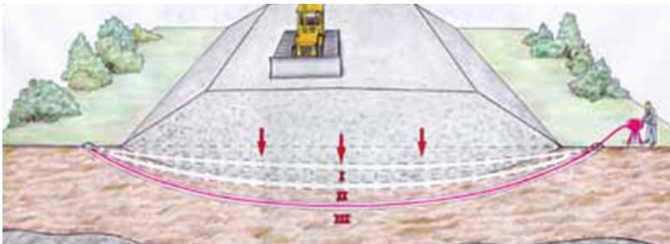


**Fig. 2.** Settlement pattern at the fill foundation interface made with hydrostatic profilometer observations (Johansson 2010).

**Table 2.** Outline of some published research studies of trial embankments founded on peat ground.

Site name	Muar clay plain, Malaysia	Booneschans, Netherlands	Parit Nipah, Johor Malaysia	Parit Nipah, Johor Malaysia
Geometry of embankment	55 × 90 × 2.5 m	750 × 100 × 6 m	3,5 × 1 × 1 m	3.6 × 3.6 × 0.15 m concrete raft
Principal foundation soil	17.8 m of Marine Muar soft silty clay	1.8 m clay layer overlying peat	Peat	Peat

(continued)

**Table 2.** (continued)

Site name	Muar clay plain, Malaysia	Booneschans, Netherlands	Parit Nipah, Johor Malaysia	Parit Nipah, Johor Malaysia
Thickness of and depth to peat layer	0.6 m thick peat layer at a depth from 17.8 m	2 m thick peat layer at a depth from 1.8 m	4 m thick peat layer from the ground surface	4 m thick peat layer from the ground surface
Field tests and instrumentation	Settlement gauges, piezometer, inclinometer, settlement rings, heave markers, piezocone	CPT, Begemann sampling system (boreholes), inclinometer, pore pressure transducer, trial pit	Boreholes, well points for water table depths, Visual observation of fill deformation Environmental monitoring	Geodetic surveying method. TOPCON AT-B4
Embankment fill composition	Well compacted fill	Sand core with a clay cover on top	Layers of Geocomposite Cellular Mat (GCM) topped with Uniformly compacted sand fill	Sand bags on Concrete raft
Research methodology/ies	Total and effective stress slip circle analysis. CRISP Finite element analysis	Use of sensors to detect movement before failure	Settlement observations and Validating Large strain consolidation predictions	Installation of slab to reduce/minimise settlement
Reference/s	Balasubramaniam et al. (1990), Indraratna et al. (2010) and Brand (1991)	Zwanenburg et al. (2005)	Ismail (2017) Ismail et al. (2014a, b)	Zainorabidin et al. (2019)

### 3 Geotechnical Challenges Associated with Malaysian Peat Ground

In a strict geotechnical engineering context and as adopted by the extended Malaysian Soil classification System, Peat is defined as soil with more than 75% organic content (ASTM D4427-92 1997; Jarret 1995). Furthermore, contrary to normal soils, the composition and properties of peat deposits are both non homogeneous and is subjected to a dynamic and conflicting process of disintegration cum preservation under very moist anaerobic conditions environments, akin with the formation of bogs, moors, muskeg, mire, tropical swamps and fens (Landva 2007). Peat further defies one of the Terzaghi

assumptions in soil mechanics, in that the peat particles themselves are variably compressible. Tropical woody peat found in Malaysia consist of semi-decomposed to decomposing plant remains of tree stumps, roots and leaves and the peat in Johor, Malaysia is dark reddish brown to black and have been formed as varying thicknesses and in an acidic environment. The renowned Von Post peat classification system in use is based on categorization in accordance with botanical composition, degree of humification, moisture content, content of fine and coarse fibers and content of woody remnants. The von Post scale for peat has a spread ranging from H1 (completely unhumified fibrous peat) to H10 (completely amorphous non fibrous peat). Hobbs (1986) extended the classification system to include categories for organic content, tensile strength, odour, plasticity and acidity. Based on the extent and type of fiber content, they are also referred to as Fibric (>66%), Hemic (33–66%) and Sapric (<33%). The unique geotechnical characteristics of peat soil are a high moisture content (>200%), high compressibility ( $C_c > 0.5$ ), high organic content (>75%), low shear strength (5–20 kPa) and low bearing capacity (< 8 kN/m<sup>2</sup>). Such attributes of peat are the cause of undesirable geotechnical challenges with peat ground to the engineers in the field of construction. Table 3 gives a summary of published geotechnical information on Malaysian Peat Soils.

**Table 3.** Published geotechnical properties of some Malaysian Peat soil

Geotechnical characteristic	Peat soil - location		
	West Malaysia	Johore Hemic Peat	East Malaysia
Source reference	Huat (2004)	Zainorabidin and Ismail (2003)	Huat (2004)
Natural moisture content (%)	200–700	230–500	200–2207
Organic content (%)	65–97	80–96	50–95
Liquid limit (%)	190–360	220–250	210–550
Plastic limit (%)	100–200	–	125–297
Specific gravity	1.38–1.70	1.48–1.8	1.07–1.63
Unit weight (kN/m <sup>3</sup> )	8.3–11.5	7.5–10.2	8.0–12.0
Undrained shear strength (kPa)	8–17	7–11	8–10
Compression index, $C_c$	1.0–2.6	0.9–1.5	0.5–2.5

By virtue of its genesis, peat is necessarily heterogeneous; far from uniform and homogeneous, even within a single laboratory sample. The macro/micro structure of deposits of natural peat is in a continuing process of dynamic diagenesis with humic acid interaction. Peat soils are recognized to be dark reddish brown to black with acidic (pH ~ 3) pore fluid. Table 2 shows that some researchers' claim that peat is not actually plastic per se, as a plastic limit cannot be determined. A further dilemma is that whether peat is granular or cohesive in shear. The macrostructure of peat shows a network of

fibers that defines any pseudo frictional characteristics of peat (Zainorabidin et al. 2010). Kogure et al. (2003) suggested a multi-phase system for peat comprising of solid organic, mineral soil particles, and water in the inner and outer voids. These nonconformities are prime reasons for the classical secondary/tertiary consolidation behaviour ( $C_{\alpha}/C_c \sim 0.06$ ) of peats that leads to indiscriminate settlements. Ground subsidence is essentially a consequence of volume change except in the cases where lateral ground movements induced by shear movements. Peat is very susceptible to volume change that may arise due to any one or combinations of the following three different causes, which are;

- (i) Consolidation of peat due to an increase in effective stress,
- (ii) Shrinkage resulting from the movement of the free moisture consequent to a change in the thermal or hydrological environment, and
- (iii) The cracking of the otherwise peat continuum due to aggressive and hostile thermal environments leading at times to irreversible break down of the cell structure of the decaying tree roots and other biological remains.

Wijeyesekera and Patel (1998) and others have outlined settlement predictions using a numerical analysis approach for the solution of Gibson's large strain consolidation, which is based on the use of Lagrangian coordinates in preference to the Cartesian coordinates. This still leaves the inability to account for the biological cell breakdown as well as to the volumetric deformations arising from drying shrinkage. Notwithstanding these indispensable setbacks to the modelling of peat, notable constructions have been done in Malaysia and elsewhere on Peat ground, viz; Kuala Lumpur International Airport (KLIA) and urban development in Sibuluan Town (Sarawak), Malaysia. Any soft ground improvement design needs to ensure the stability of the structure as required in the technical specifications (and in the case of a road embankment, to settlement limits after a specified lapse of time from construction, set at the road center and also on a maximum residual differential settlement).

## 4 Geocomposite Cellular Mat (GCM) Technology

In their quest for an environmentally sustainable solution to the challenges imposed by peat ground on road construction, the authors developed the GCM (Fig. 3) as a further alternative lightweight fill. This research focused on the development and field testing of GCM which is a pronounced improvement on the "Lightweight Blocky" basis adopted in the use of "Expanded Polystyrene" (EPS) blocks but taking on board the following considerations.

- The GCM to be made of recycled waste plastic and having a distinctive honeycomb like cellular structure that makes them marginally heavier, stiffer and stronger than the EPS, and also negates any buoyancy failures in the GCM being more porous and permeable.
- The adoption of recycled waste plastic Polypropylene as a useful material source and also to improve environmental sustainability significantly while supporting the sustainable trend of the circular economy.

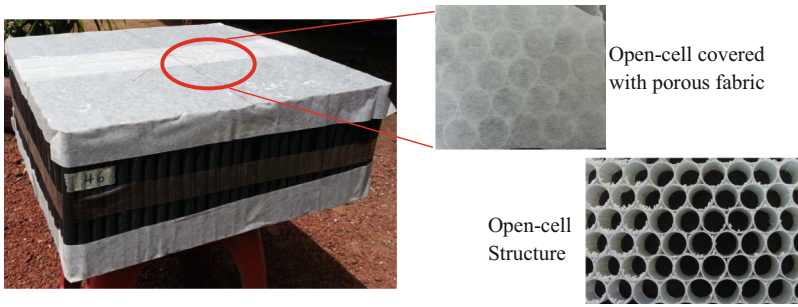


**Fig. 3.** Structure of Geocomposite Cellular Mat (GCM) block

The GCM technology (Wijeyesekera et al. 2015, 2016; Ismail 2017) is based on the adoption of a relatively firmer foundation structure than a flexible one and thereby anticipates a more even/uniform structural settlement. Particularly in the niche area of Foundation Structure – Soft Soil interaction studies, the vertical displacements and subgrade reactions at the interface of the foundation structure depends on both the soil stiffness and the rigidity of the foundation (Leshchinsky and Marcozzi 1990). A rigid interface enables to negate any non-uniformity (heterogeneity of the subgrade) and redistribute the contact subgrade reactions resulting in a uniform rigid foundation settlement. Intrusive ground improvement techniques, viz. soil stabilization, if not adequately controlled (through uniform admixing and/or specified field compaction) will still produce a particulate and heterogeneous soil, even though it be, at a reduced order of variability.

As outlined by Arellano (2010), Lightweight Fill Technology in highway engineering relies not only on improving engineering properties of the fill but also in reducing the weight of the levee of the embankment and thus the stresses applied on the soft foundation soil. Cellular solids have a macro/micro structure that can have a form ranging from the near perfect order in beehive honeycomb structure of disordered three dimensional networks found in sponges, foams and also in the biological tissues of cork cells or even in mammal/human skins. Open/closed cell polyurethane is found in the EPS blocks adopted as a form of lightweight fill in ground improvement. A closed and ordered connectivity of the individual cell edges and faces is hard to establish in the polyurethane cells, which limits the porosity and more so the intrinsic permeability. Relative density/specific gravity is an important parameter which contributes to the strength of the cellular structure. Thin walled cellular structures have a lower relative density (polymeric foams 0.05–0.2; natural materials, cork ~0.14; two dimensional structures in honeycomb and porous solids >0.3). Thus the physical, mechanical and thermal properties of cellular solids are influenced by a variety of factors including relative density, cell geometry and cell topology. The many advantages in cell structure technology have been harnessed via engineering material science in the manufacture of the body in aircraft technology and honeycomb sandwich technology adopted in building systems in such as lightweight partition walls. An exciting advantage of cellular structures is the auto compensation of any non performing cells by the rest, within reasonable limits. The use of geocells in highway engineering is an example of its application with the collapsible (for packing

purposes) but the honeycomb shaped interconnected cells provide the needed all-round confinement to completely encase the heavy granular fill that are placed within the cells.

Development of GCM is principally focused on being green and sustainable with the use of recycled waste plastic having a density ranging from 110 to 125 kg/m<sup>3</sup> and an average specific gravity of 0.915. The specific gravity of the GCM block indicates that the GCM will float but is not much lighter than water (only 10% lighter). Therefore submergence plus additional loading from wearing surface, and road base will significantly decrease the buoyancy of the GCM. Thus, GCM can be classified as a safer fill material when compared with the EPS fill which has a low specific gravity approximately 0.01 to 0.03 (which is 98% lighter than specific gravity of water) as reported by Zornberg et al. (2005). The water absorption of GCM is less than 0.01%, it was achieving equilibrium value at 1day, since polypropylene (PP) does not absorb any significant amounts of water.

GCM block fill possesses far superior mechanical bearing characteristics. GCM fill has a high compressive strength ranging from 3.8 to 4.5 MPa, the initial stiffness at 1% strain was observed to be in the range of 100 to 150 MPa, and secant stiffness was around 190 to 310 MPa. These values are more than 50% higher compared to EPS geofoam. As noted by Zornberg et al. (2005), the maximum compressive strength and initial stiffness of EPS is around 0.04 to 0.49 MPa 4 to 10 MPa, respectively. The idealised cellular structure adopted in this technology allows water to flow freely and vertically (unidirectional), and it also reduces the potential of floating due to open porous structured cells (Fig. 3). Furthermore, the open-porous cellular structure of the GCM facilitates accelerated consolidation settlement within the sub-grade through rapid dissipation of the excess pore water pressure developed. Both top and bottom surface of the open-porous GCM was covered with high strength filter fabric to avoid soil particle from passing through them. GCM follows the masonry brickwork/ blockwork concepts closely, and are made in block form. Placement of the GCM blocks can be empirical or with a rational analysis to form the entire embankment with an appropriate spacing and arrangement patterns for the blocks. Therefore additionally, the concept of a cellular mat structure with interspersed blocks further enables the sharing of the load and minimising the differential settlement. The performance of this technology constructed on peat soil is critically studied in this research.

## **5 Geo Environmental Observations at the Field Test Site (Parit Nipah, Johor, Malaysia)**

Field testing was conducted at Parit Nipah Darat (Johor, Malaysia). Ground investigations at the site consisted of drilling 4, 10 m deep boreholes and field vane shear tests carried out that revealed a peat layer extending to approximately 4 m in depth, which in turn was underlain by a layer of soft clay. This has been further confirmed recently by Basri et al. (2019) with subsurface profiling using Electrical Resistance Tomography results for the 2-D stratigraphy profiles obtained shown in Fig. 4. The image shows a clear contrast between different soil layers confirming the peat thickness. The natural moisture content of the peat obtained from the site ranged from 698% to 721%. The laboratory observations of the unit weight of peat soil were in the range of 920 to 1100 kg/m<sup>3</sup>,

and the specific gravity of peat particles was about 1.436. Vane shear strength recorded for peat layer ranged from 8 to 14 kPa. These conform to the expected characteristics of peat to have low shear strength and consequently low bearing capacity inducing large strain settlements and even shear failure.

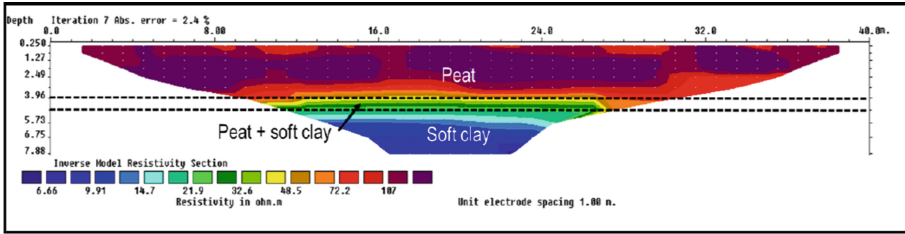


Fig. 4. 2-D ERT stratigraphy profiles for Parit Nipah Darat (adopted from Basri et al. 2019)

Environmental (rainfall, air temperature, humidity, groundwater table fluctuation and ground surface subsidence) conditions at the site were regularly monitored during the testing program. These enabled to compensate for errors arising from the environmental effect in order to obtain the net settlement data arising solely from respective fill loadings only. Temperature and humidity data as in Fig. 5 were measured using digital temperature and humidity meter to the nearest 0.1 °C and 1%, respectively. It was monitored throughout a research testing period. The temperature observations during the test period ranged between 22 °C and 30 °C. High ambient temperatures and low humidity reduce soil moisture and vice versa. Figure 6(b) shows the variation in humidity observed at Parit Nipah test site to be in the range of 78 to 89%.

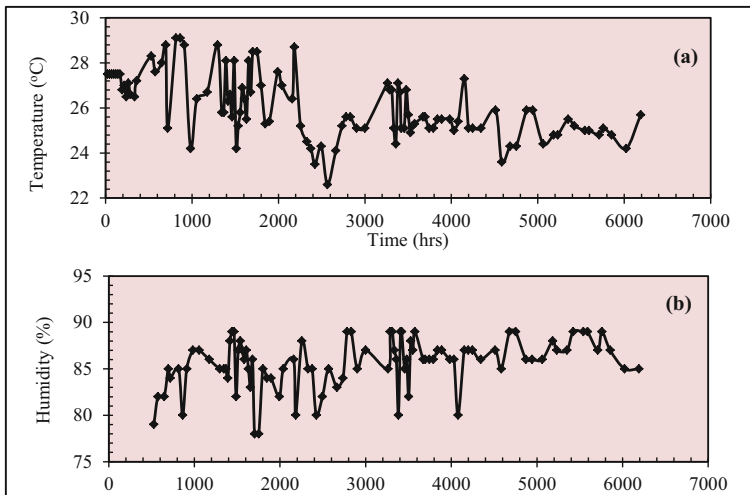
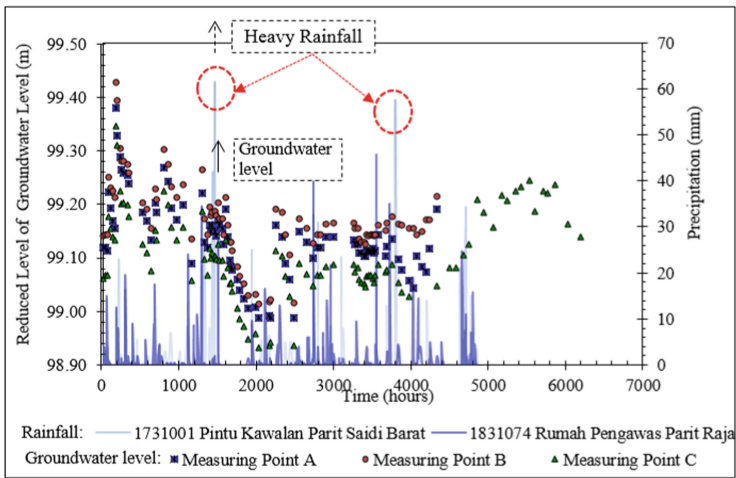


Fig. 5. Temperature and humidity variations observed at the test site

Groundwater level observations were made at three different but permanently installed standpipe locations on the test site. A stiff flat measuring tape with a readable accuracy of 0.001 m was used to ascertain the depth to local groundwater table. The measuring probe incorporated an insulated gap between electrodes to give an audible signal when it made contact with the water. The groundwater level variations depended on various factors such as water extraction demand by vegetation, local dewatering, but primarily the rainfall. Figure 6 is a comparison of the groundwater level changes in the peat layer on a backdrop of the observed rainfall. An extreme fluctuation of 27.7 cm in groundwater level was observed with intermittent rise and fall in its level, responding to the rainfall intensity and occurrence.



**Fig. 6.** Variation of local groundwater level in response to rainfall with time at the test site

## 6 GCM Technology – Field Performance

The performance of the GCM was closely observed in a real field environment at the site and analyzed. The superstructures were kept under canvas cover so that the test fills only were protected from wind and rain. The need to obtain holistic settlement observations at points on the loaded bases and beyond was a prime objective accommodated to fit the limits of time and available research funding. Environment tests mentioned above and innovative improvised instrumentation were adapted to measure surface settlements. Therefore, the adoption and installation of a large number of electronic settlement gauges needed and hydrostatic profilers proved to be both expensive and challenging as it would disturb the soft peat soil. The number of measurement points needed was not thus compromised, and a geodetic surveying technique; Topcon AT-B4 auto level with fixed



individual staff at each measurement point was installed. Each levelling staff was fastened to a rigid base plate (100 × 100 mm) for stability and to provide a representative observation. The visible portion of each levelling staff displayed a securely attached barcode portion of a leveling staff. Hence remote observations were possible, avoiding the hassle of handling heavy levelling staff and also eliminating any disturbance of the many measuring points. Net ground movement (settlement or heave) was thus measured to an accuracy of 1 mm.

The GCMs were made in the laboratory as blocks which measured either 500 × 500 × 200 mm or 500 × 250 × 200 mm. In practice, the GCM could be custom made to a required size and shape. The blocks can be arranged in a staggered pattern to distribute the load evenly between the layers. Figure 7(a) shows a typical arrangement of the GCM blocks within an embankment. The blocks are surrounded by conventional fill at the top and on the sides. 400 mm thick fill on the top of the blocks, and beneath the road pavement was proved to be sufficient in a parallel research study. This paper presents results from two distinctly different series of research testing. First was series U of uniform loading, which conceptually represents the loading arising from the central portion of the embankment as illustrated in Fig. 7(b). The second was series E of embankment loading which comprised of the central part and the two levees (see Fig. 7) that impose a triangular loading on the base.

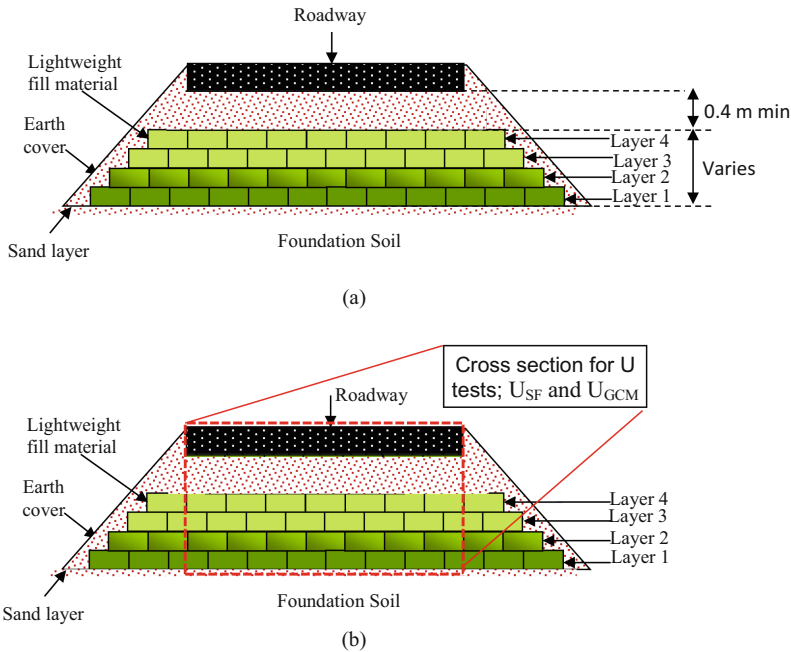
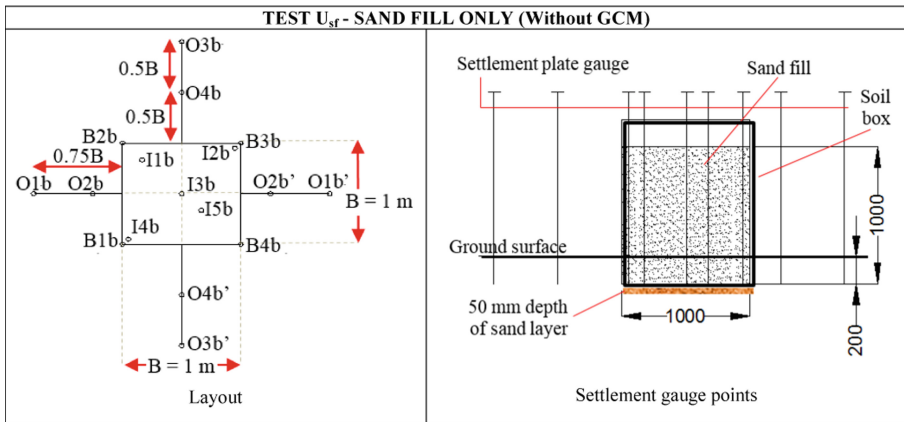


Fig. 7. Conceptual logic for the basis of  $U_{SF}$ ,  $U_{GCM}$  tests & the embankment loading tests

Figures 8 and 9 present information for/from the uniform loading tests  $U_{SF}$  and  $U_{GCM}$  and helps to compare the performance of the GCM fill with that of the conventional sand fill. Test  $U_{SF}$  consisted of 1000 mm of compacted sand fill only ( $\rho_d = 1400 \text{ kg/m}^3 \pm 2\%$ ) whereas  $U_{GCM}$  was with 3 layers of GCM ( $\rho_d = 125 \pm 10 \text{ kg/m}^3$ ) and 400 mm thick sand fill at the top. Nomenclature for the embankment loading test followed the same logic. The site preparation for both series was similar in first excavating and removing approximately 200 mm of top soil and spreading 50 mm depth of sand on the prepared surface. The base plate of each settlement gauge was placed level and positioned with a level zero assigned at specified observation points as shown in the layout diagrams. The vertical framed structure was used to contain the fills laterally. These were suspended carefully on to the prepared surface, ensuring that there was no additional loading imposed on the ground. Sand fill was placed within the frame/s in 5 uniformly placed layers of 200 mm each making up a 1000 mm thick fill. Contrarily, the GCM fills consisted of placing three layers of GCM blocks ( $3 \times 200 \text{ mm} = 600 \text{ mm}$  thick), and the balance 400 mm consisted of two layers of 200 mm thick sand layers that was placed on top of the GCM blocks. Therefore the total initial height of fill for each test was 1000 mm. The construction loading settlements occurring were monitored after the placement of each 200 mm fill. The settlement observations from all the gauges were monitored at regular intervals for the duration of the construction loading. The settlements were determined from the ground surface. Figures 8, 9 and 10 show the loading base dimensions for the U and E test series to be  $1000 \times 1000 \text{ mm}$  and  $3500 \times 3000 \text{ mm}$ , respectively. The locations for the settlement observation points were as indicated.



**Fig. 8.** Layout of uniform loading (sand fill only)

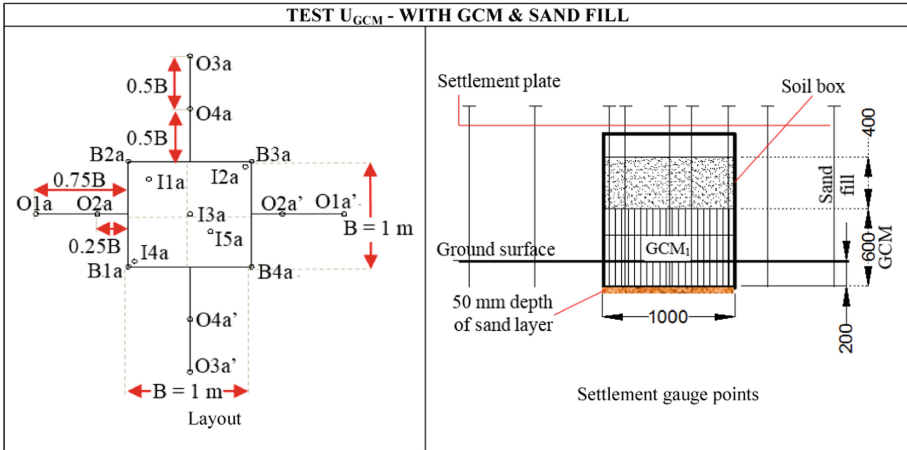
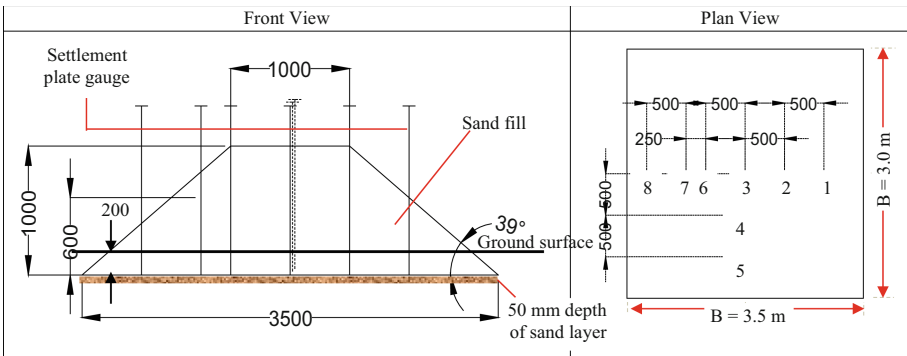
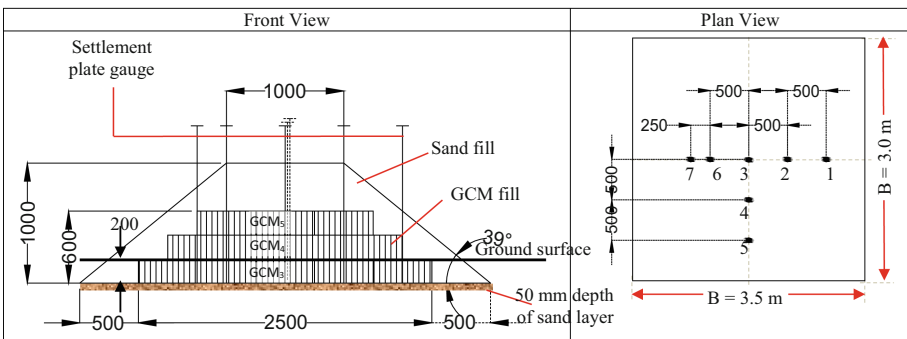


Fig. 9. Layout of uniform loading (GCM & sand fill)



(a) Test  $E_{sf}$  Sand Fill Only (Without GCM)



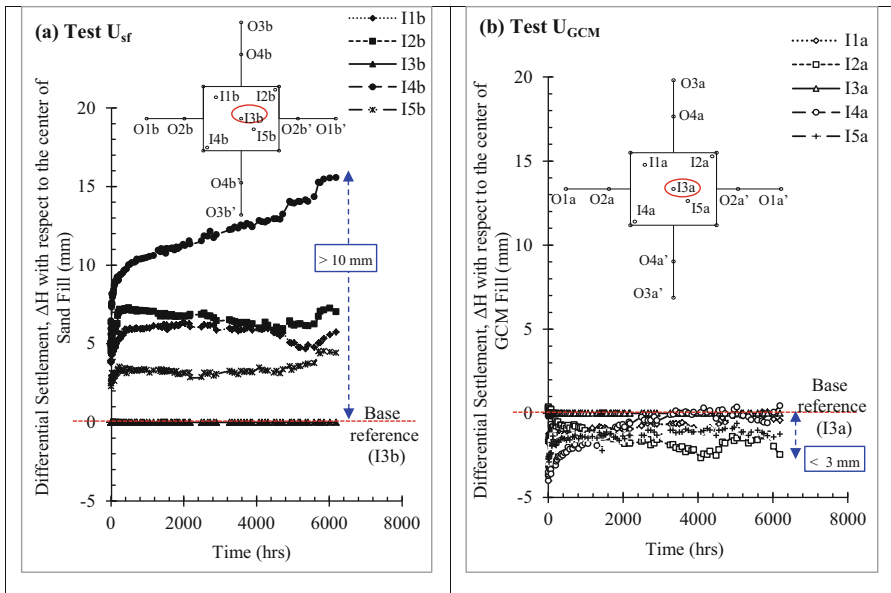
(b) Test  $E_{GCM}$  with GCM & Sand Fill

Fig. 10. Layout of embankment loading

Figure 11 shows the differential settlement with respect to the center point ( $\Delta H_x = \delta_x - \delta_{I3a/b}$ ), the point I3a and I3b being considered the base reference for both conditions. It compares the progressive differential settlement with time under both sand fill loading ( $U_{SF}$ ) and GCM fill loading ( $U_{GCM}$ ) gave maximum values of  $>10$  mm and  $<3$  mm for  $U_{SF}$  and  $U_{GCM}$ , respectively. Figure 10 also shows that with the  $U_{SF}$  test in particular there was a rapid initial settlement followed by secondary and tertiary consolidation effects. This phenomenon was not prominent in the  $U_{GCM}$  test.

Figures 8 and 12 gives details of the layout for the sand fill Uniform loading test  $U_{SF}$  and the absolute local differential settlement profile in the transverse and longitudinal directions. These profiles are nearly identical. The maximum absolute settlements recorded were 86 mm and 71 mm observed at the center ( $\Delta H_3$ ) and edge ( $\Delta H_2$ ). This gave  $\Delta H_3/\Delta H_2$  ratio to be 1.211. Furthermore, these observations portray a non-uniform settlement with a sagging profile under sand fill (flexible foundation behaviour). The constant settlement resulting at any time with  $U_{GCM}$  is further endorsed in Fig. 13 and in both transverse and longitudinal settlement profiles. The maximum settlements recorded were 56 mm and 55 mm at the center ( $\Delta H_3$ ) and edge ( $\Delta H_2$ ). The settlement ratio ( $\Delta H_3/\Delta H_2$ ) for  $U_{GCM}$  was 1.018 in this case. Hence, the observed differential settlement was both uniform and 70% less than that observed with the sand fill loading  $U_{SF}$ . This observation shows that the GCM fills have addressed the methodology can overcome the non-homogeneity on the peat ground (rigid foundation behaviour).

Another notable observation seen in both Figs. 12 and 13 is somewhat similar and circa 3 mm maximum heave of the ground outside the loaded base area. This is a consequence of the softness and the weak peat shear strength inducing a complete local shear slip surface beneath the loaded base.



**Fig. 11.** Comparison of differential settlement at strategic points on the base in  $U_{SF}$  and  $U_{GCM}$  tests

Figure 14 and 15 refers to the observations obtained with the embankment loading tests  $E_{sf}$  and  $E_{GCM}$ , respectively. The differential settlement with respect to the center of fill embankment ( $\Delta H_x = \delta_x - \delta_3$ ) in  $E_{sf}$  were significantly greater (>90%) than that from the  $E_{GCM}$  test as shown in Fig. 14(a). The results show settlement ranged from 5 to 125 mm. Non-uniform settlements experience under  $E_{sf}$  that increased with time and can be seen clearly through both transverse (see Fig. 14(b)) and longitudinal profiles (see Fig. 14(c)). The non-uniform thickness of peat deposit also contributes to the occurrence of bumpy roads, mainly when the road rests on the peat ground. Many researchers (e.g. Sas and Malinowska (2006); Oh et al. (2007a, b) and Ganasan (2016)) reported that a similar settlement pattern occurs when flexible foundation rests on the soft compressible soil.

However, results from  $E_{GCM}$  did not show any significant variation (<6 mm) as illustrated in Fig. 15(a). This is due to the stiff and contiguous mat structure and the consequent load sharing mechanism of the mosaic layer of the mats. The uniform settlement seen in the case of  $E_{GCM}$  is further endorsed in Figs. 15(b) and 15(c) through the transverse and longitudinal settlement profiles observed at any time, respectively.

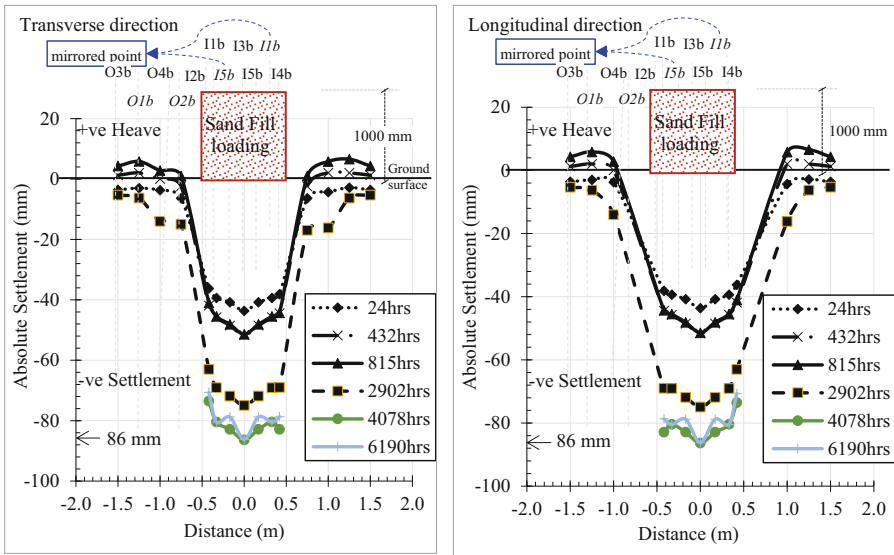
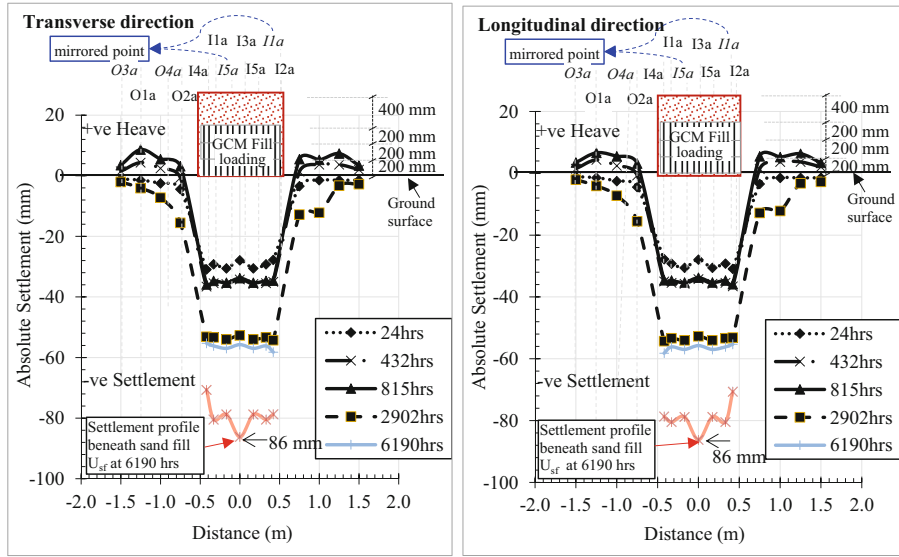


Fig. 12. Settlement profiles in transverse and longitudinal directions -test  $U_{sf}$

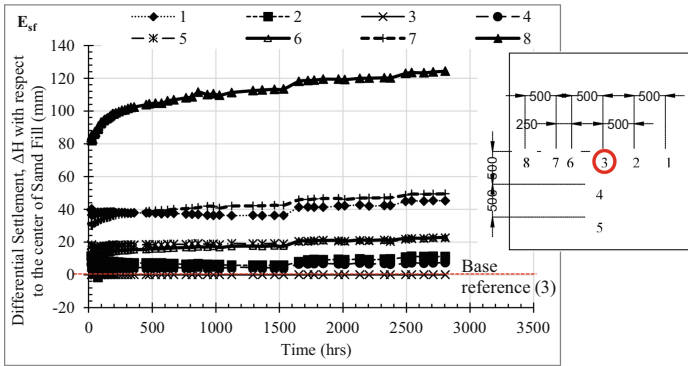


**Fig. 13.** Settlement profiles in transverse and longitudinal directions -test  $U_{GCM}$

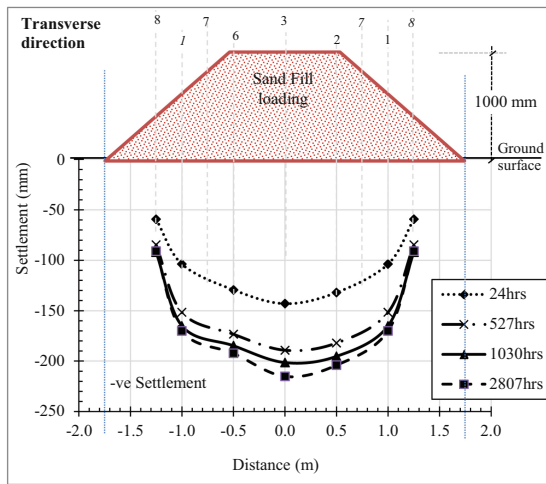
A long time after construction, the ground surface beneath sand fill embankment settled about 215 mm and 192 mm at the center and edge respectively (a ratio of 1.120) while similar observations with the GCM fills embankment were only 35 mm and 36 mm at the center and shoulder respectively (a 0.06 ratio). This can be further reduced with increasing the number of GCM fills ( $>3$  layers). The results showed that the use of GCM reduced the total settlements by about 84%. Higher settlements at the base lead to excessive deformation of pavement and stress enhancement. The presence of lightweight GCM fills (with a density range of 110 to 120  $\text{kg}/\text{m}^3$ ) to replace sand fill (with a density of 1400  $\text{kg}/\text{m}^3$ ) provided desired results, GCM being remarkably negating any differential settlement.

The observation under embankment fill loading shows that the total relative settlements in GCM fill embankment  $E_{GCM}$  was 84% less than that from the sand fill embankment ( $E_{sf}$ ). This is demonstrably seen in Fig. 16. Horizontal black lines in the figure represent the initial 0.2 m levels. Therefore, initial layer levels are datum lines and the red lines represent the observed settlement profiles of each layer traced by observing the movement of powdered tracer coal dust that was placed on the surface of each layer and near to the transparent wall to enable visibility.

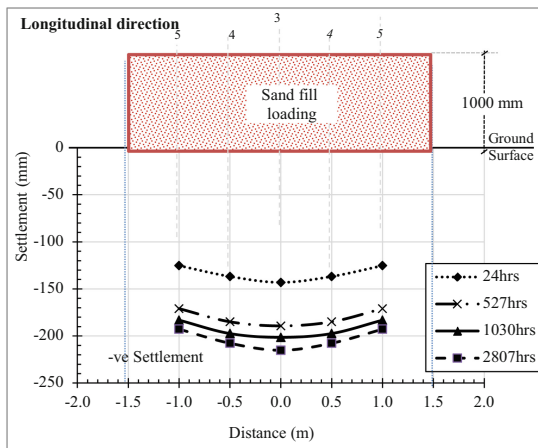
Based on the findings from the field study, it can be seen that the GCM fills not only reduces the excessive settlement but also the differential settlement. GCM also helped to accelerate the consolidation settlement within the sub-grade through the dissipation of any excess pore water pressure through the open-porous cellular structure of the GCM blocks.



(a)  $E_{sf}$  - Differential settlement plot

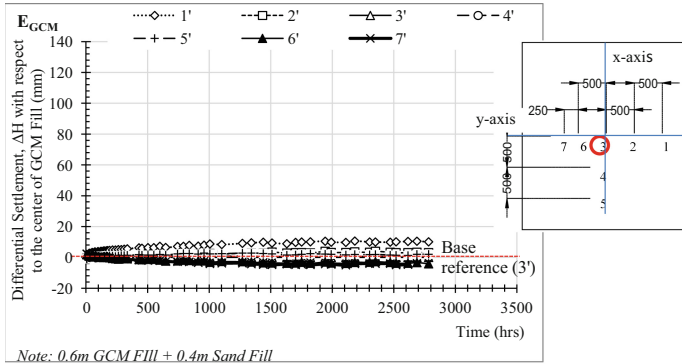


(b)  $E_{sf}$  - Transverse Settlement Profile

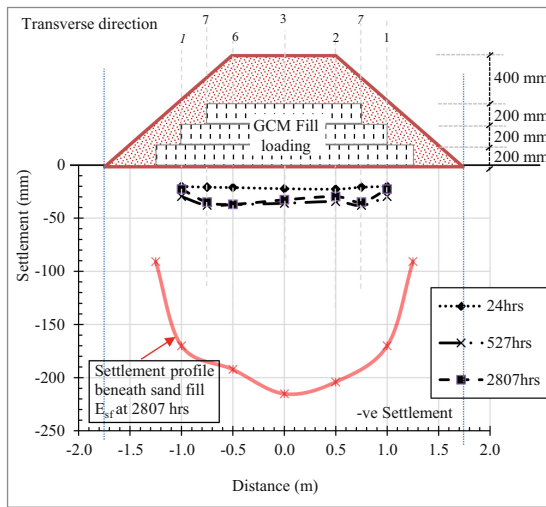


(c)  $E_{sf}$  - Longitudinal Settlement Profile

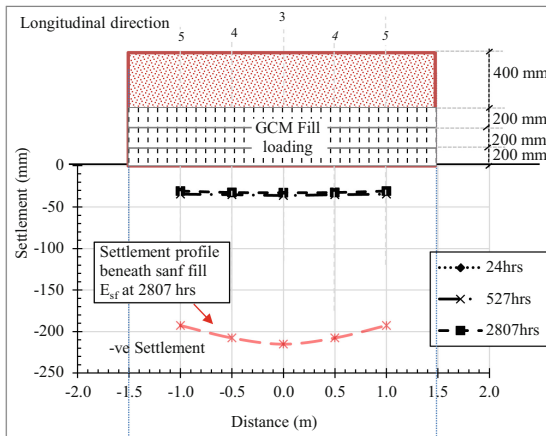
**Fig. 14.** Embankment loading test analysis– differential settlement and settlement profiles of test  $E_{sf}$  sand fill only (without GCM)



(a)  $E_{GCM}$  - Differential settlement plot



(b)  $E_{GCM}$  - Transverse Settlement Profile



(c)  $E_{GCM}$  - Longitudinal Settlement Profile

**Fig. 15.** Embankment loading test analysis– differential settlement and settlement profiles of test  $E_{GCM}$  (with GCM)



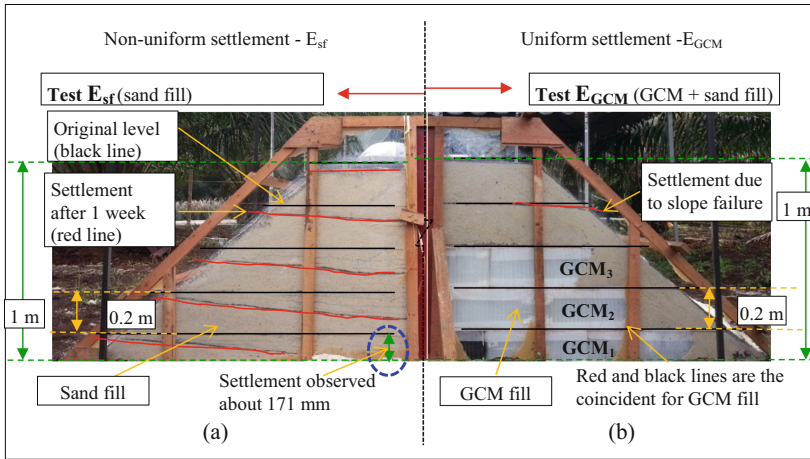


**Fig. 16.** Visual observation of settlement profile for field test group; (a) non-uniform settlements observed in flexible foundation test  $E_{sf}$ , and (b) uniform and minute settlements observed in rigid foundation  $E_{GCM}$

## 7 Conclusions

Engineers need to circumspectly consider “Peat” either as a “misnomer” of being called a “soil” or accept this unique soil as an “outlier” within the realms of traditional soil mechanics and provide stiff porous lightweight fills such as the Geocomposite Cellular Mat (GCM) to negate or minimize any untoward excessive non uniform settlements. The findings show that the soil settlement significantly improved with the GCM fills, which the maximum settlements and differential settlement were reduced by up to 84% and 70%, respectively.

**Acknowledgement.** The authors would like to express gratitude to Universiti Tun Hussein Onn Malaysia (UTHM) for the financial support to carry out this research and publish this paper.

## References

- ASTM D4427-92: Standard Classification of Peat Samples by Laboratory Testing. Annual Book of ASTM Standards, Philadelphia (1997)
- Andriessse, J.P.: Permanent constraints in Peat Reclamation. Nat. Manag. Trop. Peat Soils. FAQ Soil Bull. **59**, 81–91 (1988)
- Arellano, D.: Preliminary design procedure for EPS block geofom lightweight fill in levees overlying soft soils. In: 27th Annual Association of State Dam Safety Officials Conference. University of Memphis, Tennessee (2010)
- Balasubramaniam, A.S., Phien-Wej, B., Indraratna, B., Bergado, D.T.: Predicted behaviour of a test embankment on a Malaysian marine clay. In: Proceedings of International Symposium on Trial Embankments on Malaysian Marine Clays, Kuala Lumpur, vol. 2, pp. 1-1-1-7 (1990)
- Barden, L.: Primary and secondary consolidation of clay and peat. *Géotechnique* **18**(1), 1–24 (1968)

- Basri, K., Wahab, N., Talib, M.K.A., Zainorabidin, A.: Sub-surface profiling using electrical resistivity tomography (ERT) with complement from peat sampler. *Civ. Eng. Archit.* **7**(6A), 7–18 (2019). <https://doi.org/10.13189/cea.2019.071402>. <http://www.hrpub.org>
- Brand, E.W.: Predicted and observed performance of an embankment built to failure on soft clay. *Geotech. Eng.* **22**, 23–41 (1991)
- Huat, B.H.: *Organic and Peat Soils Engineering*. Universiti Putra Malaysia Press, Serdang (2004). ISBN: 983-2871-08-5
- Construction Research Institute of Malaysia: *Guidelines for Construction on Peat and Organic Soils in Malaysia*. Perpustakaan Negara Malaysia (2015). ISBN: 978-967-0242-15-6
- Ebid, A.M.: *Applications of genetic programming in geotechnical engineering*. Doctoral thesis, Ain Shams University, Cairo (2004)
- Edil, T.B.: Recent advances in geotechnical characterization and construction over peats and organic soils. In: Huat, et al. (eds.) *Proceedings of the 2nd International Conference on Advances in Soft Soil Engineering and Technology*, Putrajaya, Malaysia, pp. 85–108 (2003)
- Ganasan, R.: *Evaluation of innovation lightweight fill in problematic soil*. MSc thesis, Universiti Tun Hussein Onn Malaysia, Malaysia (2016)
- Hobbs, N. B.: Mire morphology and the properties and behaviour of some British and foreign peats. *Quarterly Journal of Eng. Geology and Hydrogeology*, London. **19**(1), 7–80 (1986).
- Huat, B.B.K., Maaail, S., Mohamed, T.A.: Effect of chemical admixtures on the engineering properties of tropical peat soils. *Am. J. Appl. Sci.* **2**(7), 1113–1120 (2005)
- Jarret, P.M.: *Geoguide 6: site investigation for organic soil and peat*. JKR Document 20709-0341-95 (1995)
- Indraratna, B., Rujikiatkamjorn, C., Wijeyakulasuriya, V., McIntosh, G., Kelly, R.: Soft soils improved by prefabricated vertical drains: performance and prediction (2010). <http://ro.uow.edu.au/cgi/viewcontent.cgi?article=1907&context=engpapers>
- Ismail, T.N.H.T., Wijeyesekera, D.C., Bakar, I., Wahab, S.: New lightweight construction material: cellular mat using recycled plastic. In: *Engineering Materials*, vol. 594, pp. 503–510 (2014a)
- Ismail, T.N.H.T., Hassanur, R., Ganasan, R., Wijeyesekera, D.C., Bakar, I., Sulaeman, A.: Physical and software modelling of performance of mat foundations on soft soil. In: *Proceedings of Soft Soils Conference* (2014b)
- Ismail, T.N.H.T.: *A critical performance study of innovative lightweight fill to mitigate settlement of embankment constructed on peat*. Doctoral thesis, Universiti Tun Hussein Onn Malaysia, Malaysia (2017)
- Ismail, T.N.H.T., Wijeyesekera, D.C., Lim, A.J.M.S., Yusoff, S.A.N.M.: Alternative construction technology over soft yielding ground using lightweight fill materials: an overview. *J. Eng. Appl. Sci.* **14**(16), 5602–5609 (2019)
- Jarret, P.M.: Recent development in design and construction on peat and organic soils. In: Huat, B.K., Bahia, H.M. (eds.) *Proceedings of Recent Advances in Soft Soil Engineering*, Sarawak, pp. 1–30 (1997)
- Johansson, F.: *Sättningar i sulfidjord – uppföljning och utvärdering av sättningarnas storlek och tidsförlopp, väg 760 i Norrbotten*. Luleå University of Technology, Department of Civil, Environmental and Natural Resources Engineering (2010)
- Kadir, M.I.A.: *Long term consolidation study on the tropical peat at Pekan, Pahang, Malaysia*. Doctoral thesis, Universiti Malaysia Pahang, Malaysia (2009)
- Kogure, K., Yamaguchi, H., Shogari, T.: Physical and pore properties of fibrous peat deposit. In: *Proceeding of the 11th Southeast Asian, Geotechnical Conference*, Singapore (2003)
- Kolay, P.K., Sii, H.Y., Taib, S.N.L.: Tropical peat soil stabilization using class F pond ash from coal fired power plant. *Int. J. Civ. Environ. Eng.* **3**(2), 79–83 (2011)
- Landva, A.O.: *Characterization of Escuminac peat and construction on peatland*. In: *Characterization and Engineering Properties of Natural Soils*, Singapore (2007)

- Leshchinsky, D., Marcozzi, G.F.: Bearing capacity of shallow foundations: rigid versus flexible models. *J. Geotech. Eng.* **116**(11), 1750–1756 (1990)
- Mutalib, A.A., Lim, J.S., Wang, M.H., Koonvai, L.: Characterization, distribution and utilization of peat in Malaysia. In: *Proceedings of International Symposium on Tropical Peatland*, pp. 7–16 (1991)
- Oh, E.Y.N., Balasubramaniam, A.S., Surarak, C., Chai, G.W.K., Bolton, M.W.: Interpreting field behaviors of embankment on estuarine clay. In: *The 17th International Offshore and Polar Engineering Conference*. International Society of Offshore and Polar Engineers, Lisbon (2007a)
- Oh, E.Y.N., Surarak, C., Balasubramaniam, A.S., Huang, M.: Observed behaviour of soft clay due to embankment loading: a case study in Queensland, Australia. In: *Proceedings of the 16th Southeast Asian Geotechnical Conference*, pp. 1–6 (2007b)
- Sas, W., Malinowska, E.: Surcharging as a method of road embankment construction on organic soil. In: *IAEG International Congress, United Kingdom*, Paper Number: 403 (2006)
- Von Post, L.: Swedish geological peat survey with the results obtained so far. *Sven. Mosskult. Tidskr.* **36**, 1–27 (1922)
- Wijeyesekera, D.C., Bakar, I., Ismail, T.N.H.T.: Sustainable construction material for challenging highway technology. *ARPN J. Eng. Appl. Sci.* (2015). ISSN: 1819-6608
- Wijeyesekera, D.C., Numbikannu, L., Ismail, T.N.H.T., Bakar, I.: Mitigating settlement of structures founded on peat. In: *IOP Conference Series: Materials Sciences & Engineering*, vol. 136 (2016)
- Wijeyesekera, D.C., Patel, J.C.: A three level finite difference analysis of the large strain one dimensional consolidation equation. *Geotech. J.* **2**(1), 1–13 (1998)
- Zainorabidin, A., Bakar, I.: Engineering properties of in-situ and modified hemic peat soil in Western Johor. In: *Proceedings of 2nd International Conference on Advances in Soft Soil Engineering and Technology*, Putrajaya, Malaysia, pp. 173–182 (2003)
- Zainorabidin, A., Wijeyesekera, D.C.: Geotechnical challenges with Malaysian peat. In: *Proceedings of the 2nd Annual Conference on School of Computing and Technology*. *Advances in Computing and Technology*, pp. 252–261 (2007)
- Zainorabidin, A., Wijeyesekera, D., Jayaratne, R.: Fabric of peat soils using image analysis. In: *Proceedings of the 5th Annual Conference on School of Computing and Technology*. *Advances in Computing and Technology*, pp. 38–44 (2010)
- Zainorabidin, A., Abdurahman, M.N., Kassim, A., Razali, S.N.M.: Settlement behaviour of Parit Nipah peat under static embankment. *Int. J. Geomate* **17**(60), 1–4 (2019)
- Zornberg, J.G., Christopher, B.R., Oosterbaan, M.D.: Tire bales in highway applications feasibility and properties evaluation. Colorado Department of Transportation Research Branch, Report no. CDOT-DTC-R-2005-2 (2005)
- Zwanenburg, C.: *The Influence of Anisotropy on the Consolidation Behaviour of Peat*. DUP Science (2005). ISBN: 90-407-2615-9



# Study on Response of Dual Layered Reinforced Stone Column Under Shear Loading

Akash Jaiswal<sup>(✉)</sup> and Rakesh Kumar

Department of Civil Engineering, Maulana Azad National Institute of Technology,  
Bhopal, India

**Abstract.** Stone columns are surely entitled for ground improvement and used on large scale by engineers these days. The vertical load capacity of stone columns reached to the ampler level by encasement of column material and using the bulging resistance due to confinement. Now, the efforts are in the direction for enhancement of shear strength of the stone column. The peripheral reinforcement is also considered for better shear strength by researchers. The objective of this paper is to study shear capacity of stone column on insertion of one extra layer of reinforcement in between peripheral layer and centre i.e. Dual Layered Reinforced Stone Column (DLRSC). In this experimental study, Geonets of small aperture openings are used as reinforcing layers due to their higher stiffness related to geotextiles. Various direct shear tests are conducted with different diameter and varying spacing between two layers of the reinforcement. Transformation in these combinations is also observed due to internal stresses generated by different values of Normal pressure. Outcomes are compared with the ordinary and single layered reinforced stone column which shows the significant amelioration to the shear strength of the stone columns.

**Keywords:** Stone column · Shear loading · Reinforcement · Geonet

## 1 Introduction

The soft soils have been ameliorated by changing the chemical properties or by changing the structural arrangement of particles which may cover two types of problems to the structures: one is the large settlement at lesser load and other is shear deformation/tilt of the structure. Fixing of such geotechnical issues for poor soils is Ground Improvement (Ghanti and Kashliwal 2008). Insertion of stone columns in the soft ground also deals with the Excessive settlement and bearing capacity problems of the soft/poor soil, hence came out as an effective tool for Soft Ground Improvement, which is in extensive application by Geotechnical Engineers now a days for many structures like Embankments, oil storage tanks and buildings on the soft clays (Gniel and Bouazza 2010; Shahu and Reddy 2014). The longitudinal load to the stone columns is transferred by the circumferential bulging of the column that provides increased stiffness to the ground (Bergado et al. 1994; Hughes et al. 1974).

It was observed that the bulging resistance or lateral confinement from the intervening soil may not be adequate for very loose soils. Required load bearing capacity at the limiting settlement will not be able to be developed by the stone column (Shahu et al. 2000). Afterwards for the more required capacity of stone column ameliorated grounds, the circumferential bulging resistance needed to be increased. Vertically loaded column with the encasement by use of various geosynthetics found much efficient in increasing the bearing stresses (Murugesan and Rajagopal 2006, 2007, 2010; Yoo and Kim 2009; Lo et al. 2010; Khabbazian et al. 2010; Pulko et al. 2011; Ali et al. 2012, 2014; Dash and Bora 2013). Further enhancement of bearing capacity and reduction in lateral bulging can be observed by the use of horizontal layers of Geosynthetics, that is due to the effect of interlocking and frictional effects of horizontal layers with stone column aggregates (Ayadat et al. 2008; Prasad and Satyanarayana 2015; Ghazavi 2018).

Lateral loading that caused Shear failure of the stone column was not in much recognition, the behavior under lateral loading for confined stone column was studied & shear strength increment was reported because of Encasing of granular material (Murugesan and Rajagopal 2009). Stiffness is the cause for the enhancement in shear strength for the smaller displacements, while on further increment in the displacements (larger displacements), the mobilization of tensile force is the cause for additive shear strength to encased stone column, which will be present /persist till the rupture of encasement (Mohapatra et al. 2016). Enhancement of shear strength for static as well as for cyclic lateral loading due the Encasement are also reported for stone column near the toe of Embankment (modeled with Unit cell shear device) (Cengiz et al. 2019). Study also shows that the grouped stone columns are more efficient for the shear strength resistance, because the confining-of intervening soil is also increased, but for the design considerations, further study is required for this aspect (Mohapatra et al. 2016).

Stone columns with vertical nails were also found effective which were inserted along the circumference of column body. Use of reinforcing nails driven around the circumference of the stone column up to a depth of 3D to 4D enhanced the performance of stone column; this is due to the increased confining of granular material (Babu and Shivashankar 2010). The installation of nails is more feasible than the geogrid that is the beneficial factor to use nails at the site (Komeil et al. 2015).

Current available study gives the insight about the shear failure of stone column, beneath the embankment. The stone columns which are on edge side of embankment are more vulnerable to failure. The literature study gives the idea of using Geonet, in place of geogrid or nailing at the circumference of the stone column. So in present study, geonets are used as reinforcing layers of stone column and behaviour of geonet reinforced stone column is discussed on application of shear loading.

## 2 Materials

### 2.1 Sand and Gravel

Soil bed was prepared by the sand collected from nearby sites in Bhopal city, which is poorly graded in nature, passing through the 4.75 mm sieve. The densities at the fully compacted and in loose state were found to be  $17.36 \text{ kN/m}^3$  and  $14.52 \text{ kN/m}^3$  respectively, also the density of sand at which tests were conducted was  $16.1 \text{ kN/m}^3$ .

Coarse grained soil, classified as GP, according to the soil classification system, was used as filling material for the stone column of 100 mm diameter. Other properties of sand and gravels are listed in the Table 1.

**Table 1.** Properties of sand and gravels used

Property	Sand	Gravel
Sp. gravity	2.64	2.68
D <sub>10</sub>	0.26	2.6
D <sub>30</sub>	0.38	3.1
D <sub>60</sub>	0.60	4.6
C <sub>u</sub>	2.30	1.77
C <sub>c</sub>	0.92	0.80
$\phi^\circ$	34°	42°

## 2.2 Geonets

Geonets were procured from the market. The properties of geonets used in this study are shown in Table 2, as provided by the manufacturer. The geonets used is of high density polyethylene, made with two crossover ribs. Geonets are used as reinforcement to the stone columns. For Single Layered Reinforced Stone columns (SLRSC) the layer of Geonet is placed at the Periphery of the Column, which encases the entire stone column.

**Table 2.** Characteristics of geonet

Characteristics	Value
Thickness	2 mm
Mass per unit area	740 gm/m <sup>2</sup>
Peak tensile strength	8 kN/m

For Dual Layered Reinforced Stone Column (DLRSC), Two layers of Geonet are used, the first one is same as placed in SLRSC (at the periphery), which is constant for all the DLRSC samples. Second layer of Geonet is placed inside the stone column body i.e. at 0.25d, 0.5d and 0.75d distance from the axis of stone column as shown in Fig. 1 which creates spacing of 0.75 d, 0.5d, 0.25d between two layers respectively.

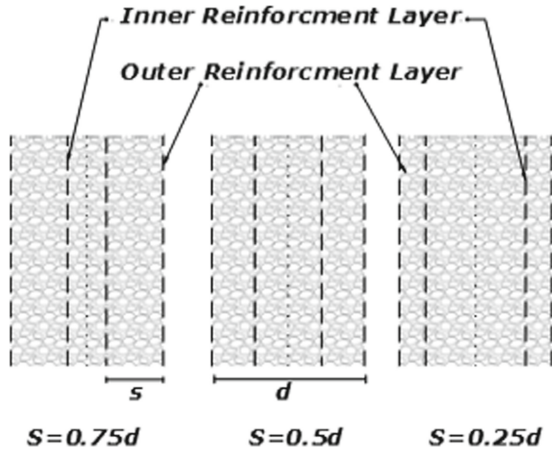


Fig. 1. Arrangement of reinforcement layers

### 3 Methodology

#### 3.1 Sample Preparation

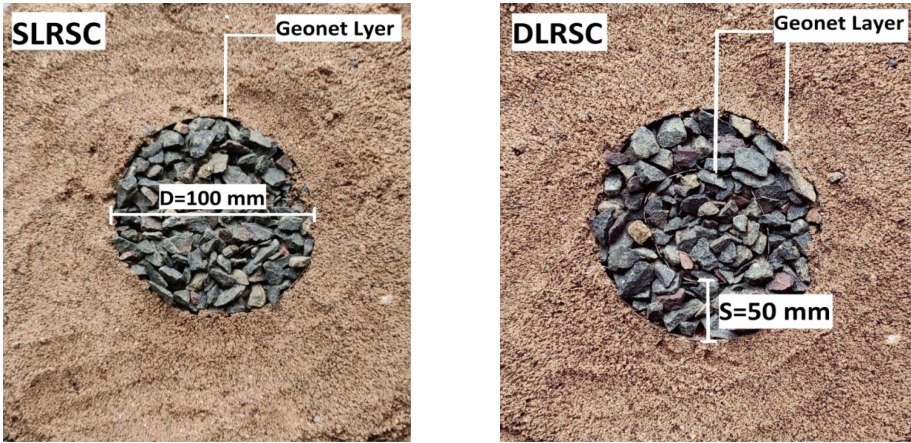
Poorly graded sand was used to make a soil bed in large shear box. Before preparing the sample with stone column, amount of sand was measured required to fill the shear box neglecting the portion equal to the volume of the stone column. So defined Pre-weighted sand was taken for each sample preparation and filled in Large Shear box, in 3 approximate equal layers. Each layer was provided a fixed amount of compaction by tamping, where the relative density for all the samples were in between  $68 \pm 2\%$ .

Three types of samples were prepared in the large shear box test, Unreinforced Stone Column (USC), SLRSC and DLRSC. For the USC, steel tube was placed inside the shear box and stones poured in steel tube in 5 approximate compacted layers with tamping each layer by fixed amount of compaction through fall of tamper from a height of 150 mm.

For SLRSC construction in the shear box, Geonets were placed on the inner surface of the steel tube and the stones were compacted in the similar fashion as performed for USC. After full length compaction steel tubes were pulled slowly leaving behind the Geonets in the peripheral place of the column, constructed column is shown in the Fig. 2(a).

Construction of DLRSC was done with Horizontal Layer of Geonet, which were folded to the shape of cylinder with the required diameter of 100 mm for outer layer of encasement. Similarly, for internal layer of encasement, the Geonet layer were folded to the shape of cylinder of lesser diameter 25, 50 & 75 mm respectively for spacing of 0.75d, 0.5d and 0.25d respectively. Both inner and outer layers of Geonet were held in vertical position and tied with thread at the bottom to the common horizontal Base made of Geonet only, the assembly made in such a manner that both the vertical layers of Geonet with the horizontal base can stand vertically without any lateral support. This is made by using small pins as a strut between two layers. Also the joint made at the bottom end of encasement helped to keep encasement in the position. This whole assembly of Geonet

layers and horizontal base was placed inside the Steel tube, which were already kept in the shear box apparatus for making stone columns. The assembly is placed such that the outer layer of encasement touches the inner periphery of the steel Tube. For DLRSC the material was also compacted in 5 layers but the compaction was done separately for both the areas i.e. the area between inner & outer layer of encasement and area encased by the inner layer of encasement. Amount of sand equal to the volume of encasement material inside the stone column was reduced for filling the DLRSC. The steel tube used was removed slowly after the compaction of material inside the stone column, one of the constructed stone column is shown in Fig. 2(b).



(a) Constructed Single Layered Stone Column

(b) Constructed Dual Layered Stone Column

**Fig. 2.** (a) Constructed single layered stone column (b) Constructed dual layered stone column

### 3.2 Test Setup

The large shear box apparatus was used for testing the shear strength of the prepared samples. The apparatus has an area of  $305 \times 305$  mm in the plan with the effective height available for soil specimen of 150 mm. The apparatus has the predefined horizontal plane of failure at the vertical center of the specimen. This horizontal plane is maintained by the two halves of the shear box apparatus. The lower half of the box moves on the roller in the horizontal direction whereas the upper one remains in the position. Due to this assembly, the soil mass inside the box also tends to separate along the predefined horizontal plane. The strain of lower box can be measured by the Strain Gauge already positioned. Loading yoke support the top half of the shear box and connected to the load transducer which reads the resistance of the soil to the horizontal loading. The loading is applied to the specimen through a motorized device, which allows providing constant rate of loading for the test. A loading cap was used to maintain the normal load over the soil specimen by manually changing the calibrated dead weights for different normal pressure.



### 3.3 Procedure

To study the effect of single and double layered encasement, Stone columns were installed in the sand bed. Tests were conducted for different normal pressures of 20, 40, 60 & 80 kPa. Required normal load was applied via available top cap of the shear box. After the application of normal pressure horizontal load was applied to the lower half of the shear box, with the constant displacement rate of 1.2mm/ min. Resistance to this displacement was measured at the end of each minute from the load transducer. Test was continued for 50 min and then terminated because resistance offered by the specimen was observed to decrease significantly.

## 4 Result and Discussion

Lateral load to the lower half of the shear box apparatus were applied till the resistance became constant against the horizontal displacement. The sand was removed which was used to construct the soil bed and the deformation of the stone column body was observed. Failure was observed in the similar fashion as Type-2 reported by Mohapatra et al. (2016) for the high rupture strain case of encasement. In all the dual encased stone columns, outer layer of encasement had high strain values than the inner layer of encasement. The cases in which the spacing was higher between the encasements, the differences in strains of both the encasement layers was large i.e. the horizontal movement of inner layer at the failure plane started on later stage of the test.

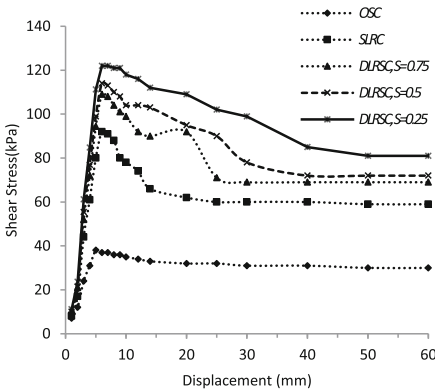


Fig. 3. Shear stress variation with horizontal displacement at normal pressure 80 kPa

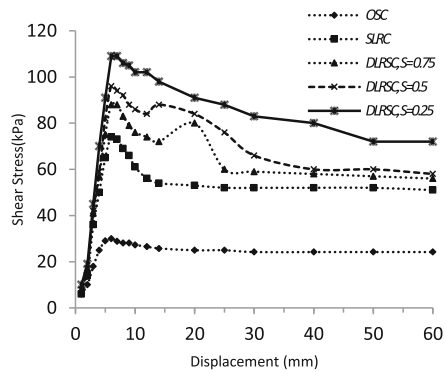


Fig. 4. Shear stress variation with horizontal displacement at normal pressure 60 kPa

### 4.1 Influence of Normal Pressure

Tests were performed at various normal pressure ranging from 20 kPa to 80 kPa, at each normal pressure condition on OSC use, SLRSC and DLRSC with 3 different spacing of encasement were tested. The observed values of shear resistance are shown with horizontal displacements in Fig. 3, 4, 5 and 6. SLRSC provides the confinement to the column material, due to which the shear resistance increases approximately 3 times.

Also, DLRSC is more effective than the SLRSC, more than 1.5 times of improvement observed for lower Normal stress of 20 kPa. This improvement over the SLRSC is due to additional confinement offered by the second layer of the encasement, which helps in restricting the movement of column material. As the normal stress increases towards higher side, improvement ratio reduces after 1.25 (Fig. 7). Hence, for the site where overburden pressure is less, DLRSC will be more efficient if the column beneath the earth is likely to bear the lateral load.

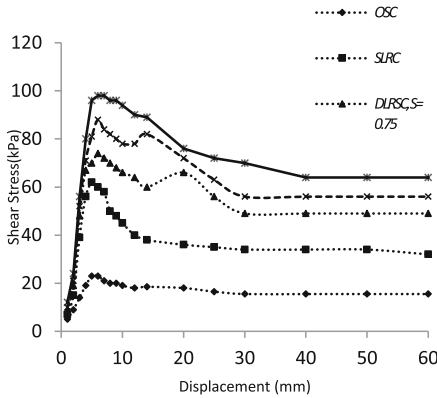


Fig. 5. Shear stress variation with horizontal displacement at normal pressure 40 kPa

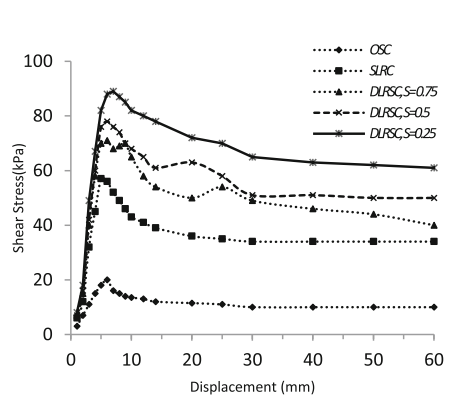


Fig. 6. Shear stress variation with horizontal displacement at normal pressure 20 kPa

Initial modulus of resistance observed was nearly same for SLRSC and DLRSC. In case of OSC, the initial tangent were tilted towards right which indicates the lesser value of initial modulus of resistance (Fig. 3, 4, 5 and 6) in all four normal pressure conditions. This shows the considerable enhancement in the stiffness of stone column due to the encasement of column.

**4.2 Encasement of Column**

The strain softening was observed for OSC and SLRSC at early displacements of 5–7 mm, just after the peak shear resistance, that continues till the end of the test. In case of DLRSC, for all 3 spacing conditions, some stain hardening was observed after the peak shear strength, but the resistance did not reach again after the peak resistance was offered by the stone column body. Slope of the graph of shear stress vs Horizontal Displacement after the highest point can be seen steep for case of SLRSC but in case of DLRSC it is mild, especially in the case with where spacing between encasements is 0.25d.

The gain of strength after the highest point of resistance is due to the inner layer of encasement. When the horizontal displacement occurs, gradually effect of it reaches up to the inner layer of encasement and this layer starts to act as an additive barrier which provides the strength to the column body even at higher stains. The resistance does not reach again up to the ultimate peak because when the inner layer provides the strength till that time the outer layer reaches to its creep level i.e. elongation without any increment of load.

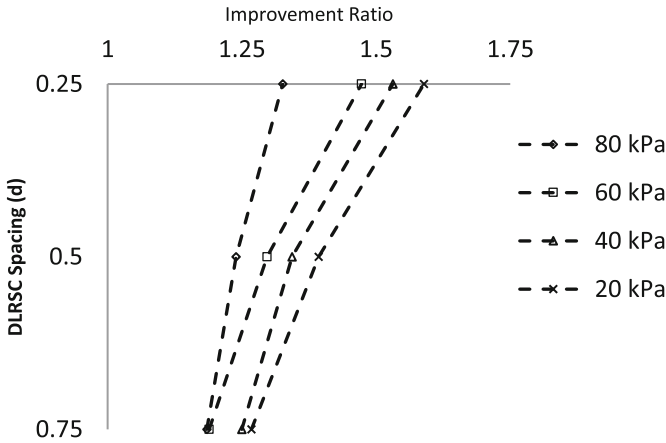
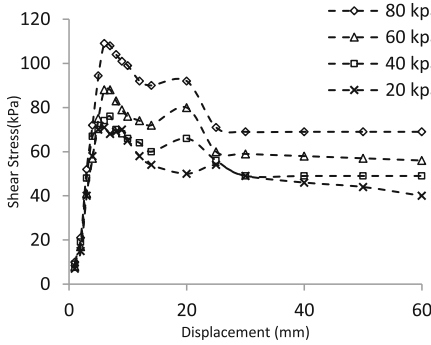


Fig. 7. Improvement ratio of DLRSC over SLRSC

### 4.3 Spacing of Encasement

In DLRSC, for encasement spacing of 0.75d, the additional strength mobilizes at the horizontal displacements of 20–25 mm, as the graph (Fig. 8) indicates the second local peak of shear strength. But for the 0.5d spacing of encasement this local peak of shear strength comes at earlier stage of horizontal displacement i.e. at 10–15 mm (Fig. 9). No such local peak is observed for case of 0.25d encasement spacing (Fig. 10). It indicates, as the spacing increases or inner layer of encasement is more towards the centre of stone column, contribution of this layer in resisting the lateral movement starts in the later stages of load application.

Lesser the spacing between the encasement, continuous strength is offered to the column, as shown in Fig. 10, where no local fluctuation (Only the reduction in shear stress, no any increment for any small region) is detected. But on the other hand in Fig. 8, 9 for higher spacing between the encasement, local fluctuation (Not the constant pattern of reduction of stresses in the region of 15 to 30 mm displacement, stresses increases and then decreases again), in strength can be seen again after the displacement of 15 mm. This local fluctuation occurs because of the higher spacing ( $S = 0.75$ ) between geonet. When shear applies to the stone column body, firstly the outer layer of encasement starts to resist it and gives the strength to the column body. The highest point of shear stress shows the full mobilization of strength of outer layer. After the failure of outer encasement, when the shear displacement reaches to the inner layer of the encasement, this layer starts resisting the shear displacement and takes part in providing strength to the column body. Due to the restrengthening of stone column the local fluctuation occurs as the stresses increases till the full mobilization of strength of inner layer of encasement. This fluctuations are relatively high in case of large spacing (Fig. 8) then the lesser spacing case (Fig. 9). For the lowest spacing ( $S = 0.25$ ) case in this study there is no fluctuation (Fig. 10) were observed. This happen because when the geonets are placed closely, after the failure of outer layer, the inner layer starts contributing to the strength immediately.



**Fig. 8.** Shear stress variation for DLRSC ( $S = 0.75d$ ) different normal pressure

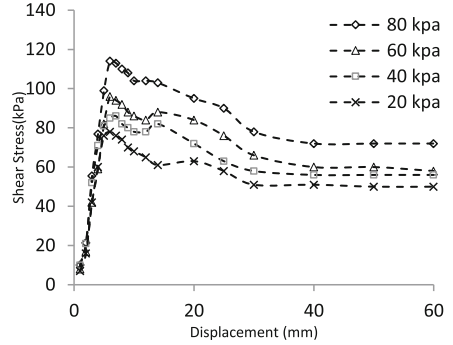


**Fig. 9.** Shear stress variation for DLRSC ( $S = 0.5d$ ) at different normal pressure

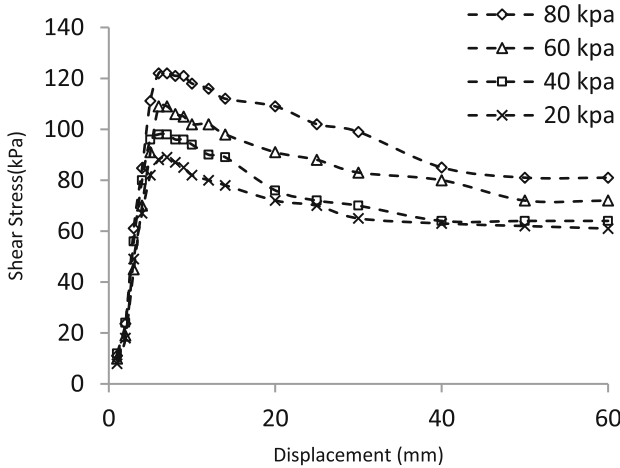


**Fig. 10.** Shear stress variation for DLRSC ( $S = 0.25d$ ) at different normal pressure

## 5 Conclusion

Direct shear stress tests were conducted for many type of Stone columns installed in the Laboratory shear box setup and obtained results were analyzed. Based on the observations some conclusions are listed below:-

- Lateral strength of stone column increases due to the encasement of column material and additional shear resistance is also provided by the encasement material.
- SLRSC performs three times better than the OSC in case of shear loading.
- The peak shear strength of the DLRSC enhances substantially over the SLRSC due to provision of additional confinement of the column material by inner layer of Geonet.

- In case of DLRSC, improvement in peak shear strength from SLRSC is more than 1.5 times for lower normal stress conditions of 20 or 40 kPa and for normal stress of 80 kPa the improvement is in between 1.25 to 1.5 times.
- Lower spacing (i.e. 0.25d) between the two layers of encasement is more effective than the higher spacing (i.e. 0.75d), in case of column subjected to lateral loading.

## References

- Ali, K., Shahu, J.T., Sharma, K.G.: Model tests on geosynthetic-reinforced stone columns: a comparative study. *Geosynth. Int.* **19**(4), 292–305 (2012)
- Ali, K., Shahu, J.T., Sharma, K.G.: Model tests on single and groups of stone columns with different geosynthetic reinforcement arrangement. *Geosynth. Int.* **21**(2), 103–118 (2014)
- Ayadat, T., Hanna, A.M., Hamitouche, A.: Soil improvement by internally reinforced stone column. *Ground Improv.* **161**(2), 55–63 (2008)
- Bergado, D.T., Chai, J.C., Alfaro, M.C., Balasubramaniam, A.S.: *Improvement Techniques of Soft Ground in Subsiding and Lowland Environment*. Balkema, Rotterdam (1994)
- Cengiz, C., Kilic, I.E., Guler, E.: On the shear failure mode of granular column embedded unit cells subjected to static and cyclic shear loads. *Geotext. Geomembr.* **47**, 193–202 (2019)
- Dash, S.K., Bora, M.C.: Influence of geosynthetic encasement on the performance of stone columns floating in soft clay. *Can. Geotech. J.* **50**(7), 754–765 (2013)
- Ghazavi, M., Yamchi, A.E., Afshar, J.N.: Bearing capacity of horizontally layered geosynthetic stone column. *Geotext. Geomembr.* **46**, 312–318 (2018)
- Gniel, J., Bouazza, A.: Construction of geogrid encased stone columns: a new proposal based on laboratory testing. *Geotext. Geomembr.* **28**(1), 108–118 (2010)
- Hughes, J.M.O., Withers, N.J.: Reinforcing of soft cohesive soils with stone columns. *Ground Eng.* **7**(3), 42–49 (1974)
- Khabbazian, M., Kaliakin, V.N., Meehan, C.L.: Numerical study of the effect of geosynthetic encasement on the behaviour of granular columns. *Geosynth. Int.* Thomas Telford **17**(3), 132–143 (2010)
- Lo, S.R., Zhang, R., Mak, J.: Geosynthetic-encased stone columns in soft clay: a numerical study. *Geotext. Geomembr.* **28**(3), 292–302 (2010)
- Mohapatra, S.R., Rajagopal, K., Sharma, J.: Direct shear tests on geosynthetic-encased granular columns. *Geotext. Geomembr.* **44**, 396–405 (2016)
- Murugesan, S., Rajagopal, K.: Geosynthetic encased stone columns: numerical evaluation. *J. Geotext. Geomembr.* **24**(6), 349–358 (2006)
- Murugesan, S., Rajagopal, K.: Model tests on geosynthetic encased stone columns. *Geosynth. Int. J.* **24**(6), 346–354 (2007)
- Murugesan, S., Rajagopal, K.: Shear load tests on stone columns with and without geosynthetic encasement. *Geotech. Test. J.* **32**(1), 76–85 (2009)
- Murugesan, S., Rajagopal, K.: Studies on the behavior of single and group of geosynthetic encased stone columns. *J. Geotech. Geoenviron. Eng.* **136**(1), 129–139 (2010)
- Pulko, B., Majes, B., Logar, J.: Geosynthetic-encased stone columns: analytical calculation model. *Geotext. Geomembr.* **29**(1), 29–39 (2011)
- Siva, S., Prasad, G., Harish, Y., Satyanarayana, P.V.V.: Stabilization of marine clays with geotextile reinforced stone columns using silica-manganese slag as a stone column material. *Inter. J. Comp. Eng. Res.* **9**, 2250–3005 (2015). ISSN
- Shivashankar, R., Dheerendra Babu, M.R., Nayak, S., Manjunath, R.: Stone columns with vertical circumferential nails: Laboratory model study. *Geotech. Geol. Eng.* **28**(4), 695–706 (2010). <https://doi.org/10.1007/s10706-010-9329-1>

- Shahu, J.T., Madhav, M.R., Hayashi, S.: Analysis of soft ground—Granular pile-granular mat system. *J. Comput. Geotech.* **27**(1), 45–62 (2000)
- Shahu, J.T., Reddy, Y.R.: Estimating long-term settlement of floating stone column groups. *Can. Geotech. J.* **51**(7), 770–781 (2014)
- Valipourian, K., Shirazi, M.R., Kafsh, O.Z.: The Effect of Stone Column (Nailing and Geogrid) on Stability of Expansive Clay (Version 10002274) (2015). <https://doi.org/10.5281/zenodo.1108486>
- Yoo, C., Kim, S.B.: Numerical modeling of geosynthetic-encased stone column-reinforced ground. *Geosynth. Int.* **16**(3), 116–126 (2009)

# Author Index

## A

Akhtarpour, Ali, [54](#)  
Akiyama, Nanoka, [14](#)  
Arce, Mario Terceros, [62](#)

## B

Bakar, Ismail, [84](#)

## C

Chen, Cheng, [75](#)

## G

Gong, Jun, [75](#)  
Guo, Yanrou, [23](#)

## H

Herrera, Mario A. Terceros, [62](#)

## I

Ieong, Jessica U. N., [23](#)  
Ismail, Tuan Noor Hasanah Tuan, [84](#)

## J

Jaiswal, Akash, [107](#)

## K

Kumar, Rakesh, [107](#)

## L

Li, Huihui, [31](#)  
Li, Lifeng, [31](#)

Liu, Jian-fei, [75](#)

Liu, Yong, [1](#)  
Lok, Thomas M. H., [23](#)

## M

Marinucci, Antonio, [62](#)  
Mohammadyar, Mohammad Amin, [54](#)

## N

Nishiyama, Satoshi, [14](#)

## P

Pan, Yu-Tao, [1](#)

## S

Sakita, Koki, [14](#)  
Song, Junsheng, [14](#)

## W

Wang, Man-Yu, [1](#)  
Wijeyesekera, Devapriya Chitral, [84](#)

## X

Xu, Liang, [31](#)

## Y

Yamazaki, Fumiaki, [14](#)  
Yao, Kai, [1](#)

## Z

Zhou, Zan, [23](#)